学位論文

Aspects of dark matter coannihilations

(暗黒物質の共対消滅について)

平成 28 年 12 月博士(理学)申請

東京大学大学院理学系研究科
物理学専攻
リュウ センペイ

Aspects of Dark Matter Coannihilations

Seng Pei Liew

A Dissertation
presented to the Faculty of the
University of Tokyo
in candidacy for the degree of
Phd

January 2017

Abstract

This thesis deals with particle physics of dark matter, particularly emphasizing the importance of particle physics phenomena in the early universe. Dark matter is one of the biggest mysteries in modern physics. Despite convincing evidence of its existence, its properties as a particle remain largely unknown.

Dark matter is a relic of the early universe if standard big bang cosmology applies. Understanding the behavior and interactions of dark matter in the early universe allows us to predict the present abundance of dark matter. Understanding how dark matter interacts also allows us to map constraints from dark matter detection experiments to the viable parameter space of the dark matter model in consideration.

In particular, this thesis deals with a specific type of dark matter production mechanism called coannihilation, where there exists, in addition to dark matter, a particle mediating the dark sector and the visible sector, and its mass is very close to that of the dark matter particle. We go through the calculations of coannihilation involving a particle carrying color (Quantum Chromodynamics, or QCD) charges, and emphasize the effects of the formation of colored bound state on the prediction of dark matter relic abundance on top of the better-known Sommerfeld effects. In addition, we study the case where the particle is also electrically charged.

Furthermore, we discuss other cosmological implications of colored bound states. If the colored particle's lifetime is long, it could affect the theoretical predictions of the big bang nucleosynthesis. It is known that the standard calculation (without including effects of exotic particles) of processes of big bang nucleosynthesis matches well with experimental observations, placing a stringent limit on the abundance of the long-lived particle. The formation of colored bound state in the early universe can change the prediction of the abundance of such a long-lived particle. If dark matter is super weakly interacting, the decay of the frozen-out colored particle can contribute to the relic abundance of dark matter as well. Finally, we study how the Large Hadron Collider (LHC) can probe scenarios of coannihilation and long-lived colored particles.

Summarizing our results, we find that for most cases, on top of the Sommerfeld enhancement, bound-state effects can further significantly increase the largest possible DM masses which can give the observed DM relic abundance, by $\sim 30 - 100\%$ with

respect to values obtained by considering the Sommerfeld effect only while considering DM coannihilating with color triplet or octet exotic particles. In particular, it indicates that the Bino DM mass in the right-handed stop-Bino coannihilation scenario in the Minimal Supersymmetric extension of the Standard Model (MSSM) can reach ~ 2.5 TeV. Such cosmological upper limits on the DM mass have far-reaching consequences; given that collider experiments constrain the mass of exotic massive colored particles from below, a more precise calculation of the relic abundance of DM tells us whether the LHC or a prospective high-energy collider can cover all parameter regions of the coannihilation scenarios. We find that a prospective 100 TeV could not test the right-handed stop-Bino coannihilation scenario fully, in contrast to previous estimates.

Acknowledgements

I would like to thank my supervisor, Koichi Hamaguchi, for introducing to me various topics in particle physics. He has provided not only professional advice and valuable mentoring, but also personal support and heartwarming encouragement.

I am grateful to Takeo Moroi, Motoi Endo, and Kazunori Nakayama for teaching me a lot, and providing insights into my studies. I have also been privileged to learn and collaborate with many other physicists, especially Philipp Grothaus, Feng Luo, Alberto Mariotti, Kentarou Mawatari, Kyohei Mukaida, Michele Papucci, Kazuki Sakurai, Satoshi Shirai, Matthias Vereecken, Alessandro Vichi, Yasuhiro Yamamoto, and Kathryn Zurek.

I would like to thank my friends and family for all the supports. This thesis is, in particular, dedicated to my parents, brother and sister. My friends, whether in Japan or other places around the world, have brought to me much fun and motivation during my study. I would like to thank my Japanese friends and colleagues, for being patient with my broken Japanese, and providing various helps throughout my study.

Finally, I would like to thank the Ministry of Education, Culture, Sports, Science and Technology (MEXT) of Japan, for providing me a golden opportunity to conduct research in the University of Tokyo. I also appreciate the financial support provided by the Leading Graduate Course for Frontiers of Mathematical Sciences and Physics (FMSP) program as well as the Japan Society for the Promotion of Science (JSPS), without which, I would not have learned so much from brilliant physicists around the world through international conferences and workshops.

Contents

List of Figures

List of Tables

Chapter 0

Preface

The discovery of the final missing piece of the Standard Model (SM), the Higgs boson, at the Large Hadron Collider (LHC) in 2012 is arguably one of the most important milestones in the history of mankind [1, 2]. This however, does not mean that we are done with particle physics. In fact, the Higgs itself brings up troubles and questions from the physicist's point of view. How the Higgs mass is tuned at the electroweak scale even though the radiative correction to its mass is quadratically divergent is one of the biggest questions (hierarchy or naturalness problem). Even neglecting the Higgs, there are mysteries involving the existence of dark energy and dark matter (DM). Particularly, the latter, of which the nature remains largely unknown, has attracted attention of physicists resolving its issues from the perspective of particle physics.

For these and many other reasons, the particle physics community has been bustling with rigorous activities, both in theory and experiment. Experimental physics has been advancing our understanding at a remarkable pace. The LHC has not only discovered a Higgs boson, but also ruled out many SM extensions. Experiments aiming to detect the scattering of particle DM with nuclei have achieved fruitful results, and many more similar experiments are going to operate soon. There is also a number of experimental programs that look for signals from the sky via space telescopes and Earth-based detectors. These experiments have also helped us understand particle physics as well as cosmic rays and astrophysics.

From the theoretical point of view, it has been expected that along with the Higgs, there must be new particles near the weak scale that could resolve the large hierarchy between the weak scale and the Planck scale induced by the relatively light Higgs. However, the LHC which probes the weak scale at the highest energy, has so far failed to find such particles. This has caused many people to abandon naturalness as a guiding principle of new physics. Without naturalness, new physics can appear at any scale, and since the LHC's capability to probe new physics is at best the TeV scale, it seems to be hopeless to find anything new at the energy frontier.

Dark matter may be another guiding principle about where the new physics (or new particle mass) scale lies at. The cosmological cold dark matter density depends on its annihilation and coannihilation rate, as well as its mass. In this thesis, we focus on the dark matter coannihilating with a certain colored particle. In such a scenario, it is possible to impose a cosmological upper bound on the dark matter mass (as well as the mass of the accompanying coannihilator) by requiring the dark matter density to be consistent with the observed one.

Particularly, we emphasize the effects of QCD bound states on the dark matter relic abundance. As will be shown in the following, dark matter relic abundance can be reduced by the bound-state effects. In many cases, the relic abundance of dark matter is significantly reduced as compared to previously obtained results. With these new calculations, one can impose a cosmological upper bound on the dark matter mass more confidently and project how experimental searches (particularly searches at the LHC) probe the viable parameter region of this type of models. While the scope of this study is beyond the study of coannihilation in supersymmetry (SUSY), it is worthwhile to emphasize one important implication of our calculations: that the stop/bino coannihilation scenario can no longer be discovered with a standard monojet search, even at a prospective 100 TeV collider.

This thesis is organized as follows. In Chapter 1, we illustrate the history and observational evidence that establish DM as a new particle that cannot be explained within the SM framework. We also set up basic cosmological notations used throughout the thesis.

Chapter 2 is dedicated to contemporary experimental methods that look for hints of non-gravitational interactions of DM. We will review the direct detection, indirect detection and collider search strategy used to look for possible particle physics signature of dark matter.

Chapter 3 discusses how to calculate the relic density of dark matter. The main ingredient is the Boltzmann equation governing the number density of dark matter throughout the cosmological history. We also describe how the coannihilation process, the main topic of this thesis, affects the number density of dark matter.

In Chapter 4, we deal exclusively with the early universe reactions of colored particles, which act as the coannihilator of dark matter. We give an account of the particles' annihilation cross section and the effects of Sommerfeld.

In Chapter 5, we provide an account of the formation of QCD bound state in the early universe and its consequences on the relic density of dark matter. We discuss the formation and dissociation rates of bound states, as well as the bound-state effects on the Boltzmann equations.

Chapter 6 deals with the numerical results of the dark matter relic density for the cases of interest. We also study the implications of our results on the Big Bang Nucleosyn-

thesis constraint on long-lived particles, and the collider constraints on colored particles. We also discuss how our newly calculated results change previously made conclusions on the coannihlation scenarios. Finally, we conclude.

Materials presented in Chapter 4, 5 and 6 are based on [3].

Chapter 1

Introduction

We first give a brief historical account of the discovery of dark matter (DM). We then provide a more detailed description of modern experiments and observations that establish convincingly the existing evidence of DM as the solution of the "missing matter" problem.

1.1 History of dark matter

The matter density in the local galactic neighborhood can be used to infer the dynamics of stellar objects. The use of stellar objects' velocity to determine the possible existence of DM was first suggested by Kapetyn and then later emphasized by Oort [4, 5].

Beyond local galactic neighborhood, one can, utilizing the mass-to-light ratio of galactic clusters, deduce how fast galaxies move in the clusters under the gravitational influence of luminous matter. In 1930s, Zwicky found a mass discrepancy as he measured the galaxies' redshifts in the Coma cluster [6]. According to his observation, the galaxies were moving so fast relative to the cluster mean velocity that, the required cluster mass would have to be 400 times larger than the observed luminous matter mass. Zwicky proposed the existence of DM within the cluster in order to resolve the discrepancy. Three years later, Smith found that the Virgo cluster behaves similarly, i.e. the mass-to-light ratio is unexpectedly high [7].

Since then, there were a few more observations of anomalous dynamics of various galactic objects but the DM interpretation was not given much attention. Around 25 years later, Kahn and Woltjer observed that the M31 and the Milky Way galaxy were moving towards each other [8]. As both of them were not likely to have been formed very far from each other, they must have performed at least one orbit around their center of gravity. Kahn and Woltjer deduced from the mass of the Local Group from this observation and found that the required mass is at least six times larger than the observed one, i.e. there is some invisible form of matter.

It was not until 1970s that observations of anomalous behaviors of the rotation curve of galaxies provided clear evidence of the existence of DM. The first work can be traced to 1939; Babcock showed that the rotation curve of M31 had unexpectedly high velocity [9]. In 1970s, the work of Rubin and Ford, and subsequent observations using 21-cm line by Roberts and Whitehurst strongly suggested the presence of DM in various galaxies [10, 11]. These results were further corroborated by the works of Ostriker and Peebles on the stability of galactic disks, and independent works of Einasto & Saar and Ostriker et. al. on companion galaxies [12–14]. The majority of astronomers were convinced by the concept of DM at that time.

The next big question was whether DM is hot (relativistic) or cold (non-relativistic). Initially the focus was on hot DM, where neutrino was considered the natural candidate of DM as no ingredients beyond the Standard Model (SM) are required[15]. Neutrino also satisfies the condition of DM being weakly interacting. The relation of hot DM with cosmic structure formation was studied by the Zel'dovich group and the hot DM interpretation was later ruled out by simulation of the nonlinear growth of structure of the universe [16].

Gravitino, the supersymmetric (SUSY) partner of graviton with mass $\lesssim$ 1keV was studied as the candidate of DM in 1982 [17]. Warm and cold DM were studied in the same year as well [18]. Subsequent studies focused on the cosmic structure of the universe due to DM, and during the same period of time, neutralino (SUSY partner of neutral gauge boson) was suggested as the candidate of DM. [19] By then, there was a consensus that part of our universe consists of (cold) DM within the scientific community. Along with the discovery of dark energy, the so-called ΛCDM cosmology (where the energy density of the universe is assumed to be consisting of baryons, non-baryonic DM and dark energy) has become the "standard model" of cosmology.

1.2 Cosmology

Before making more quantitative description and exploration, let us first set up the notations of cosmology used in this dissertation. For a more complete account of relevant topics, see e.g. [20] and [21]. From observations such as the X-ray background radiation and galaxy surveys, it is safe to assume that our universe is isotropic (the universe looks the same (at large scale) in all direction) and homogeneous (observers see the same conditions at any point in the universe). Mathematically, this leads to the Friedmann-Robertson-Walker metric, of which the line element reads

$$g_{\mu\nu}dx^\mu dx^\nu = ds^2 = dt^2 - a^2(t)\left[\frac{dr^2}{1-kr^2} + r^2\left(d\theta^2 + \sin^2\theta\, d\phi^2\right)\right], \tag{1.1}$$

where $a(t)$ is the scale factor. r, θ and ϕ are the comoving spatial coordinates. k determines the spatial curvature of the universe, i.e. $k = -1$ corresponds to an open, $k = 0$

to a flat and $k = +1$ to a closed universe.

Meanwhile, the Einstein's equations are:

$$R_{\mu\nu} - \frac{1}{2}\, g_{\mu\nu} R = 8\pi\, G T_{\mu\nu}. \tag{1.2}$$

$R_{\mu\nu}$ and R are the Ricci tensor and Ricci scalar, respectively. G is the gravitational constant and $T_{\mu\nu}$ is the energy-momentum tensor. At large scale, vector and tensor fields of matter average to zero, and thus they should be isotropic and homogenous. Then, the energy-momentum tensor should take the following form:

$$T^{\mu}_{\ \nu} = \begin{pmatrix} +\rho & 0 & 0 & 0 \\ 0 & -p & 0 & 0 \\ 0 & 0 & -p & 0 \\ 0 & 0 & 0 & -p \end{pmatrix}. \tag{1.3}$$

The energy conservation law $T^{0\mu}{}_{;\mu} = 0$ is satisfied in the Friedmann-Robertson-Walker metric, giving

$$\dot{\rho} + 3\, H\, (\rho + p) = 0, \tag{1.4}$$

where $H \equiv \dot{a}/a$ is the Hubble parameter, which is an important parameter describing the expansion rate of the universe. Solving the Einstein's equations gives the Friedmann equation:

$$H^2 = \frac{8\pi\, G}{3}\rho - \frac{k}{a^2}. \tag{1.5}$$

If the equation state of matter is proportional to ρ, i.e.

$$p = w\rho, \tag{1.6}$$

we can solve Eq. (1.4), giving

$$\rho \propto a^{-3-3w}. \tag{1.7}$$

The most interesting cases with physical meaning are as below:

$$\text{cold matter (non-relativistic)} : \rho_M \propto a^{-3} \tag{1.8}$$

$$\text{hot matter (relativistic)} : \rho_R \propto a^{-4} \tag{1.9}$$

$$\text{vacuum energy} : \rho_\Lambda = -p_\Lambda = \text{constant} \tag{1.10}$$

If our universe is flat, i.e. $k = 0$, the scale factor $a(t)$, after solving the Friedmann equation has simple form:

$$\text{cold matter dominated} : a(t) \propto t^{2/3} \tag{1.11}$$

$$\text{hot matter dominated} : a(t) \propto \sqrt{t} \tag{1.12}$$

$$\text{vacuum energy dominated} : a(t) \propto \exp(Ht) \tag{1.13}$$

From the results of the Supernova Cosmology Project and the High-z Supernova Search Team [22, 23], we know that the current universe is dominated by vacuum energy and the expansion of our universe is accelerating, i.e. our universe is well described by Eq. (1.13).

It is convenient to rewrite the ρ's (ρ_i) as follows:

$$\Omega_i(t) = \frac{\rho_i(t)}{\rho_c(t)}, \tag{1.14}$$

where

$$\rho_c(t) = \frac{3H_0^2}{8\pi G} \simeq 1.05 \times 10^{-5}\ h^2\ \text{GeV cm}^{-3}. \tag{1.15}$$

$\rho_c(t)$ is called the critical density. H_0 is the present value of the Hubble parameter. h is a value parametrized as follows:

$$H_0 = 100\ h\ \text{km s}^{-1}\ \text{Mpc}^{-1}, \tag{1.16}$$

where measurements show that $h \simeq 0.7$.

With all three types of matter/energy (relativistic and non-relativistic matter, vacuum energy) and arbitrary curvature k, we have, from the Friedmann equation,

$$1 = \Omega_R(z) + \Omega_M(z) + \Omega_\Lambda(z) - \frac{k}{a^2H^2}, \tag{1.17}$$

or, at present,

$$1 = \Omega_R + \Omega_M + \Omega_\Lambda + \Omega_k, \tag{1.18}$$

where $\Omega_k = -\frac{k}{a^2H_0^2}$.

1.3 Evidence

The amount of DM in a certain astronomical object cannot be measured directly. Typically, one measures the total amount of visible and invisible matter, and deduct the amount of visible matter which is measured by other means. Out of a plethora of astronomical and cosmological observations relating to DM, let us describe in more detail several modern pieces of convincing evidence establishing particle DM as the explanation of the observed "missing matter" in the universe, with a special emphasis on cosmic microwave background (CMB). Let us first notice that there were a few alternate theories to explain the "missing matter" problem. For example, Newtonian dynamics could modified at large scale (MoND), or there might be massive compact halo object (MACHO). We will show that such explanations are disfavored by observations in the following.

We first give a more quantitative description of the rotation curves of galaxies. Using classical Newtonian laws, one can show that, if $M(r)$ is the total mass inside a sphere of radius r from the galactic center, the velocity $v(r)$ of a test particle as a function of r is

$$v(r) = \sqrt{\frac{GM(r)}{r}}. \tag{1.19}$$

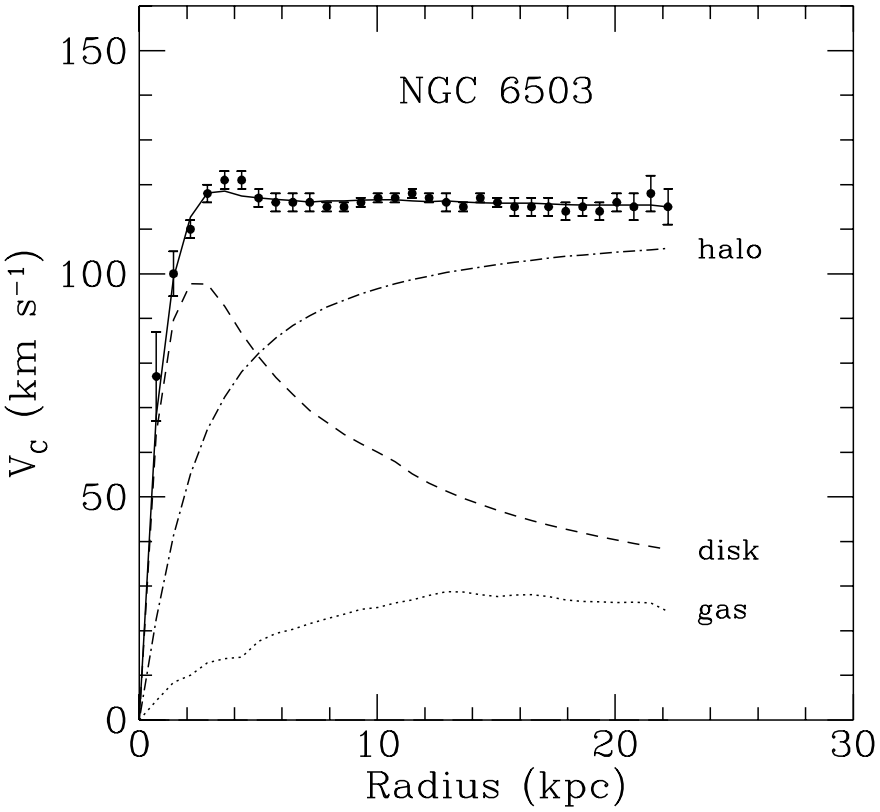

Figure 1.1: Typical velocity distribution of objects compared to the distance from the galactic center. The dashed-dotted line labelled "halo" is the expected mass contribution to the velocity distribution from DM, whereas the dashed and dotted lines show the contribution from disk and gas. Figure taken from [24, 25].

Outside the observable disk, the velocity of objects is expected to fall as $\sqrt{1/r}$. However, as described previously, objects' velocity remains constant at large r away from the luminous disk (see Fig. 1.1). This phenomenon can be explained by the existence of massive and invisible DM with halo density profile proportional to $1/r^2$.

Indeed, theories of MoND could in principle explain the anomalous rotation curves at large scale. Let us invoke another remarkable evidence that can rule out MoND: colliding clusters (or the so-called bullet cluster named 1E 0657-558) as observed in 2006 using the Hubble Telescope [26]. The fluid-like, X-ray emitting component forming the baryonic majority of the cluster galaxies, is observed to form a clear shock profile. See Fig . However, when mapping out the weak gravitational lensing of the system, the mass distribution does not trace the distribution of hot plasma. Instead, it behaves as if there

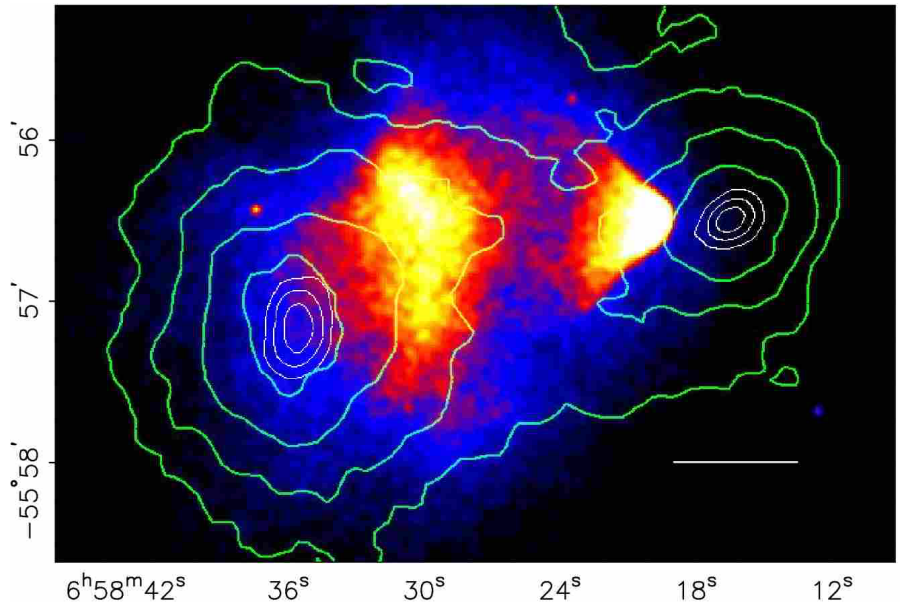

Figure 1.2: Shock profile of the bullet cluster [26]. The green contours show the gravitational potential mapped from weak lensing, while the colored region represents X-rays emission from the baryonic plasma. It can be seen that the mass distribution does not trace the distribution of hot plasma.

are invisible objects that pass through each other without collision. This indicates the particle-like behavior of DM and disfavors the MoND explanation.

1.3.1 Cosmic microwave background

Precision cosmology, in particular the measurement of the anisotropy of CMB gives quantitavely the most concrete proof of DM. While the full treatment of CMB is out of reach, here, we highlight features of the CMB anisotropy relevant to the energy density of DM.[1]

The big bang theory tells us that the universe was hot and dense in the very beginning of time. Photons were in thermal equilibrium with matter. When the universe started to expand and cool to $\sim$ 3000 K, atom hydrogen started to form and matter decoupled with photon (recombination). The free photon is a relic of light from the epoch of the last scattering, showing itself as CMB propagating in the present universe at $\sim$ 3K. While the almost isotropic CMB contains little information about the details of the cosmological model, the CMB anistropies carry the imprint of fluctuations in the early universe, which is fundamental to structure formation, and relevant to the matter content

[1] See, e.g. [27] for a more detailed account of this topic.

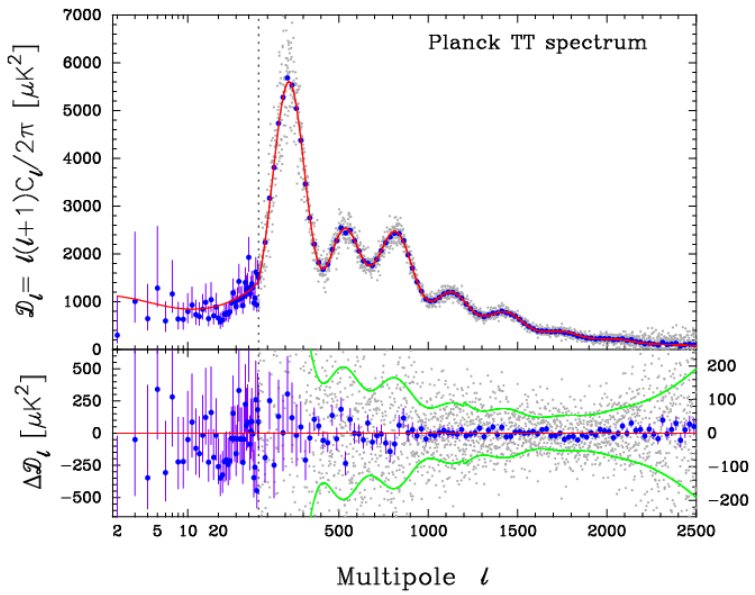

Figure 1.3: Temperature power spectrum presented by the Planck Collaboration [28]. The red line shows the best fit of the temperature spectrum using the ΛCDM cosmological model. The lower panel shows the residuals of the power spectrum with respect to the ΛCDM model.

and other important parameters of the universe.

It is the measurement of two point temperature correlation function that provides us the statistical information of CMB anistropies. Equivalently, it is the measurement of the power spectrum of Legendre moments C_l, which is the decomposition of the two point temperature correlation function into normal modes. Fig. 1.3 shows the result presented by the Planck Collaboration [28].

Before the last scattering, photon and baryons are tightly coupled to each other via (photon-electron) Thomson scattering and (electron-proton) Coulomb interaction such that, they form a fluid. Gravitational infall tends to compress the fluid, while the photon pressure resists the compression, leading to acoustic oscillations. These oscillations froze at recombination, and their imprints on the recombination surface becomes the acoustic peaks in the temperature anisotropy observed as in Fig. 1.3.

The acoustic peaks have physical meanings. Odd (even) peaks represent the compression (rarefaction) phase of the fluid. The angular scale (position) of the first peak reflects the distance the photon from the last scattering traveled, and thus determines the spatial

curvature of our universe. Recent results show that at 95% confidence level [29]:

$$\Omega_k = 0.0008 \pm 0.004. \tag{1.20}$$

The second peak can be used to deduce the baryon density $\Omega_b h^2$. Baryons increase the mass or inertia of the photon-baryon fluid, leading to an enhanced compression with respect to rarefaction of the fluid. Thus, by comparing the ratio of the amplitudes of the first and second peak, one can measure the baryon-to-photon ratio. The Planck measurement gives the baryon abundance $\Omega_b h^2$ [29]:

$$\Omega_b h^2 = 0.02230 \pm 0.00014. \tag{1.21}$$

Note that the uncertainties quoted here and hereafter indicate the 68% confidence level unless stated otherwise. It is worth to note that the baryon-to-photon ratio can as well be determined independently from the Big Bang Nucleosynthesis (BBN) processes [2]. Both measurements are consistent with each other.

The third peak indicates how much DM there is. While baryons couple strongly with photon before recombination, DM does not, and its compression is not affected by the counteracting photon pressure. This affects the overall amplitude of the acoustic peaks. The matter-to-photon ratio, and therefore the DM density $\Omega_{\rm DM} h^2$ can then be determined by relating the third peak with the first two, and recent results give:

$$\Omega_{\rm DM} h^2 = 0.1188 \pm 0.0010. \tag{1.22}$$

Roughly speaking, it tells us that DM makes up of around 26.8% of the energy density of the universe.

It is worth mentioning another large scale observation carrying rich cosmological information: baryon acoustic oscillations (BAO). The large scale structure of the universe originates from the density anistropies, which can be traced back and related to the CMB anistropies at recombination. The large survey on the distribution of galaxies, for example the Sloan Digital Sky Survey (SDSS), gives a power spectrum of BAO showing patterns matching those from CMB (see e.g. [31]).

1.3.2 Other issues

CMB anistropies, as well as BBN tell us clearly that most DM is non-baryonic. MACHO, which are baryonic, such as faint stars, white dwarfs, etc., are against the CMB and BBN observations. Indeed, other independent results show that MACHO has very little contribution to $\Omega_{\rm DM} h^2$ [32].

There is another issue about DM. Numerical simulations of DM halos with cold DM are in tension with observations. N-body simulations also predict too great number of

[2] For a review of BBN, see e.g. [30].

low mass halos. It is still unclear how serious this problem is, as it remains unknown whether the comparison of simulation with observation is appropriate [33].

Chapter 2

Detecting dark matter

Arguments in the previous Chapter establish the existence of dark matter at the astronomical/cosmological scale. As little is known about the particle aspects of dark matter, various strategies have been devised to uncover the microscopic properties of dark matter. The purpose of this Chapter is to give a overview of these strategies.

Let us first see how the macroscopic nature of dark matter gives us some hints of the particle properties of dark matter:

- **Dark matter interacts weakly.** The non-colliding behavior of bullet cluster implies that the DM-DM scattering cross section is weak ($\sigma \lesssim /m_{DM} < 0.7\text{cm}^2\text{g}^{-1}$ for DM-DM scattering cross section [34]). As will be shown in the following, terrestrial experiments impose a stringent bound on the DM-baryon scattering cross section (albeit the limit depends on DM mass).

- **Dark matter is stable.** Dark matter has lifetime as long as the age of the universe in order to explain all the astronomical and cosmological "missing matter" problems. This translates to a lower limit on its lifetime: $\tau_{\text{DM}} \gtrsim 14$ Gyr.

- **Dark matter behaves classically.** The fact that the observed behavior of dark matter is classical imposes a lower bound on the dark matter mass, as the de Broglie wavelength of DM cannot be as large as the size of galaxy ($m_{DM} \gtrsim 10^{-22}\text{eV}$).

- **Dark matter is not too heavy.** Dark matter would lead to the kinematic heating of the galactic disk if it is too heavy (see e.g. [35]). This leads to a limit $m_{DM} \lesssim 10^6 M_\odot$.

Phenomenological properties mentioned above still give us very little information about dark matter. Certain assumptions from the perspectives of particle physics and cosmology are required in order to strategize DM detection. Perhaps the simplest assumption is to assign DM a $Z2$ symmetry such that dark matter is stable at the cosmological

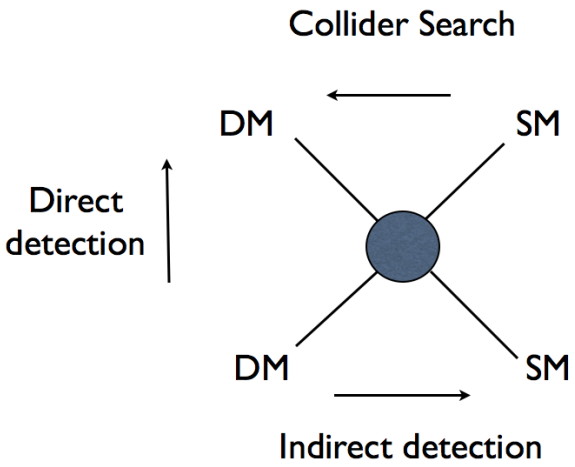

Figure 2.1: A sketch on approaches to uncovering particle properties of dark matter.

scale. Another typical assumption is that there exists a certain interaction between DM and visible sector such that the observed DM number density can be reproduced via this type of interaction. One class of dark matter candidates called weakly interacting massive particle (WIMP) in the literature indeed satisfies such conditions (or defined as so). Three types of interaction can be deduced straightforwardly from these minimal assumptions: DM-SM particle scattering, DM-DM annihilation to SM particles, and production of DM from the collision of SM particles. These are used to strategize WIMP detection. Fig. 2.1 summarizes schematically approaches to study the particle properties of dark matter utilizing these types of interaction. [1]

2.1 Direct detection

Dark matter propagates throughout our galactic halo. The maximum velocity the dark matter travels is fixed by the galactic escape velocity. DM particles may come in contact with the Earth and occasionally interact with the terrestrial baryons. The purpose of

[1] An example of non-WIMP dark matter is the axion, which is a by-product of the Peccei-Quinn solution to the strong CP problem. Another example is the super-weakly interacting massive particle (superWIMP), where its relic abundance gives the observed DM relic abundance assuming that the early universe satisfies certain condition (e.g. reheating temperature). Some aspects of superWIMP will be discussed in the following sections.

direct detection experiments is to look for such rare elastic scatterings of nuclei with dark matter by making experimental observation of the nuclei recoil. The scattering event rate is given by $R = N\langle\sigma_{\rm sca}v\rangle$, where N is the number of target nuclei in the detector. $\langle\sigma_{\rm sca}v\rangle$ accounts for dark matter number and velocity distributions as well as the scattering cross section. More accurately, the observable related to these experiments is the recoil energy E_r of the target nuclei. Below a certain threshold recoil energy E_0, the detector is insensitive to the dark matter-nucleon scattering. The differential event rate can then be written as

$$\frac{dR}{dE_r} = \frac{N\rho}{m_{\rm DM}} \int_{v_{min}}^{v_{max}} v f(\vec{v}) \frac{d\sigma}{dE_r}, \tag{2.1}$$

where ρ is the local dark matter density, and $f(\vec{v})$ is the dark matter velocity distribution (in the Earth frame) normalized to 1. v_{min} is the dark matter velocity that produces the threshold recoil energy E_0 while v_{max} is the dark matter escape velocity. Based on (2.1), we observe that the interpretation of direct detection experiments requires a good knowledge of detector responses as well as the understanding of astrophysics (dark matter velocity distribution), nuclear and particle physics (dark matter-nucleus scattering cross section).

There are spin-dependent and spin-independent contributions to the the differential scattering cross section. In general, for an elastic scattering between DM and a nucleus of proton number Z and nucleon number A, it can be written in the following form:

$$\frac{d\sigma}{dE_r} = \frac{m_A}{2\mu_A^2 v^2}(\sigma_0^{SD} S(q) + \sigma_0^{SI} F^2(q)). \tag{2.2}$$

m_A is the nucleus mass, and μ_A is the reduced mass of dark matter and the nucleus. $\sigma_0^{SD/SI}$ are the spin-dependent and spin-independent cross sections at zero momentum transfer $q = 0$. $S(q)$ and $F^2(q)$ are form factors describing the cross sections when there is non-zero momentum transfer. The form factors are determined from nuclear physics. They determine if the scattering is coherent with respect to all nucleons in the nucleus.

2.1.1 Spin-dependent scattering

Let us give a brief discussion of spin-dependent scattering.[2] Assuming that DM is a Majorana fermion χ, the spin-dependent contribution arises from the following Lagrangian at the quark level:

$$L = \alpha_{\rm DM}^q (\overline{\chi}\gamma^\mu\gamma_5\chi)(\overline{q}\gamma_\mu\gamma_5 q). \tag{2.3}$$

At the nucleon level, the Lagrangian can be parametrized as

$$L_N = (\overline{\chi}\gamma^\mu\gamma_5\chi)(\overline{N}s_\mu N) \sum_{q=u,d,s} 2\alpha_{\rm DM}^q \Delta_q^N, \tag{2.4}$$

[2] Here, we follow [36, 37] closely.

with $\langle n|\bar{q}\gamma_\mu\gamma_5 q|n\rangle = 2s_\mu^n\Delta_q^n$. The next step is to write the nuclear matrix element of the nucleon operator. The nuclear matrix element of the spin operator is just the average spin of protons and neutrons in the nucleus at zero transfer momentum. At non-zero momentum transfer, the coherence loss is accounted by the form factor. It is common, in correspondence to nuclear physics, to use the following notations:

$$a_p = \sum_{q=u,d,s} \frac{2\alpha_{\rm DM}^q}{\sqrt{2}G_F}\Delta_q^p, \qquad a_n = \sum_{q=u,d,s} \frac{2\alpha_{\rm DM}^q}{\sqrt{2}G_F}\Delta_q^n \tag{2.5}$$

$$a_0 = a_p + a_n, \qquad a_1 = a_p - a_n. \tag{2.6}$$

The differential cross section takes the following form:

$$\frac{d\sigma}{d|\mathbf{q}|^2} = \frac{8}{\pi v^2}\Lambda^2 G_F^2 J(J+1)\frac{S(|\mathbf{q}|)}{S(0)}. \tag{2.7}$$

The form factor $S(|\mathbf{q}|)$ is of the following form:

$$S(|q|) = a_0^2 S_{00}(q) + a_1^2 S_{11}(q) + a_0 a_1 S_{01}(q). \tag{2.8}$$

J is the total angular momentum of the nucleus. Λ is given by

$$\Lambda = (1/J)[a_p\langle S_p\rangle + a_n\langle S_n\rangle], \tag{2.9}$$

where $\langle S_n\rangle = \langle N|S_n|N\rangle$ is the expectation value of the spin of the neutron in the nucleus, and similarly for $\langle S_p\rangle$. We show in Table 2.1 several elements often used in direct detection experiments and values relevant to spin-dependent scattering.

2.1.2 Spin-independent scattering

For demonstration, we consider spin-independent scattering cross section arising from the Lagrangian of the following form (scalar and vector part):[3]

$$L = \alpha_q^S \overline{\chi}\chi\bar{q}q + \alpha_q^V \overline{\chi}\gamma_\mu\chi\bar{q}\gamma^\mu q. \tag{2.10}$$

Note that the above Lagrangian is symbolic, i.e. we do not specify the particle nature of dark matter. The differential scattering cross section in general reads

$$\left(\frac{d\sigma}{dE_r}\right)_{SI} = \frac{m_N\sigma_0 F^2(E_r)}{2\mu^2 v^2}. \tag{2.11}$$

The reduced mass, μ, is defined as follows:

$$\mu = \frac{m_{\rm DM}m_N}{m_{\rm DM}+m_N}. \tag{2.12}$$

[3]Here, we have ignored possible (effective) couplings between DM and gluon

Table 2.1: Elements and their atomic number Z, the total nuclear spin J, and the expectation values of the proton and neutron spins inside the nucleus $\langle S_{p,n} \rangle$. The nucleus is indicated whether it contains odd numbers of protons or neutrons. The relative sensitivities to spin-dependent interactions are also shown. Taken from [38].

Nucleus	Z	Odd Nuc.	J	$\langle S_p \rangle$	$\langle S_n \rangle$	$\frac{4\langle S_p \rangle^2 (J+1)}{3J}$	$\frac{4\langle S_n \rangle^2 (J+1)}{3J}$
^{19}F	9	p	1/2	0.477	-0.004	9.1×10^{-1}	6.4×10^{-5}
^{23}Na	11	p	3/2	0.248	0.020	1.3×10^{-1}	8.9×10^{-4}
^{27}Al	13	p	5/2	-0.343	0.030	2.2×10^{-1}	1.7×10^{-3}
^{29}Si	14	n	1/2	-0.002	0.130	1.6×10^{-5}	6.8×10^{-2}
^{35}Cl	17	p	3/2	-0.083	0.004	1.5×10^{-2}	3.6×10^{-5}
^{39}K	19	p	3/2	-0.180	0.050	7.2×10^{-2}	5.6×10^{-3}
^{73}Ge	32	n	9/2	0.030	0.378	1.5×10^{-3}	2.3×10^{-1}
^{93}Nb	41	p	9/2	0.460	0.080	3.4×10^{-1}	1.0×10^{-2}
^{125}Te	52	n	1/2	0.001	0.287	4.0×10^{-6}	3.3×10^{-1}
^{127}I	53	p	5/2	0.309	0.075	1.8×10^{-1}	1.0×10^{-2}
^{129}Xe	54	n	1/2	0.028	0.359	3.1×10^{-3}	5.2×10^{-1}
^{131}Xe	54	n	3/2	-0.009	-0.227	1.8×10^{-4}	1.2×10^{-1}

Form factor

Let us first discuss the form factor $F(E_r)$. When the transfer momentum q is zero, every nucleon in the nucleus scatters equally with DM. However, when q is not zero, DM resolves the internal structure of the nucleus and causes the loss of coherence of scattering.

The form factor $F(q)$, with q equivalent to the transferred momentum ($q = \sqrt{2m_N E_r}$ at the non-relativistic limit), is defined as

$$F(q) = \frac{1}{A(2\pi)^{3/2}} \int \rho(\vec{r}) e^{-i\vec{q}.\vec{r}} d^3r. \tag{2.13}$$

$\rho(\vec{r})$ is the charge density and A is the proton number of the nucleus. One way to parametrize the form factor is using the so-called Helm form factor [42]:

$$F(q) = \frac{3j_1(qR_1)}{qR_1} e^{-\frac{1}{2}q^2s^2}, \tag{2.14}$$

where j_1 is the 2nd spherical Bessel function and $R_1 = \sqrt{c^2 + 7\pi^2a^2/3 - 5s^2}$, with c, a and s determined from nuclear physics data.

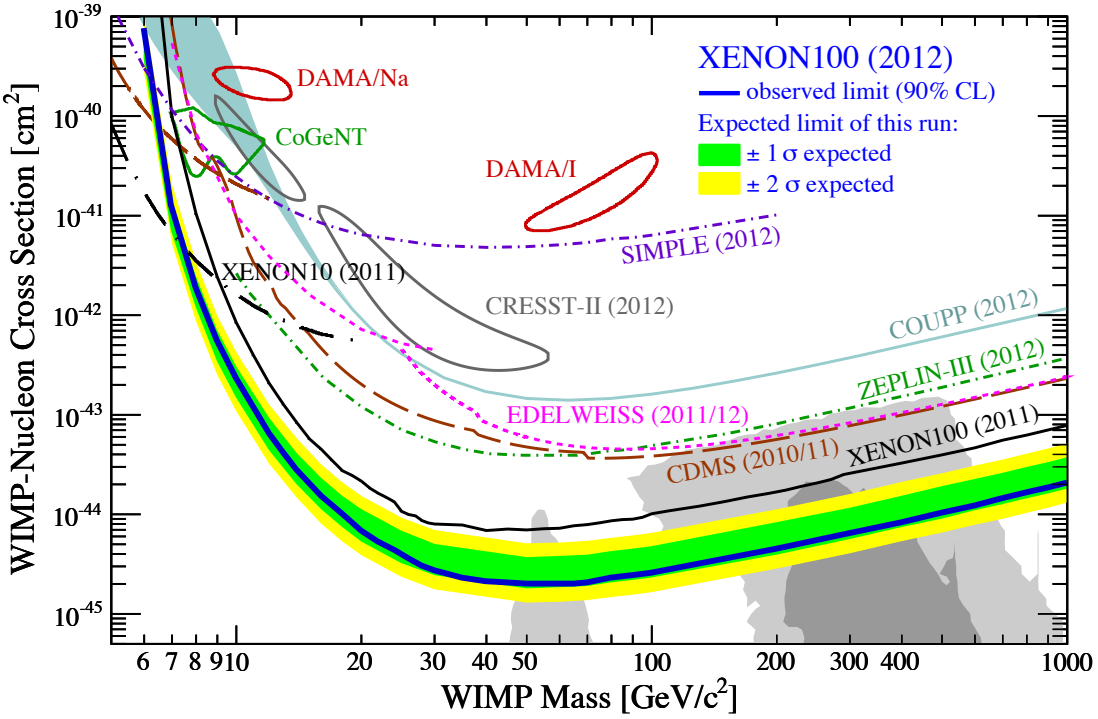

Figure 2.2: Results on spin-independent dark matter-nucleon scattering (at 90% CL) together with the regions ($1\sigma/2\sigma$) preferred by supersymmetric (CMSSM) models. Taken from [39]. See [39] for details.

Hadronic matrix elements

The vector part of the spin-independent scattering as in Eq. (2.10) does not receive any contribution from sea quarks and gluons. This is because the vector current conserves charge. Only valence quarks contribute and σ_0 in Eq. (2.11) is

$$\sigma_0^V \propto \mu^2 \left[\alpha_u^V (A+Z) + \alpha_d^V (2A-Z)\right]^2 , \tag{2.15}$$

where the coefficient depends on the nature of dark matter (scalar, Dirac fermion etc.), of which we will go through next Chapter. For the scalar part of Eq. (2.10), it is a bit more complicated. We follow closely those presented in [43]. The σ_0 in Eq. (2.11) reads

$$\sigma_0^S \propto \mu^2 \left[Z f_p + (A-Z) f_n\right]^2 , \tag{2.16}$$

where

$$\frac{f_n}{m_n} = \sum_{q=u,d,s} f_{T_q}^{(n)} \frac{\alpha_q^S}{m_q} + \frac{2}{27} f_{T_G}^{(n)} \sum_{q=c,b,t} \frac{\alpha_q^S}{m_q} \tag{2.17}$$

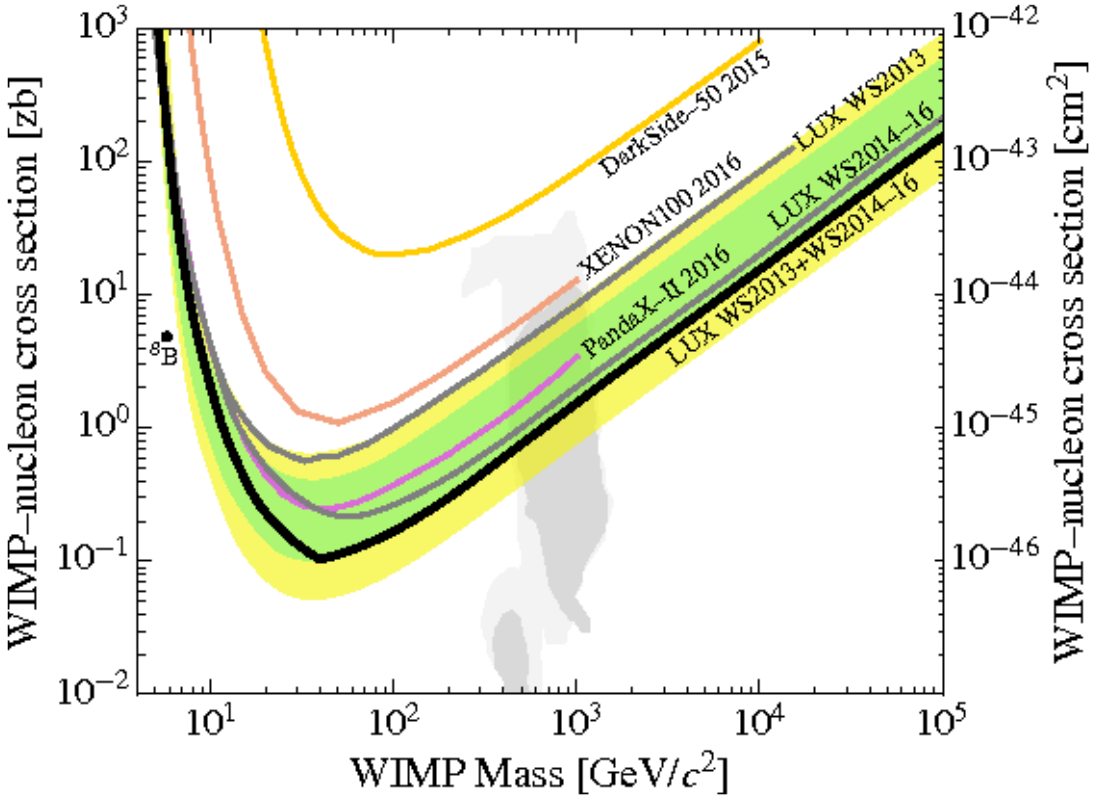

Figure 2.3: Results on spin-independent dark matter-nucleon scattering (at 90% CL) together with the regions ($1\sigma/2\sigma$) preferred by supersymmetric (CMSSM) models at the sensitivity frontier. Also shown are limits obtained by XENON100 (red), DarkSide-50 (orange), and PandaX-II. Taken from [40].

and similarly for f_p. f_T's are parametrized as:

$$m_N f_{T_q}^{(N)} = \langle N|m_q \bar{q}q|N\rangle \equiv m_q B_q^{(N)}, \tag{2.18}$$

and

$$f_{TG}^{(N)} = 1 - \sum_{q=u,d,s} f_{T_q}^{(N)}. \tag{2.19}$$

Using isospin symmetry of proton/neutron, the scalar matrix elements ($B_q^{(n)}$ and $B_q^{(p)}$) can be related to each other as follows:

$$B_u^{(n)} = B_d^{(p)}, \qquad B_d^{(n)} = B_u^{(n)}, \qquad B_s^{(n)} = B_s^{(p)}. \tag{2.20}$$

The B's are related to the pion-nucleon sigma, $\Sigma_{\pi N}$ as follows

$$\Sigma_{\pi N} \equiv \frac{1}{2}(m_u + m_d) \times \left(B_u^N + B_d^N\right). \tag{2.21}$$

	LQCD	Experiment	
f_{Tu}	0.0190 ± 0.0029	0.0308 ± 0.0061	[44], [45]
f_{Td}	0.0246 ± 0.0037	0.0459 ± 0.0089	[44], [45]
f_{Ts}	0.043 ± 0.011	0.493 ± 0.159	[46], [45]

Table 2.2: Values of f_T's determined with lattice QCD (LQCD) and from experiment. Taken from [47].

We show in Table 2.1.2 values and uncertainties related f_T's.

2.1.3 Astrophysical aspects of direct detection

DM has a relative velocity of order 100 km/s with respect to our Earth. Thus, the DM-nucleus scattering is non-relativistic and E_r can be written as, in the DM-nucleus center-of-mass frame,

$$E_r = \frac{\mu^2 v^2}{m_N}(1 - \cos\theta), \tag{2.22}$$

where θ is the scattering angle in the DM-nucleon center-of-mass frame.At $\theta = \pi$, the momentum transfer is the largest, and it corresponds to the minimum speed required to scatter at a given recoil energy E_r:

$$v_{min} = \sqrt{\frac{m_N E_r}{2\mu^2}}. \tag{2.23}$$

μ is the reduced mass. Since the speed of DM is not arbitrarily large, i.e cannot be larger than the escape velocity, the low energy threshold of the detectors limit DM detection to a certain DM velocity range. This is especially important when one tries to interpret results of XENON100, which in the conventional cases, has no sensitivity at the low mass region.

All information of the DM velocity distribution can be represented by $g(v_{min})$:

$$g(v_{min}) \quad = \quad \int_{v>v_{min}} \frac{1}{v} f_e(\vec{v}, t) d^3 v. \tag{2.24}$$

$\vec{v}$ can be divided into $\vec{v_e} + \vec{v}$. Here, $\vec{v}$ is the DM velocity in the Earth's frame, and $\vec{v_e}$ is the Earth's velocity in the galactic halo's rest frame, which, following [48], reads

$$v_e = v_\odot + v_{\rm orb} \cos\gamma \cos[\omega(t - t_0)]. \tag{2.25}$$

The DM velocity distribution (relative to the rest frame of the galactic halo) is usually assumed to be Maxwellian/isothermal. This is called the Standard Halo Model (SHM)

and has the form:

$$f_{SHM}(\vec{v}) = \begin{cases} \frac{1}{Nv_0^3\pi^{3/2}} e^{-v^2/v_0^2}, & v < v_{\rm esc} \\ 0, & \text{otherwise} \end{cases} \tag{2.26}$$

v_0 is the mean DM velocity relative to the rest frame of the galactic halo. N is the normalization factor:

$$N = \text{erf}\left(\frac{v_{\rm esc}}{v_0}\right) - \frac{2v_{\rm esc}}{v_0\sqrt{\pi}} e^{-v_{\rm esc}^2/v_0^2}. \tag{2.27}$$

We quote the following values from [48] : $v_0 = 220$ km/s, $v_\odot = 232$ km/s, $v_{\rm esc} = 544$ km/s, $v_{\rm orb} = 30$ km/s, $\rho = 0.3$ GeV/c^2/cm^3, $\cos\gamma = 0.51$.

In recent years, some experimental groups have claimed to observe spin-independent dark matter-nucleon scattering events (DAMA/LIBRA [49], CoGeNT [50, 51] and CRESST [52], CDMS-II Si [53]).However, their results remain debatable as the viable parameter regions are in tension with each other. Moreover, other experiments such as XENON100 [39] and LUX [54] have ruled out most parameter regions claimed to be yielding positive results. We show in Fig. 2.2 and 2.3 several recent results of direct detection experiments.

2.2 Indirect detection

Dark matter may decay or annihilate into SM particles. This provides an opportunity to detect signals of dark matter in the form of cosmic rays. These cosmic rays can either be primary products of dark matter annihilation/decay or secondary products from primary SM particles. Their fluxes are proportional to $\rho^2\langle\sigma_{\rm ann}v\rangle$ for annihilating dark matter with velocity-averaged annihilation cross section $\langle\sigma_{\rm ann}v\rangle$ and $\rho\Gamma_{\rm dec}$ for decaying dark matter with decay rate $\Gamma_{\rm dec}$. The bound on annihilating dark matter is often compared with the canonical annihilation cross section of thermally produced dark matter.

2.2.1 Gamma rays

Dark matter may annihilate into quarks or leptons which undergo cascade decay producing a continuous energy spectrum of gamma rays. Detections of gamma rays are straightforward as they propagate in the space unaffected by galactic magnetic fields. For gamma rays, the relevant quantity is the flux, $\phi(E,\psi)$, of which comes from a direction of observation ψ integrated over a solid angle $\Delta\Omega$. For annihilating (particle-antiparticle) dark matter, writing $N(E)_\gamma$ as the gamma-ray energy spectrum per annihilation,

$$\phi(E,\psi) = \frac{\langle\sigma_{\rm ann}v\rangle}{8\pi m_{\rm DM}^2} N(E)_\gamma \int_{l.o.s.,\Delta\Omega} dl\ d\Omega\rho^2[l(\psi)], \tag{2.28}$$

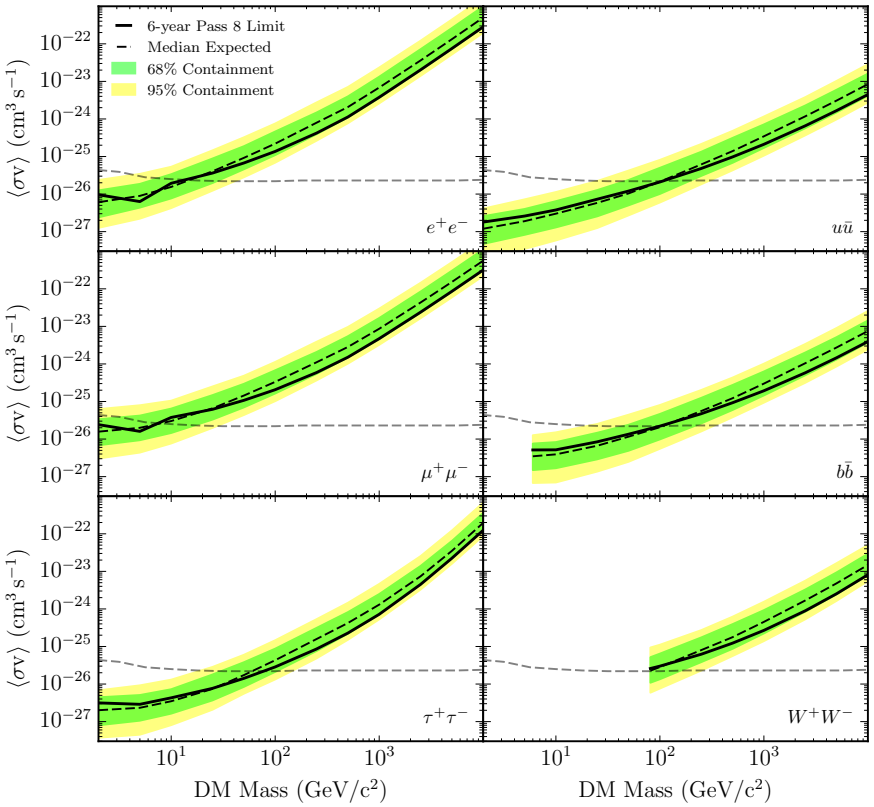

Figure 2.4: Upper limit on $\langle\sigma_{\rm ann}v\rangle$ assuming that dark matter annihilates into various channels. The shaded region is due to uncertainties of the combined dSphs dark matter density profile. The horizontal dashed line is the canonical annihilation cross section for thermal dark matter. Taken from [55].

where the integration is performed over the line of sight (l.o.s). Note that there is an additional factor of 1/2 for the case where DM is self-conjugate. The integral is called the J-factor. It is dependent on the dark matter mass distribution of the astrophysical target of interest.

Dwarf spheroidal galaxies are excellent targets for indirect detection. These objects are dominated by dark matter and their astrophysical background is minimal. The total mass of dark matter inside the system is deduced from the velocity dispersion of the stars in the system. This information allows experimentalists to deduce the upper limit of the annihilation cross section of dark matter. In Fig. 2.4, we show constraints on the annihilation cross section based on the gamma-ray flux from these galaxies, assuming various annihilation channels [55]. The experiment was performed using the Fermi Large Area Telescope (LAT).

In recent years, there have been curious signatures originated from the observation of the spectral and morphological distribution of gamma rays from the Galactic Center [56, 57]. Furthermore, WMAP has observed excess microwave emission from the Galactic Center ("WMAP" Haze) [58]. The Fermi Gamma-Ray Space Telescope has also seen excess of gamma rays at high latitudes ("Fermi Bubble"), which is thought by some to be related to the WMAP haze. While these phenomena could be of astrophysical origin, they have also been interpreted as hints from dark matter. In addition, observed hard synchrotron emission from the Inner Galaxy's radio filament has been interpreted as synchrotron emission of energetic SM particles as a result annihilation/decay of dark matter [59]. Galactic Center gamma rays, the WMAP haze and the synchrotron emission from the Inner Galaxy's radio filament can be explained simultaneously by dark matter of mass ~ 10 GeV [60]. However, dark matter models inspired by these phenomena are under serious reconsideration due to stringent constraints from antiproton and positron flux measurements.

Aside from continuum gamma rays, monochromatic gamma-ray line, if observed, could be a smoking gun signature of dark matter. Such signal are recently found to be coming from the Galactic Center at 130 GeV [61, 62]. If it is to be interpreted as a signal from the annihilation (decay) of dark matter, its annihilation cross section (decay lifetime) into gamma rays is around 10^{-27} cm^{3}s^{-1} (10^{28} s). The interpretation of the gamma-ray line remains tentative and further investigation and inspection are needed before one makes any conclusion. See, e.g. [63, 64] for theoretical works on possible dark matter models that could generate this signal.

Excess of 511 keV from the Galactic Center has also been reported [65, 66]. This has been speculated as MeV-scale dark matter that produces e^+ e^- which, in turn annihilate into 511 keV gamma rays [67]. Dark matter model with an MeV-scale excited state has also been proposed [68]. We note that again, there is no confirmation of such speculations yet.

More recently, monochromatic line has been discovered by two independent groups looking for X-ray line emissions originated from galaxy clusters as well as Andromeda galaxy [69, 70]. It has been found that there is an excess of X-ray emissions at around 3.5 keV, which has no explanation with known physics. Although it remains debatable regarding the source of the X-ray, more experimental works are needed to rule out the possibility of explaining it as dark matter. See, e.g. [71] for a possible dark matter model explaining the anomaly.

2.2.2 Neutrinos

We now discuss briefly neutrino signals from dark matter. Detection of neutrino is always straightforward because the propagation of neutrino is unaffected by galactic magnetic fields. Teresterial neutrino detection is basically based on Cherenkov light (observed

via photomultiplier) produced when there is charged-current scattering of neutrino with nucleon or electron. Neutrino detection usually involves detector volume of enormous size due to its extremely weak interaction. The current leading neutrino detection experiment is the Icecube experiment located at the Antarctica [72].

Results from neutrino detection can be utilized to impose bounds on the spin-dependent scattering cross section of dark matter captured in the sun [73]. The more exciting prospect is perhaps the possibility of detecting energetic neutrinos directly from the annihilation/decay of dark matter. Interestingly, Icecube detectors at the Antarctica have seen anomalous neutrino events of energy $O(100 - 1000)$ TeV that could not be accounted for by the background [74]. There have been theoretical progresses suggesting that these events could be coming from the decay of dark matter [75, 76].

2.2.3 Charged particles

We now discuss indirect detection of charged particles. There are several processes that affect the propagation of charged particles in the galaxy. The propagation equation can be constructed from these processes:

$$\frac{\partial N_i}{\partial t} = \sum_{\text{processes}} f(N_i, ...). \tag{2.29}$$

N_i is the number of charged particle of interest. the function f can depend on other variables such as energy, position etc.

The most important processes are as follows:

$$\frac{\partial N_i}{\partial t} = D(E)\Delta N_i + \frac{\partial}{\partial E}(b(E)N_i) + Q(\vec{x}, E, t). \tag{2.30}$$

The first term accounts for the diffusion of the charged particle. The second one is energy loss. The third term indicates all sources of the charged particle.

It is vital to fix the boundary condition when solving this differential equation. The boundary is often chosen in the shape of cylinder, of which the meaning is clear as it is the shape of the galaxy. Beyond the boundary, the typical assumption is that particles can escape freely.

Parameters in Eq. (2.30) are determined using observational data. We note that as compared to vigorous astrophysical activities that are involved in the production of cosmic rays, dark matter, whether through annihilation or decay, has subdominant contribution to the energy density of cosmic ray. Hence, using the boron-to-carbon ratio, one can determine parameters involved in the propagation of cosmic rays.

This does not mean that there is no hope of detecting any trace of dark matter from charged particles. Matter that is rarely produced in astrophysical phenomena, such as positron, antiproton and anti-deuterium are excellent target candidates of indirect

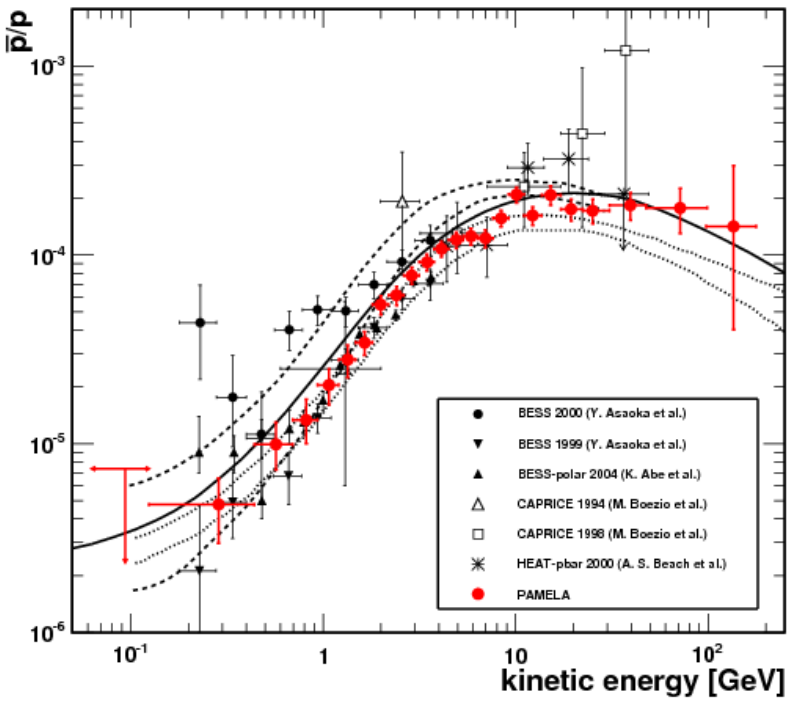

Figure 2.5: $\overline{p}/p$ and theoretical prediction of the secondary-only production of antiprotons during the propagation of cosmic rays in the galaxy. Taken from [77].

detection of dark matter. Dark matter annihilation or decay produces, except in special cases, equal amount of ordinary and antiparticles.

We first discuss antiproton cosmic ray. The main astrophysical production is via

$$p + p \to p + p + \overline{p} + p. \tag{2.31}$$

Such process is called spallation. It also applies to other antimatter. Note that the threshold energy of this process is around 10 GeV (a high-energy proton hitting a proton in the interstellar medium, for example). As we can see from Figure 2.5 from the PAMELA experiment, antiprotons do not lose much of its energy during propagation. This in fact makes antiproton a good candidate for dark matter indirect detection as any significant cutoff in the energy spectrum could hint at products of dark matter annihilation or decay. The measurement of the flux of antiproton cosmic ray, however, has yielded good agreement between astrophysical theory and observation [77]. See Fig. 2.7 for the recent measurement of antiproton flux from AMS-2 [78].

As is well known, PAMELA and, more recently, AMS-02 have obtained indisputable data that indicate that there is an excess of positrons in cosmic rays [79, 80]. There have

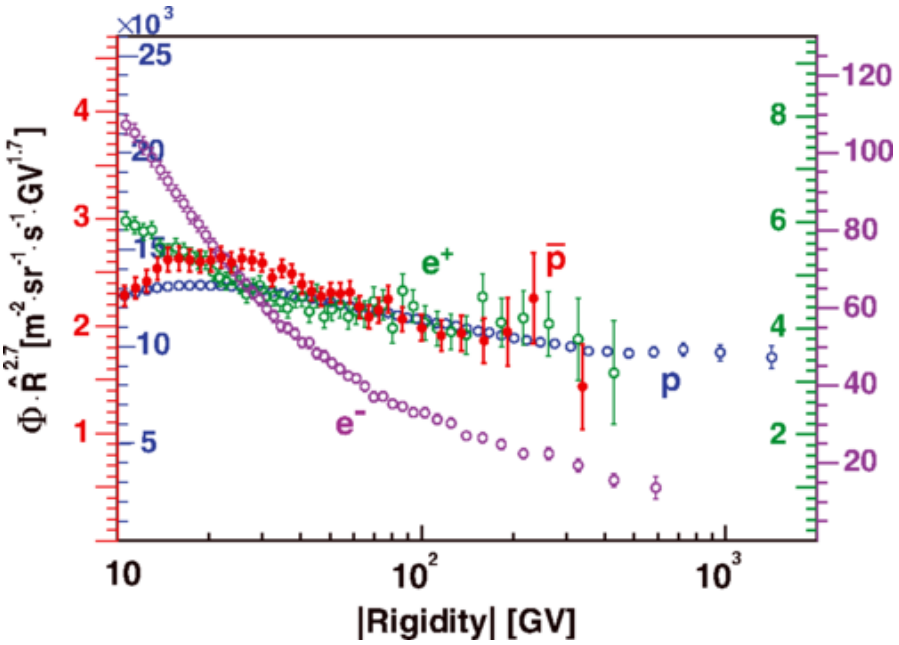

Figure 2.6: Measured fluxes of various particles with respect to rigidity, defined as the particle momentum divided by charge. antiproton flux (red, left axis) compared to the proton flux (blue, left axis), electron flux (purple, right axis), and positron flux (green, right axis). Taken from [78].

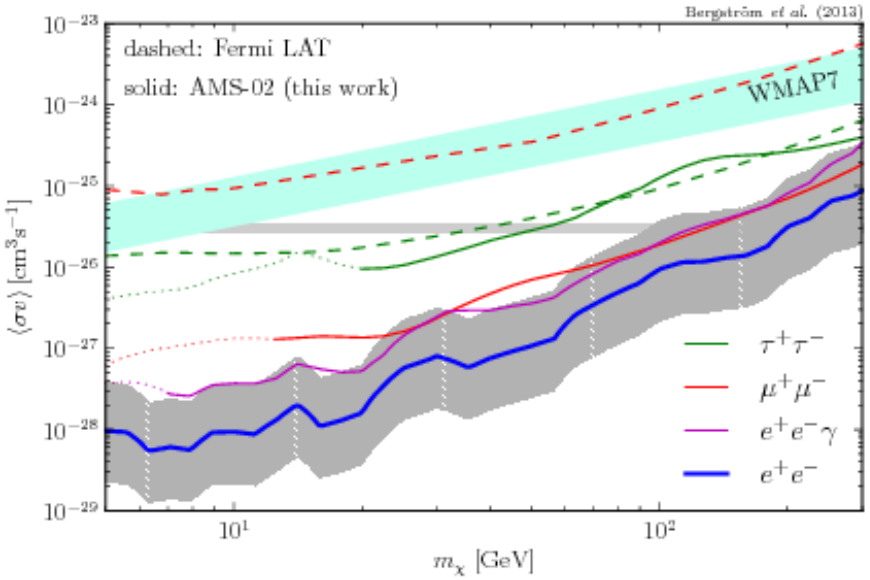

Figure 2.7: Upper limits on annihilation cross section of dark matter, assuming various leptonic channels (solid lines). Also shown are limits from Fermi LAT gamma-ray constraints assuming various leptonic channels (dashed lines) and WMAP7 CMB constraints (light blue band). Taken from [81].

been many papers on its interpretation as dark matter, but it is generally difficult as dark matter must annihilate/decay dominantly into lepton pairs as there is no excess of antiproton. The annihilation cross section must be very large to explain the positron anomaly, 10^3 larger than the canonical annihilation cross section.

At lower energy, the high-quality AMS-02 data have enabled physicists to impose upper limits of dark matter annihilation cross section or decay rate [81]. Any significant rate of annihilation/decay of dark matter at around 10 GeV into electrons/positrons would appear clearly as a bump on the smooth energy spectrum. As we can see in Fig. 2.7, the limits are reaching the canonical value at energy as high as 100 GeV.

2.3 Collider searches

Dark matter may be produced at colliders and this is a potentially powerful complementary probe to searches for DM in direct and indirect detection experiments as mentioned above. The searches for DM at colliders have been focused on popular models of beyond the Standard Model physics where DM is involved, such as supersymmetry (SUSY).

However, the idea that the LHC can search for DM in more general classes of theories and interactions has gained attention. It has been studied and shown quite a while ago

that can constrain DM models via a jet, photon or Z-boson recoiling off missing energy originated from DM [82–85]. More recently, the advents of Tevatron and the LHC have led to studies of DM models utilizing the effective field theory (EFT), where one can cast bounds on models by comparing directly the constraints from colliders with results from direct and indirect detection experiments [86–92]. The energy scale in relation with direct and indirect detection experiments is often negligible as compared to the energy scale of the full model, where particles other than DM and SM particles in the UV-complete model can be integrated out while studying direct and indirect detection constraints. One can then compare these results with a bound on the scale of the EFT operator, Λ derived from collider searches. The effective operators are often labelled following [87, 88] and are shown in Table 2.3. These non-renormalizable operators are suppressed by a scale M_*, which is related to the UV-complete model of dark matter. We note that for operators D1-5, M1-M4, C1-2, R1-2, it is implicitly assumed that the coefficients of these effective operators are proportional to the quark mass in order to achieve minimal flavor violation. Perhaps for the reason of this simplicity of comparison to direct and indirect detection experiments, DM searches at the Large Hadron Collider (LHC) have gained popularity, and the EFT framework has been utilized in many LHC searches.

However, it is clear that the energy scale of collision processes probed at colliders such as the LHC is in general beyond the values of Λ that can be bounded, rendering the EFT characterization of DM searches at colliders invalid in many cases. In general, One integrates out heavy mediators at a scale Λ in the UV-complete theory in order to generate effective operators for various studies. One can only derive the constraints on Λ derived self-consistently if the processes used to constrain the theory have energy scale smaller than Λ. Further discussions and more detailed analyses of this issue can be found in [93–102]. For this reason, the collider limits obtained using the EFT approach cannot be reliably used, for example, to compare with limits obtained from direct detection experiments.

These statements are especially true once constraints on the mediating particle are taken into account, generally forcing one out of the regime of validity of the EFT (*e.g.* [99, 102]). For example, dijet searches for the particle mediating the DM production place such strong constraints on the quark-mediator coupling that, in order for the DM-mediator coupling to be perturbative but still constrained by mono-jet searches, the mediator must, in most cases, be produced on-shell.

Therefore, in order to interpret DM search results at colliders adequately, simplified models should be employed. Simplified models are UV-complete models that do not necessarily represent the full theory, but enable one to study the kinematics and topologies of DM production at the LHC in a precise manner. Moreover, the sensitivity comparisons between collider and direct detection limits can be performed accurately.

Name	Operator	Coefficient
D1	$\overline{\chi}\chi\overline{q}q$	m_q/M_*^3
D2	$\overline{\chi}\gamma^5\chi\overline{q}q$	im_q/M_*^3
D3	$\overline{\chi}\chi\overline{q}\gamma^5 q$	im_q/M_*^3
D4	$\overline{\chi}\gamma^5\chi\overline{q}\gamma^5 q$	m_q/M_*^3
D5	$\overline{\chi}\gamma^\mu\chi\overline{q}\gamma_\mu q$	$1/M_*^2$
D6	$\overline{\chi}\gamma^\mu\gamma^5\chi\overline{q}\gamma_\mu q$	$1/M_*^2$
D7	$\overline{\chi}\gamma^\mu\chi\overline{q}\gamma_\mu\gamma^5 q$	$1/M_*^2$
D8	$\overline{\chi}\gamma^\mu\gamma^5\chi\overline{q}\gamma_\mu\gamma^5 q$	$1/M_*^2$
D9	$\overline{\chi}\sigma^{\mu\nu}\chi\overline{q}\sigma_{\mu\nu}q$	$1/M_*^2$
D10	$\overline{\chi}\sigma_{\mu\nu}\gamma^5\chi\overline{q}\sigma_{\alpha\beta}q$	i/M_*^2
D11	$\overline{\chi}\chi G_{\mu\nu}G^{\mu\nu}$	$\alpha_s/4M_*^3$
D12	$\overline{\chi}\gamma^5\chi G_{\mu\nu}G^{\mu\nu}$	$i\alpha_s/4M_*^3$
D13	$\overline{\chi}\chi G_{\mu\nu}\tilde{G}^{\mu\nu}$	$i\alpha_s/4M_*^3$
D14	$\overline{\chi}\gamma^5\chi G_{\mu\nu}\tilde{G}^{\mu\nu}$	$\alpha_s/4M_*^3$

Name	Operator	Coefficient
M1	$\overline{\chi}\chi\overline{q}q$	$m_q/2M_*^3$
M2	$\overline{\chi}\gamma^5\chi\overline{q}q$	$im_q/2M_*^3$
M3	$\overline{\chi}\chi\overline{q}\gamma^5 q$	$im_q/2M_*^3$
M4	$\overline{\chi}\gamma^5\chi\overline{q}\gamma^5 q$	$m_q/2M_*^3$
M5	$\overline{\chi}\gamma^\mu\gamma^5\chi\overline{q}\gamma_\mu q$	$1/2M_*^2$
M6	$\overline{\chi}\gamma^\mu\gamma^5\chi\overline{q}\gamma_\mu\gamma^5 q$	$1/2M_*^2$
M7	$\overline{\chi}\chi G_{\mu\nu}G^{\mu\nu}$	$\alpha_s/4M_*^3$
M8	$\overline{\chi}\gamma^5\chi G_{\mu\nu}G^{\mu\nu}$	$i\alpha_s/8M_*^3$
M9	$\overline{\chi}\chi G_{\mu\nu}\tilde{G}^{\mu\nu}$	$i\alpha_s/8M_*^3$
M10	$\overline{\chi}\gamma^5\chi G_{\mu\nu}\tilde{G}^{\mu\nu}$	$\alpha_s/8M_*^3$

Name	Operator	Coefficient
C1	$\chi^\dagger\chi\overline{q}q$	m_q/M_*^2
C2	$\chi^\dagger\chi\overline{q}\gamma^5 q$	im_q/M_*^2
C3	$\chi^\dagger\partial_\mu\chi\overline{q}\gamma^\mu q$	$1/M_*^2$
C4	$\chi^\dagger\partial_\mu\chi\overline{q}\gamma^\mu\gamma^5 q$	$1/M_*^2$
C5	$\chi^\dagger\chi G_{\mu\nu}G^{\mu\nu}$	$\alpha_s/4M_*^2$
C6	$\chi^\dagger\chi G_{\mu\nu}\tilde{G}^{\mu\nu}$	$i\alpha_s/4M_*^2$
R1	$\chi^2\overline{q}q$	$m_q/2M_*^2$
R2	$\chi^2\overline{q}\gamma^5 q$	$im_q/2M_*^2$
R3	$\chi^2 G_{\mu\nu}G^{\mu\nu}$	$\alpha_s/8M_*^2$
R4	$\chi^2 G_{\mu\nu}\tilde{G}^{\mu\nu}$	$i\alpha_s/8M_*^2$

Table 2.3: Effective operators of DM coupling to SM particles. The operator names beginning with D, M, C, R refer to DM that are Dirac fermions, Majorana fermions, complex scalars or real scalars respectively.

Simplified models immediately suggest that other signatures, apart from looking for DM recoiling against a visible SM particle, must be considered. Searching directly for the mediator of the SM-DM interaction may generally be more powerful for constraining the parameter space. For example, returning to the earlier example, assuming that the mediator is coupled to both quarks and DM, where the monojet search is expected to be important, models with t-channel DM production (squark mediator) are constrained by jets plus missing transverse energy (MET) searches, while models with s-channel DM production (Z' mediator) are constrained by dijet searches. Various aspects of such simplified models have been studied extensively in the literature [96–104]. [4]

2.4 A final remark

As reviewed above, even though DM direct/indirect detection experiments have looked for DM signals extensively, there is no concrete observational evidence of DM interacting with SM particles. One might wonder if there exists WIMP that can escape (almost) all the detection strategies mentioned above. Let us remind the readers that postulate of the existence of WIMP is motivated by the fact it can be produced thermally via SM-DM interactions (without modifying early-universe conditions). It is then of interest to question if there is any WIMP with almost-vanishing SM-DM interaction, yet it could be produced thermally to match the cosmologically observed DM abundance. We will review the calculation of DM relic abundance in the next Chapter and reveal that, the so-called coannihilation scenario has such a property.

[4] For a comprehensive list of references, see [105–107].

Chapter 3

Relic density of dark matter

Calculating the evolution of number density of dark matter with respect to time is crucial in order to predict its relic abundance at present. Essentially, the evolution is governed by the Boltzmann equation. In the early studies of particle cosmology, only the DM self annihilation cross section is considered to be important in calculating the relic abundance. Later, it has been shown that the interaction of exotic particles other than dark matter can also be important if their masses are close to that of the dark matter. In certain limits, the relic abundance of dark matter is completely determined by the properties of the exotic particles. This so-called coannihilation process will be an important topic studied in detail throughout this thesis.

In the first part of this chapter, we discuss how the Boltzmann equation is solved to obtain the relic abundance of dark matter. Since the early universe is basically a thermal bath of particles, thermal average needs to be taken when considering the dynamics of the particles in the thermal bath. The second part of this chapter is dedicated to the description of thermal averaging. In the final part, we study how the effects of coannihilation change the usual prediction of the relic abundance.

3.1 The Boltzmann equation

Let us describe the Boltzmann equation governing the evolution of the DM number density. We first give a qualitative discussion of DM number density evolution.

The standard description of the early universe is that there exists a stage of reheating and particle production at the end of inflation. The temperature of the early universe is so high that all particles are in thermal equilibrium (if the particle mass is not larger than the reheating temperature, or the interaction rate is not too low), and the energy density of the universe is dominated by radiation (radiation dominated era). As the universe expands, the temperature (which is common for all particles in the equilibrium) decreases as the momentum of particles gets redshifted away.

The number density of a certain particle X is governed by inelastic interactions that annihilate or produce it. For simplicity, let us assume two-to-two scattering of X with another particle Y which is lighter than X: $XX \leftrightarrow YY$.[1] At high temperature, both the annihilation and production processes of X are at a rate high enough to keep the particles in the equilibrium. Once the temperature falls below the mass of X, it is more difficult for Y to annihilate into X as most of the Y particles do not have enough kinetic energy to produce X. Then, the number density of X can no longer be kept in equilibrium, or in other words, the production rate of X can no longer compete with the expansion rate of the universe. The number density of X in a comoving volume is conserved if there is no other process that can produce X. Then, X is said to have undergone "freeze out". This typically occurs at temperature $T \simeq m_X/20$.

The Boltzmann equation governing the number density of X, n_X, for the simple system mentioned above can be written as follows:

$$\frac{dn_X}{dt} + 3Hn_X = -\langle\sigma v_{rel}\rangle_{XX\to YY} n_X^2 + \langle\sigma v_{rel}\rangle_{YY\to XX} n_Y^2, \tag{3.1}$$

where $\langle\sigma v_{rel}\rangle$ is the thermally averaged annihilation cross section times velocity. Let us invoke the principle of detailed balance, $\langle\sigma v_{rel}\rangle_{XX\to YY} n_X^{eq2} = \langle\sigma v_{rel}\rangle_{YY\to XX} n_Y^{eq2}$, where n^{eq} is the number density in thermal equilibrium. Furthermore, assuming that Y is always in equilibrium within the period of time in consideration, $n_Y = n_Y^{eq}$, the Boltzmann equation can be rewritten as

$$\frac{dn_X}{dt} + 3Hn_X = -\langle\sigma v_{rel}\rangle_{XX\to YY}(n_X^2 - n_X^{eq2}). \tag{3.2}$$

The equation can be understood as follows: the rate of change in the total number of X in a comoving volume, na^3 is controlled by its annihilation rate ($-\langle\sigma v_{rel}\rangle n^2$) as well as its production rate ($\langle\sigma v_{rel}\rangle n^{eq2}$). Note that the era of universe in consideration is radiation-dominated.

In order to solve the Boltzmann equation, it is convenient to change the variable to remove the second term in the LHS of Eq. (3.2). Let us define $Y = n_X/s$, where s is the entropy density. The total entropy per comoving volume is conserved if there is no entropy release: $d(sa^3)/dt = 0$, implying $ds/dt = -3Hs$. Hence, Eq. (3.2) can be rewritten as:

$$\frac{dY}{dt} = -s\langle\sigma v_{rel}\rangle(Y^2 - {Y_{eq}}^2). \tag{3.3}$$

Furthermore, it is easier to track the evolution of Y using the temperature of the system. The derivative dT/dt can be derived using the properties of s. As described

[1] Here, we assume the antiparticle of X is itself. We will discuss the case where X annihilates with $\overline{X}$ in later chapters.

briefly in Section, the Hubble constant in a radiation-dominated flat universe is:

$$H^2 = \frac{8\pi\rho}{3}, \tag{3.4}$$

where $\rho = g_*(T)\frac{\pi^2}{30}T^4$. The effective degree of freedom $g_*(T)$ is given as:

$$g_*(T) = \sum_{i=boson} g_i(T_i/T)^4 + (7/8)\sum_{i=fermions} g_i(T_i/T)^4, \tag{3.5}$$

where T_i is the temperature of the particle with T the temperature of the photon (or heat bath). Moreover, the entropy density is written as:

$$s = g_{*s}(T)\frac{2\pi^2}{45}T^3, \tag{3.6}$$

with the effective degree of freedom $g_{*s}(T)$ given as:

$$g_{*s}(T) = \sum_{i=boson} g_i(T_i/T)^3 + (7/8)\sum_{i=fermions} g_i(T_i/T)^3. \tag{3.7}$$

Then, $dT/dt = (dT/ds)(ds/dt) = (45/6\pi^2T^2g^s_{eff}(T))(-3Hs)$. We also define the dimensionless quantity:

$$x \equiv m/T, \tag{3.8}$$

where m is the mass of dark matter. Then, Eq. (3.3) can be rewritten as:

$$\frac{dY}{dx} = -\frac{xs}{H(m)}(1 - \frac{x}{3g_{*s}}\frac{dg_{*s}}{dx})\langle\sigma v_{rel}\rangle(Y^2 - {Y_{eq}}^2), \tag{3.9}$$

where

$$H(m) \equiv H(T)x^2 = \sqrt{\frac{4\pi^3 G g_*}{45}}m^2. \tag{3.10}$$

3.2 Thermal averaging

Let us write down the full form of the term $\langle\sigma v_{rel}\rangle$. We follow the method presented in [108] closely. For a process involving incoming particles 1 and 2 with common mass m, the annihilation cross section can be written as:

$$\sigma v_{rel} = \frac{1}{4E_1E_2}\int d\,LIPS\,|\mathcal{T}|^2, \tag{3.11}$$

where $d\,LIPS$ is the Lorentz invariant phase space, given by

$$d\,LIPS \equiv (2\pi)^4\delta^4\left(p_1 + p_2 - \sum_j p_j\right)\prod_i \frac{d^3p_i}{(2\pi)^3}\frac{1}{2p_i^0}, \tag{3.12}$$

where the sum and product are over final-state particles. The term $|\mathcal{T}|^2$ is the matrix element squared for the process in consideration, with spin, color and particle-antiparticle factors averaged appropriately.

It is convenient to describe the kinematics using the Mandelstam variables s, t, u. Since $s = (p_1 + p_2)^2$ is Lorentz invariant, we define the Lorentz-invariant quantity $w(s)$,

$$w(s) \equiv \frac{1}{4} \int d\,LIPS |\mathcal{T}|^2 = E_1 E_2 \sigma v_{rel}. \tag{3.13}$$

Assuming that the initial-state particles has an energy distribution $f(E)$, $\langle \sigma v_{rel} \rangle$ can be written as

$$\langle \sigma v_{rel} \rangle = \frac{1}{n_0^2} \int dE_1 dE_2 f(E_1) f(E_2) \frac{w(s)}{E_1 E_2}, \tag{3.14}$$

where n_0 normalizes the initial-state particle distribution $n_0 = \int dE f(E)$.

The range of temperature we are particularly interested in is $x \sim 20$, where the statistics of particle is not important. Therefore, the energy distribution of particles in the thermal bath can be approximated as the Boltzmann one, $f(E) = \kappa (2\pi)^3 e^{-E/T}$, where κ is the number of degrees of freedom of spin and color.

Moreover, it is in general computationally inefficient to evaluate Eq. (3.14) directly as it involves multiple integrals. As we are mainly interested in the the cross section at $x \gtrsim 20$, it is more convenient to obtain analytical expressions of each term in the expansion of $\langle \sigma v_{rel} \rangle$ with respect to $1/x$. First, we write

$$\begin{aligned}
\langle \sigma v_{rel} \rangle &= \frac{\kappa^2}{(2\pi)^6 n_0^2} \int d^3p_1 d^3p_2 e^{-E_1/T} e^{-E_2/T} \frac{1}{E_1 E_2} w(s) && (3.15)\\
&= \frac{\kappa^2}{8\pi^4 n_0^2} \int dp_1 dp_2 \frac{p_1^2 p_2^2}{E_1 E_2} e^{-E_1/T} e^{-E_2/T} \int_{-1}^{1} d\cos\theta w(s) && (3.16)\\
&= \frac{\kappa^2}{8\pi^4 n_0^2} \int dE_1 dE_2 p_1 p_2 e^{-E_1/T} e^{-E_2/T} \int_{-1}^{1} d\cos\theta w(s), && (3.17)
\end{aligned}$$

where we have used $dp/dE = p/E$. Next, we perform changes of variables from E_i to y_i:

$$E_i = m(1 + \frac{y_i}{x}), \quad p_i = m\sqrt{\frac{2}{x}}\sqrt{y_i + \frac{1}{2}\frac{y_i^2}{x}}. \tag{3.18}$$

One needs to further express n_0 and s in terms of x and y_i (see [108] for details). Expanding around $s = 4m^2$, one gets

$$\langle \sigma v_{rel} \rangle = \frac{1}{m^2} \left[w - \frac{3}{2}(2w - w')\frac{1}{x} + ... \right]_{s=4m^2}, \tag{3.19}$$

where w, w' is to be evaluated at $s = 4m^2$. The first and second term is commonly called the s-wave and p-wave thermally averaged cross section (a and b terms) respectively in the literature when the thermally averaged cross section is expanded in the form $\langle \sigma v_{rel} \rangle = a + b\,T/m_X + \mathcal{O}\left((T/m_X)^2\right)$.

3.3 Coannihilation

Let us now consider a system of N particles which has a conserved multiplicative quantum number different from the SM particles, denoted as χ_i for $i = 1, ..., N$. This corresponds to the R-parity of the SUSY particles in SUSY. Each exotic particle decays into lighter exotic particles with the quantum number conserved. Then, the lightest particle is stable due to the quantum number conservation and can be the candidate of dark matter. While the coupled Boltzmann equations look complicated to solve, as will be shown below, since we are mainly interested in the lightest particle's relic abundance, the solution can be simplified dramatically.

There are various possible interactions within this system. Let us take SUSY as an example to elucidate these interactions. Often the lightest SUSY particle (LSP) is thought to be the lightest neutralino. For example, if the lightest neutralino is wino-like, it annihilates into the W bosons:

$$\chi_1^0 + \chi_1^0 \leftrightarrow W^+W^-. \tag{3.20}$$

If the temperature of the thermal bath is high enough, the LSP can scatter with an SM particle to create another SUSY particle accompanied by yet another SM particle:

$$\chi_1^0 + q \leftrightarrow \tilde{q} + g, \tag{3.21}$$

where $\tilde{q}$ refers to the squark. This process trivially leads to the "crossed" process where a pair of SUSY particles (of different species) annihilates into SM particles:

$$\chi_1^0 + \tilde{q} \leftrightarrow q + g. \tag{3.22}$$

Finally, in the Boltzmann equation, one should include the decay process:

$$\tilde{q} \leftrightarrow q + \chi_1^0. \tag{3.23}$$

The Boltzmann equation governing the number density of χ_i should then look like as follows:

$$\begin{aligned} \frac{dn_i}{dt} + 3Hn_i = & - \sum_{j,X} \langle \sigma_{ij} v \rangle (n_i n_j - n_i^{eq} n_j^{eq}) && (3.24) \\ & - \langle \sigma'_{ij} v \rangle (n_i n_X - n_j^{eq} n_{X'}^{eq}) && (3.25) \\ & - \Gamma_{ij} (n_i - \frac{n_j}{n_j^{eq}}), && (3.26) \end{aligned}$$

where the labels X, X' refer to SM particles. The cross sections and decay rates refer to the processes:

$$\sigma_{ij} = \sigma(\chi_i \chi_j \leftrightarrow XX'), \tag{3.27}$$

$$\sigma'_{ij} = \sigma(\chi_i X \leftrightarrow \chi_j X'), \tag{3.28}$$

$$\Gamma_{ij} = \Gamma(\chi_i \leftrightarrow \chi_j X). \tag{3.29}$$

Since heavier χ's eventually decay to the lightest χ_1, it is useful to define the total number density of χ's $n = \sum_{i=1}^{N} n_i$, and track the change of n with time in the Boltzmann equation. Using Eq. (3.26), the Boltzmann equation of n can be written as

$$\frac{dn_i}{dt} + 3Hn_i = \quad - \quad \sum_j \langle \sigma_{ij} v \rangle (n_i n_j - n_i^{eq} n_j^{eq}). \tag{3.30}$$

Let us note that for $i = j$, two particles are annihilated away,resulting in a factor of 2. However, the factor 2 is balanced by a factor 1/2 due to the fact that the annihilating particles are identical. Therefore, the equation shown above is correct even for $i = j$. Let us also note that the total relic number density is independent of the conversion term proportional to σ'_{ij}, and decay term Γ_{ij}, since at late times, all exotic particles eventually decay into the lightest state.

Eq. (3.30) can be further simplified by getting rid of the unknown n_i's. This is done by using the fact that the scattering process σ'_{ij} occurs at a much larger rate than the annihilation process. This is because the exotic particles are non-relativistic around the freeze-out temperature, and its number density is Boltzmann suppressed. On the other hand, SM particles are light and the number density is $n_X \propto T^3$. More concretely,

$$\frac{n_i n_X \langle \sigma'_{ij} \rangle}{n_i n_j \langle \sigma_{ij} \rangle} \sim \frac{T^3}{(m_j T^3)^{3/2} e^{-m_j/T}} \sim \left(\frac{T}{m_j} \right)^{3/2} e^{m_j/T}, \tag{3.31}$$

where we have assumed that the scattering and annihilation cross sections are of the same order (which is usually, because they are related by crossing). For $m_j \sim m_1$ and $T \sim m_1/25$, the scattering rate is around 10^9 larger than the annihilation rate. From Eq. (3.26), it can be seen that such a large rate keep the ratio n_i/n_j in equilibrium:

$$\frac{n_i}{n_j} = \frac{n_i^{eq}}{n_j^{eq}}. \tag{3.32}$$

Or, more conveniently, the expression can be written as

$$\frac{n_i}{n} = \frac{n_i^{eq}}{n^{eq}}. \tag{3.33}$$

With this expression, Eq. (3.30) can be written as

$$\frac{dn}{dt} + 3Hn = -\langle \sigma_{eff} v \rangle (n^2 - n_{eq}^2), \tag{3.34}$$

where

$$\langle \sigma_{eff} v \rangle = \sum_{i,j} \langle \sigma_{ij} v \rangle \frac{n_i^{eq}}{n_{eq}} \frac{n_j^{eq}}{n_{eq}}. \tag{3.35}$$

The Boltzmann equation then looks just the same as the case where there is only a single exotic particle annihilating by itself, Eq. (3.2). The effect of heavier exotic particles on the relic abundance of the lightest particle is called coannihilation [109].

To elucidate this effect, consider a system composed of two species of exotic particles. The effective annihilation cross section is then given by

$$\langle \sigma_{eff} v \rangle = \langle \sigma_{11} v \rangle \frac{n_1^{eq2}}{n_{eq}^2} + \langle \sigma_{22} v \rangle \frac{n_2^{eq2}}{n_{eq}^2} + 2\langle \sigma_{12} v \rangle \frac{n_1^{eq} n_2^{eq}}{n_{eq}^2}. \tag{3.36}$$

At the limit $m_2 \gg m_1$, it becomes

$$\langle \sigma_{eff} v \rangle = \langle \sigma_{11} v \rangle, \tag{3.37}$$

the usual definition of annihilation cross section. On the other hand, at the limit $m_2 = m_1$,

$$\langle \sigma_{eff} v \rangle = \frac{1}{(g_1 + g_2)^2} \left(g_1^2 \langle \sigma_{11} v \rangle + g_2^2 \langle \sigma_{22} v \rangle + 2 g_1 g_2 \langle \sigma_{12} v \rangle \right). \tag{3.38}$$

It can be observed that, even if χ_1 has zero self annihilation cross section, its number density can be reduced with the help of the partner χ_2's self annihilation, provided that their masses are almost degenerate. Physically, the number density is reduced as χ_1 is continuously converted into χ_2 in the thermal bath, where χ_2 is subsequently annihilated away by self interaction. The efficiency of this convert-and-annihilate effect is controlled by the Boltzmann suppression coming from the mass splitting:

$$\frac{n_2^{eq}}{n_{eq}} \sim e^{\frac{m_1 - m_2}{T}}. \tag{3.39}$$

Therefore, the annihilation cross section of the partner particle can, when the mass splitting is small, determine the relic abundance of dark matter dominantly. In particular, the coannihilation effects of a colored partner particle can be very important due to its strong interactions. This will be the main topic in the following chapters of this study.

Moreover, it should be noted that colored particles can form a bound state in the early universe. The long-ranged nature of QCD interaction makes bound state formation of colored particles possible. The formation of a QCD bound state η_X occurs via the process $X_1 X_2 \to \eta_X g$, with the final-state gluon carrying the binding energy $E_B \simeq m_\eta - m_1 - m_2$. η_X can then decay to gluons or quarks via QCD annihilation of the constituent X's. The formation of bound state and its subsequent decay to SM particles help remove X from the thermal bath. As will be shown in the following, this type of process increases significantly the effective annihilation cross section of X or DM. This will also be dealt with in the following chapters.

Chapter 4

Coannihilation of colored particles

In cosmological scenarios of physics beyond the SM, the early universe may have been inhabited by exotic particles charged under QCD. Due to their strong interactions with SM particles, they were initially in thermal equilibrium and later froze out such that their number density over entropy density (Y_X for particle X) remains constant until present.

While the relic abundance of a stable colored particle is stringently constrained by null results from searches for exotic isotopes or nuclei [1], the bounds are considerably relaxed if the colored particle is metastable, i.e. it froze out and decayed to neutral particles at a timescale much shorter than the lifetime of the universe. This can happen in, e.g., R-parity conserved Minimal Supersymmetric Standard Model (MSSM) where the next-to-the lightest supersymmetric particle (NLSP) is colored, and the lightest LSP or DM is extremely weakly interacting (superWIMP), such as gravitino or axino. Typically, observational and experimental bounds are applicable only to metastable colored particles with lifetime $\gtrsim 0.1$s. Specifically, one can derive significant constraints from processes of the big-bang nucleosynthesis (BBN) [30]. Moreover, the decay of the frozen out colored particles into superWIMPs can contribute non-thermally to the relic density of DM.

Even if the colored particle has not-so-weak interaction with DM, the colored particle can play a role in determining the relic abundance of DM, especially when the mass of the colored particle is almost degenerate with DM. Coannihilations among themselves can significantly reduce the relic abundance of DM [109].

[1] See [110] for a review. The bounds using carbon on Y_X/Y_B (B denoting baryon) range from 10^{-20} to 10^{-16} for $m_X \simeq 0.1 - 10$ TeV [111].

4.1 Motivations

Squarks and gluino are the colored SUSY particles. In the so-called split SUSY scenarios, where the scalar SUSY partners are heavy and fermion partners are light, gluino coannihilations are possible [112–122]. In such a scenario, the LSP would be a neutralino (gaugino or Higgsino, or the mixture of them). As gluino decays via an intermediate squark to the neutralino, its decay rate is suppressed with respect to two-body decay. If the timescale of bound state formation is shorter than gluino lifetime, the formation of gluinonium is possible.

The scalar SUSY partner of the top quark, stop is, in variants of MSSM, for example the CMSSM, the coannihilating partner of the lightest neutralino [123–132]. Often, stop receives the largest radiative corrections and its mass (at hight scale) can be driven down to mass range of the LSP (at low scale), initiating stop coannihilation. If the mass splitting between stop and the LSP is smaller than the mass of the top quark, its lifetime is delayed. Again, stoponium formation is possible if the rate of bound state formation is fast enough.

The extension of the SM with a vector-like quark is a fairly popular idea due to its simplicity [2]. It can couple to a DM-to be scalar field and a SM quark field via the Yukawa coupling, initiating coannihilation if the mass splitting is small. The decay of the vector-like quark into DM is controlled by the Yukawa coupling, and if it is small, bound state formation is possible. The same goes to the possibility of having a massive scalar gluon in the SM extension.

The colored particle we consider in this thesis is either a scalar (S) or fermion (F). It can also either be a color triplet (**3**) or octet (**8**). These four cases are abbreviated in the following as S3, S8, F3 and F8.

4.2 Annihilation of colored particles

We now proceed to present the calculation of the QCD annihilation of colored particles into quarks and gluons. The kinematic variables are written in terms of s, t, u. For colored fermions, there are three diagrams contributing to the annihilation into two gluons: s-channel gluon exchange. t an u-channel X exchange diagrams. For colored scalars, there is additional a contact interaction diagram. For annihilation into quark-antiquark, there is only the s-channel gluon exchange diagram. The procedure of extracting the s and p-wave annihilation cross section is described in Section 3.2.

[2] Such a particle can also be found in models of Universal Extra Dimensions in the form of Kaluza-Klein (KK) quark [133–138].

Color rep. (fermion)	c_{ini}	C_{ss}	C_{tt}	C_{st}	C_{tu}	D_{ss}
3	1/9	12	16/3	6	-2/3	8
8	1/64	72	72	36	36	48

Table 4.1: color factors for fermion annihilation.

Colored fermion annihilation to gluons

A factor c_{ini} is used to average over initial colors. $|\mathcal{T}|^2$ takes the form

$$|\mathcal{T}|^2 = c_{ini}(\mathcal{T}_s\times\mathcal{T}_s + \mathcal{T}_t\times\mathcal{T}_t + \mathcal{T}_u\times\mathcal{T}_u + \mathcal{T}_s\times\mathcal{T}_t + \mathcal{T}_s\times\mathcal{T}_u + \mathcal{T}_t\times\mathcal{T}_u)\,.$$

$$\begin{aligned}
\mathcal{T}_s\times\mathcal{T}_s &= C_{ss}\frac{16\pi^2\alpha_s^2}{s^2}\left[s^2-(t-u)^2\right]\,,\\
\mathcal{T}_t\times\mathcal{T}_t &= -C_{tt}\frac{32\pi^2\alpha_s^2}{s^2\left(m_X^2-t\right)^2}\Big\{m_X^2\left[s^2(t+3u)+2s(t^2+2u^2)+2(t+u)^3\right]\\
&\qquad + m_X^4\left[s^2-2s(t+2u)-6(t+u)^2\right]+2m_X^6\left[s+4(t+u)\right]\\
&\qquad - 4m_X^8 - tu\left[s^2+2su+2(t^2+u^2)\right]\Big\}\,,\\
\mathcal{T}_s\times\mathcal{T}_t &= -C_{st}\frac{16\pi^2\alpha_s^2}{s^2\left(m_X^2-t\right)}\left[s(t-u)\left(4m_X^2-t+u\right)+s^3+s^2(u-t)+(t-u)^3\right]\,,\\
\mathcal{T}_t\times\mathcal{T}_u &= -C_{tu}\frac{64\pi^2\alpha_s^2}{s^2\left(m_X^2-t\right)\left(m_X^2-u\right)}\left(m_X^4-tu\right)\left[-4(t+u)m_X^2+8m_X^4+(t-u)^2\right]\,,
\end{aligned}$$

and $\mathcal{T}_s\times\mathcal{T}_u$ and $\mathcal{T}_u\times\mathcal{T}_u$ are related to $\mathcal{T}_s\times\mathcal{T}_t$ and $\mathcal{T}_t\times\mathcal{T}_t$, respectively, by exchanging $t\leftrightarrow u$ in the corresponding expressions.

Colored fermion annihilation to quarks

$$|\mathcal{T}|^2 = c_{ini}(\mathcal{T}_s\times\mathcal{T}_s)\,.$$

$$\mathcal{T}_s\times\mathcal{T}_s = D_{ss}\frac{48\pi^2\alpha_s^2}{s^2}\left[m_X^2(s-t-u)+2m_X^4+t^2+u^2\right]\,.$$

Colored scalar annihilation to gluons

$$|\mathcal{T}|^2 = c_{ini}(\mathcal{T}_s\times\mathcal{T}_s+\mathcal{T}_t\times\mathcal{T}_t+\mathcal{T}_u\times\mathcal{T}_u+\mathcal{T}_c\times\mathcal{T}_c+\mathcal{T}_s\times\mathcal{T}_t+\mathcal{T}_s\times\mathcal{T}_u+\mathcal{T}_t\times\mathcal{T}_u+\mathcal{T}_t\times\mathcal{T}_c+\mathcal{T}_u\times\mathcal{T}_c)\,.$$

Color rep. (scalar)	c_{ini}	C_{ss}	C_{tt}	C_{cc}	C_{st}	C_{tu}	C_{tc}	D_{ss}
3	1/9	12	16/3	28/3	6	-2/3	14/3	8
8	1/64	72	72	216	36	36	108	48

Table 4.2: color factors for scalar annihilation.

	S3	F3	S8	F8
a for gg	14/27	7/27	27/16	27/32
b for gg	$-61/27$	1/6	-261/32	9/64
a for $q\bar{q}$	0	4/3	0	9/8
b for $q\bar{q}$	4/3	$-14/3$	9/8	$-63/16$

Table 4.3: The coefficients a and b in $\langle\sigma v_{rel}\rangle$ for massive colored particle pair annihilation to gg or $q\bar{q}$, up to the common factor $\pi\alpha_s^2/m_X^2$, for the S3, F3, S8 and F8 cases.

$$
\begin{aligned}
\mathcal{T}_s\times\mathcal{T}_s &= C_{ss}\frac{32\pi^2\alpha_s^2}{s^2}(t-u)^2\,,\\
\mathcal{T}_t\times\mathcal{T}_t &= -C_{tt}\frac{256\pi^2\alpha_s^2}{s^2\left(m_X^2-t\right)^2}\left(-m_X^4+t\,u\right)^2\,,\\
\mathcal{T}_c\times\mathcal{T}_c &= C_{cc}\,32\pi^2\alpha_s^2\,,\\
\mathcal{T}_s\times\mathcal{T}_t &= -C_{st}\frac{64\pi^2\alpha_s^2}{s^2\left(m_X^2-t\right)}(t-u)\left[s\left(s-2m_X^2\right)-\left(m_X^2-t\right)^2-\left(m_X^2-u\right)^2\right]\,,\\
\mathcal{T}_t\times\mathcal{T}_u &= C_{tu}\frac{64\pi^2\alpha_s^2}{s^2\left(m_X^2-t\right)\left(m_X^2-u\right)}\left[2m_X^2(s-t-u)+2m_X^4-s^2+t^2+u^2\right]^2\,,\\
\mathcal{T}_t\times\mathcal{T}_c &= C_{tc}\frac{64\pi^2\alpha_s^2}{s\left(m_X^2-t\right)}\left[2m_X^2(s-t-u)+2m_X^4-s^2+t^2+u^2\right]\,.
\end{aligned}
$$

Colored scalar annihilation to quarks

$$|\mathcal{T}|^2 = c_{ini}(\mathcal{T}_s\times\mathcal{T}_s)\,.$$

$$\mathcal{T}_s\times\mathcal{T}_s = D_{ss}\frac{48\pi^2\alpha_s^2}{s^2}\left[s(s-4m_X^2)-(u-t)^2\right]\,.$$

Up to the common factor $\pi\alpha_s^2/m_X^2$, the a and b terms in $\langle\sigma v_{rel}\rangle$ we found are listed in Table 4.3. The results for the $q\bar{q}$ channel are for all 6 types of SM quarks, and we have dropped quark mass dependent terms, as we are considering massive colored particles much heavier than the SM quarks.

4.3 Sommerfeld corrections

In addition to the annihilation of colored particles at the tree level as discussed above, there is another effect: at low velocities, the initial state of the annihilating particles receives non-perturbative corrections due to the exchange of multiple t-channel ladder-type massless mediators, namely Sommerfeld correction. See [139–141] and [142–145] for its effects on DM annihilation and coannihilation respectively.

The Sommerfeld correction is understood as the ratio of the wave-function squared with and without the influence of potential at the interaction point ($x = 0$),

$$S = \frac{|\psi_k(0)|^2}{|\psi_k^{(0)}(0)|^2} = |\psi_k(0)|^2, \tag{4.1}$$

where we have normalized $\psi_k^{(0)}(0)$ to 1, and k is the momentum of the particle. Under the influence of a centrally symmetric potential, the wave-function can be written as

$$\psi_k = \sum_{l=0}^{\infty} \frac{i^L e^{i\delta_L}(2L+1)}{k} P_l(\cos\theta) R_{kL}(r), \tag{4.2}$$

where $P_L(\cos\theta)$ is the the associated Legendre function with L the angular momentum quantum number, and $R_{kL}(r)$ is the radial function.

We then need to solve the Schroedinger equation of the radial function. Under the influence of an Abelian-like massless mediator with Coulomb potential $V = \alpha/r$, the radial part of the Schroedinger equation is

$$\frac{1}{r}\frac{d}{dr}\left(r^2 \frac{dR(r)}{dr}\right) - \frac{L(L+1)}{r^2} R(r) + 2m(E - \frac{\alpha}{r})R(r) = 0, \tag{4.3}$$

with m and E the mass and energy of the particle.

It is convenient to make a change of variables:

$$\rho = kr \tag{4.4}$$
$$y = \frac{\alpha}{\beta} \tag{4.5}$$
$$\chi(r) = rR(r) \tag{4.6}$$

with β the particle velocity. Then, the equation looks like

$$\frac{d^2\chi(\rho)}{d\rho^2} + \left(1 - \frac{2y}{\rho} - \frac{L(L+1)}{\rho}\right)\chi(\rho) = 0. \tag{4.7}$$

The solution is

$$\chi(\rho) = \sqrt{\frac{2\pi y}{e^{2\pi y} - 1}} \frac{(2\rho)^2 \rho}{(2L+1)!} e^{i\rho} M(L+1+iy, 2L+2, -2iy) \prod_{s=1}^{l} \sqrt{s^2 + y^2}, \tag{4.8}$$

where

$$M(\alpha,\gamma,z) \equiv 1 + \frac{\alpha}{\gamma}\frac{z}{1!} + \frac{\alpha(\alpha+1)}{\gamma(\gamma+1)}\frac{z^2}{2!} + ... \tag{4.9}$$

is the confluent hypergeometric function. We are mainly interested in the s-wave contribution ($L = 0$). Moreover, the case of interest involves the QCD potential between two particles of the same mass, where in the center-of-mass frame, we substitute $m \to m/2$ and $\beta \to \beta/2 = v_{rel}$. Taking account into these, the Sommerfeld factor is

$$\begin{aligned} S &= |\psi_k(0)|^2 && (4.10)\\ &= |\frac{e^{i\delta_0}(2L+1)}{k} R_{k0}(r)|^2 && (4.11)\\ &= \frac{\pi y}{e^{\pi y}-1} && (4.12) \end{aligned}$$

An attractive potential ($\alpha > 0$) results in an enhancement ($S > 1$), while a repulsive potential ($\alpha < 0$) results in a suppression ($S < 1$). The Sommerfeld corrected s-wave annihilation cross section can be written as

$$\sigma v_{rel} = aS(\alpha/v_{rel}), \tag{4.13}$$

In Eq. (4.13), the perturbative s-wave cross section, a, does not depend on temperature. Therefore, the thermally-averaged Sommerfeld corrected s-wave cross section is $a\langle S(\alpha/v_{rel})\rangle$, where

$$\langle S(\alpha/v_{rel})\rangle = \int_0^\infty S(\alpha/v_{rel}) f(v_{rel}) dv_{rel}, \tag{4.14}$$

where $f(v_{rel})$ is the Maxwell-Boltzmann distribution function of v_{rel}, given as

$$f(v_{rel}) = \left(\frac{\mu}{2\pi T}\right)^{3/2} 4\pi v_{rel}^2 \, e^{-\frac{\mu v_{rel}^2}{2T}}. \tag{4.15}$$

For the massive colored particles of our interest, we expect that the dominate annihilation channels are $S3\overline{S3}$, $F3\overline{F3}$, $S8S8$ and $F8F8$ annihilation into a pair of gluon, gg, and into quark-antiquark pairs, $q\bar{q}$. We consider the Sommerfeld corrected s-wave cross sections and the tree-level p-wave cross sections in our calculation. To consider the Sommerfeld effect, we need to decompose an s-wave cross section into partial cross sections contributed from each two-body states in different color representations, as given in Eqs. (5.4) and (5.5), because different representations correspond to different Coulomb-like potentials. We follow the decompositions given in [145]. The thermally-averaged

Sommerfeld factors are

$$\begin{aligned}
\frac{\langle\sigma v_{rel}(S3\overline{S3} \text{ or } F3\overline{F3} \to gg)\rangle_{s\text{-wave, Sommerfeld}}}{\langle\sigma v_{rel}(S3\overline{S3} \text{ or } F3\overline{F3} \to gg)\rangle_{s\text{-wave, pertubative}}} &= \frac{2}{7}\langle S(\frac{4\alpha_s/3}{v_{rel}})\rangle + \frac{5}{7}\langle S(\frac{-\alpha_s/6}{v_{rel}})\rangle\,, \\
\frac{\langle\sigma v_{rel}(F3\overline{F3} \to q\overline{q})\rangle_{s\text{-wave, Sommerfeld}}}{\langle\sigma v_{rel}(F3\overline{F3} \to q\overline{q})\rangle_{s\text{-wave, pertubative}}} &= \langle S(\frac{-\alpha_s/6}{v_{rel}})\rangle\,, \\
\frac{\langle\sigma v_{rel}(S8S8 \text{ or } F8F8 \to gg)\rangle_{s\text{-wave, Sommerfeld}}}{\langle\sigma v_{rel}(S8S8 \text{ or } F8F8 \to gg)\rangle_{s\text{-wave, pertubative}}} &= \frac{1}{6}\langle S(\frac{3\alpha_s}{v_{rel}})\rangle + \frac{1}{3}\langle S(\frac{3\alpha_s/2}{v_{rel}})\rangle + \frac{1}{2}\langle S(\frac{-\alpha_s}{v_{rel}})\rangle\,, \\
\frac{\langle\sigma v_{rel}(F8F8 \to q\overline{q})\rangle_{s\text{-wave, Sommerfeld}}}{\langle\sigma v_{rel}(F8F8 \to q\overline{q})\rangle_{s\text{-wave, pertubative}}} &= \langle S(\frac{3\alpha_s/2}{v_{rel}})\rangle\,. \qquad (4.16)
\end{aligned}$$

The s-wave cross sections vanish for $S3\overline{S3} \to q\overline{q}$ and $S8S8 \to q\overline{q}$.

Chapter 5

Colored bound states in the early universe

The main purpose of the following chapters is to study the effects of exotic massive colored particles on DM relic abundance, assuming that they share the same discrete symmetry stabilizing DM (e.g., R-parity in supersymmetric models and KK-parity in UED models). In this chapter, we study properties of QCD bound state and how they play a role in the early-universe cosmology. These results will be used in the next chapter to calculate the DM relic abundance in scenarios where the colored particle coannihilates with the WIMP. We also discuss implications of a metastable colored particle on BBN and the DM relic abundance in the superWIMP scenario.

5.1 Bound state formalism

In this section, we discuss properties and dynamics of formation and dissociation of QCD bound state, $X_1 X_2 \leftrightarrow \eta g$. Studies on DM bound state formation due to some new binding force can be found in the literature, see [146–149]. Gluino (colored octet) bound-state effects on neutralino DM coaanihilation have been investigated in [121].

We are mainly concerned with masses of colored particles satisfying $m_1, m_2 \gg \Lambda_{\rm QCD}$. At this limit, the dynamics can be described by the exchange of single gluon where the potential is Coulomb-like, and if the potential is attractive, a bound state can be formed. The bound state is characterized by the color decomposition of its constituent particle. As an example, a pair of SM top and anti-top decomposes as follows:

$$t\bar{t}: \quad \mathbf{3} \otimes \overline{\mathbf{3}} = \mathbf{1} \oplus \mathbf{8}, \tag{5.1}$$

and the two-particle state is characterized by the **1** and **8** color representations. The

Coulomb-like potential due to gluon exchange has the form:

$$V(r) = -\frac{\zeta}{r}\,, \tag{5.2}$$

in which ζ is determined by the quadratic Casimir coefficients of the color representations of the individual colored particles, X_1 and X_2 (C_{X_1} and C_{X_2}, respectively), as well as of the one by taking X_1 and X_2 together in a specific color state ($C_{X_1X_2}$):

$$\zeta = \frac{1}{2}\left(C_{X_1} + C_{X_2} - C_{X_1X_2}\right)\alpha_s\,, \tag{5.3}$$

where $\alpha_s > 0$ is the QCD coupling strength. A positive, negative or zero value of ζ gives an attractive, repulsive or zero potential, respectively.

The colored particles we consider in this paper include a complex scalar and a Dirac fermion in the color SU(3) fundamental representation, a real scalar and a Majorana fermion in the adjoint representation. The X_1X_2 combinations are $S3\overline{S3}$, $F3\overline{F3}$, $S8S8$ and $F8F8$, abbreviated in the following as S3, F3, S8 and F8, respectively, and hence $m_{X_1} = m_{X_2} \equiv m_X$. As mentioned previously, there are motivations to consider such particles in BSM. Examples of S3 and F8 are a squark-antisquark pair and a gluino-gluino pair, respectively, in the MSSM. A KK quark-antiquark pair in models of UED is a realization of F3. One can also build models for the S8 case [150, 151]. As shown before, the product of a color triplet and an anti-triplet is decomposed as

$$\mathbf{3} \otimes \overline{\mathbf{3}} = \mathbf{1} \oplus \mathbf{8}, \tag{5.4}$$

and the product of two color octets is decomposed as

$$\mathbf{8} \otimes \mathbf{8} = \mathbf{1}_S \oplus \mathbf{8}_A \oplus \mathbf{8}_S \oplus \mathbf{10}_A \oplus \overline{\mathbf{10}}_A \oplus \mathbf{27}_S, \tag{5.5}$$

where the subscripts S and A indicate symmetric and anti-symmetric color states, respectively. Therefore, the relevant quadratic Casimir coefficients of the color representations for our calculations are $C_{\mathbf{1}} = 0$, $C_{\mathbf{3}} = 4/3$, $C_{\mathbf{8}} = 3$, $C_{\mathbf{10}} = 6$ and $C_{\mathbf{27}} = 8$. [1]

In principle, a bound state can form as long as the potential for it is attractive. In this paper, we focus on the color-singlet bound state, since it is expected to be the deepest bound (i.e., the ground state) and the most copiously produced one, in analogy

[1] We note that at a temperature T of the Universe, the screening effect from the quarks and gluons in the thermal plasma induces a thermal mass $m_{th} \sim \sqrt{\alpha_s}T$ to the gluon, modifying the QCD Coulomb potential to a Yukawa one. However, as emphasized in [152], the Coulomb potential is a good approximation as long as the momentum transfer between the two incoming particles, $\sim m_X\sqrt{\frac{T}{m_X}}$, is larger than m_{th}. We can see that this condition is well satisfied at the usual freeze-out temperature $T \sim m_X/20$, and further better satisfied for the bound-state effect calculation since the effect of which is important at even lower temperature $T \sim \alpha_s^2 m_X$, as will be shown in the next section.

to atomic physics [2]. Therefore, the coefficient, ζ, in Eq. (5.2) for the bound state in the S3 and F3 cases is $1/2\times(4/3+4/3-0)\alpha_s = (4/3)\alpha_s$, and is $1/2\times(3+3-0)\alpha_s = 3\alpha_s$ for the S8 and F8 cases. In all the four cases, we consider that the color-singlet bound state has total orbital angular momentum $L = 0$ and spin $S = 0$ [3]. The normalized spatial wave function of such a bound state is

$$\phi_\eta(r) = (\pi a^3)^{-1/2} e^{-r/a}, \tag{5.6}$$

where a is the Bohr radius,

$$a = (\zeta\mu)^{-1}, \tag{5.7}$$

where $\mu \equiv m_{X_1} m_{X_2}/(m_{X_1} + m_{X_2}) = m_X/2$ is the reduced mass. The binding energy of the bound state is

$$E_B = \frac{\zeta^2\mu}{2}. \tag{5.8}$$

We show all possible combinations of bounds states as well as the strengths of the potential among MSSM colored particles (stop $\tilde{t}$ and gluino $\tilde{g}$) in Table 5.1 and 5.2.

5.2 Dissociation and formation of bound states in the early universe

We first give a general description of the dissociation and formation processes of bound states without specifying the color representation of the particles. We focus only on the dynamics of the ground state of color singlet bound state (with angular momentum

[2] In [149], the formation of bound states at excited energy levels is discussed for bound-state effects in the late Universe, and it is found that the total bound-state formation cross section is dominated by levels with principle quantum numbers $n < \zeta/v_{rel}$, where v_{rel} is the relative velocity of the incoming particles. Compared to the ground state, the contribution from the excited states enhances the total bound-state formation cross section by a logarithmic factor $\sim \log(\zeta/v_{rel})$, which is significant for $v_{rel} \sim 10^{-3}$ in the galactic halo. However, in the early Universe at temperatures relevant for the dark matter relic abundance calculation, v_{rel} is of order 10^{-1}, so that $\zeta/v_{rel} \sim 1$. Moreover, compared to the ground state, the excited states are easier to be dissociated by gluons in the thermal bath, while the dissociation is not a concern for bound states in the late Universe. Therefore, the contribution from the excited states is not significant for the relic abundance calculation. Nevertheless, in the next section we will also show results with a factor of 2 enhancement of the bound-state effect from the considerations of the excited states contribution as well as other uncertainties in our calculations.

[3] The total wave function of the bound state is a product of the spatial, spin and color parts of the wave functions. For the S8 (F8) case, because of the nature of identical particles, the total wave is symmetric (anti-symmetric). $L = 0$ gives symmetric (symmetric) spatial wave function, and $S = 0$ gives symmetric (anti-symmetric) spin wave function. Together with the symmetric color wave function of the color-$\mathbf{1}_S$ state, indeed the requirement of the total wave function is satisfied.

MSSM	attractive	repulsive
$\tilde{g}\tilde{g}$	$\mathbf{1}, \mathbf{8_S}, \mathbf{8_A}$	$\mathbf{10}, \overline{\mathbf{10}}, \mathbf{27}$
$\tilde{t}\tilde{t}^*$	$\mathbf{1}$	$\mathbf{8}$
$\tilde{t}\tilde{t}$	$\overline{\mathbf{3}}$	$\mathbf{6}$
$\tilde{t}\tilde{g}$	$\mathbf{3}, \overline{\mathbf{6}}$	$\mathbf{15}$

Table 5.1: Color representations of bound states formed by a pair of MSSM particles (stop $\tilde{t}$ or gluino $\tilde{g}$).

MSSM	$SU(3)$	C
$(\tilde{g}\tilde{g})$	$\mathbf{1}$	3
	$\mathbf{8}$	3/2
$(\tilde{t}\tilde{t}^*)$	$\mathbf{1}$	4/3
$(\tilde{t}\tilde{t}), (\tilde{t}^*\tilde{t}^*)$	$\overline{\mathbf{3}}, \mathbf{3}$	2/3
$(\tilde{t}\tilde{g}), (\tilde{t}^*\tilde{g})$	$\mathbf{3}, \overline{\mathbf{3}}$	3/2
	$\overline{\mathbf{6}}, \mathbf{6}$	1/2

Table 5.2: Bound states in MSSM, their color representations and the strength of their potential (5.2). Due to Bose symmetry, the ground states of $\tilde{t}\tilde{t}$ and $\tilde{t}^*\tilde{t}^*$ have angular momentum $L = 1$. Moreover, the ground state of $\tilde{g}\tilde{g}$ ($\tilde{t}\tilde{g}$) belongs to the $\mathbf{1}(\mathbf{3})$ representation due to the larger value of C.

$L = 0$ and spin angular momentum $S = 0$), which is expected to be most copiously produced in the early universe.

First of all, due to color charge conservation, the emission (absorption) of a gluon during bound-state formation (dissociation) makes the color representation of the bound state η not necessarily be the same as the free pair X_1X_2. Therefore, the coefficient in the Coulomb potential for the free pair, denoted as ζ', is not necessarily equal to the one for the bound state. In particular, ζ' can be negative, so that the potential is repulsive for the free pair. As will be shown, at high temperature in the early Universe, the massive colored particles can have enough kinetic energy to overcome a repulsive potential to form a bound state.

We follow [121] to calculate the bound-state formation and dissociation cross sections, where the method is adapted from the calculations of the photoelectric effect for an atom [153]. The essence of of the calculation is to evaluate the transition matrix element between the bound state and the free pair state:

$$\mathcal{M}_{fi} = \int \phi_f^* (-i \frac{\vec{\nabla} \cdot \vec{\epsilon}^c}{\mu}) e^{i\vec{k}\cdot\vec{r}} \phi_i d^3\vec{r}, \tag{5.9}$$

where ϕ_f is the wave function of the free pair and $\phi_i \equiv \phi_\eta(r)$. The gluon has a momentum

$\vec{k}$ and a polarization $\vec{\epsilon}^{c}$, where "c" is the color index.

For the free pair, the normalized spatial part of the wave function is (see Section 136 of [154])

$$\phi_f = \frac{1}{2|\vec{p}|}\sum_{L=0}^{\infty} i^L(2L+1)e^{-i\delta_L}R_{pL}(r)P_L(\frac{\vec{p}\cdot\vec{r}}{|\vec{p}|r}), \tag{5.10}$$

where $|\vec{p}|$ is the relative momentum of the free pair, expressed in terms of the reduced mass and their relative velocity as $|\vec{p}| = \mu v_{rel}$. $P_L(\frac{\vec{p}\cdot\vec{r}}{|\vec{p}|r})$ is the Legendre polynomial and δ_L (a real number) is the phase shift. Note that the form of the radial function $R_{pL}(r)$ for an attractive potential between the free pair is different from the one for a repulsive potential (see Section 36 of [154] for details). Consider the spatial part of the wave functions only, the differential dissociation cross section is given as

$$d\sigma^0_{dis} = \alpha_s\frac{\mu|\vec{p}|}{2\pi\omega}|\mathcal{M}_{fi}|^2 d\Omega_{\vec{p}}, \tag{5.11}$$

where $\omega \equiv |\vec{k}|$ is the energy of the gluon. The explicit α_s factor in the above equation comes from the coupling between the emitted gluon and the massive colored particle. In the Lagrangian of the quantum field theory, this coupling is from the covariant derivative of the kinetic term of the massive colored particle, and it takes the form of $ig_s\mathbf{T}_c$, where $g_s = \sqrt{4\pi\alpha_s}$ is the strong coupling, and $\mathbf{T}_c$ are the generator matrices for the color representation in which the massive colored particle lies. We will specify $\mathbf{T}_c$ in the next subsection when we consider the color part of the wave functions for the four cases of our interest.

We use the dipole approximation, i.e. $e^{i\vec{k}\cdot\vec{r}} \approx 1$ to calculate the transition matrix element Eq. (5.9). For the four cases of our interest (S3, F3, S8, F8), we have checked that the dipole approximation is always justified, i.e. $\omega a < 1$ (as the gluon carries a momentum $|\vec{k}| = \omega$). Also, the kinetic energy of the bound state is negligible compared to the gluon energy, so that $\omega \approx E_B + \frac{1}{2}\mu v^2_{rel}$. This means that only the $L = 1$ term in ϕ_f has a non-zero contribution due to selection rule. Also, considering that it is the absolute square of the transition matrix element that appears in Eq. (5.11), we can drop the phase factors and rewrite ϕ_f as

$$\phi_f = \frac{3}{2|\vec{p}|}R_{p1}(r)P_1(\frac{\vec{p}\cdot\vec{r}}{|\vec{p}|r})\,. \tag{5.12}$$

Defining the dimensionless quantities:

$$\nu \equiv |\zeta'|/v_{rel}, \tag{5.13}$$

and

$$\kappa \equiv \zeta/|\zeta'|, \tag{5.14}$$

we can write down the integrated dissociation cross section, averaged over the incoming gluon spin polarizations. The result depends on whether the free pair feels an attractive (denoted by the subscript "a") or a repulsive (denoted by the subscript "r") Coulomb potential:

$$\sigma^0_{dis,a} = \frac{2^9\pi^2}{3}\alpha_s a^2 \left(\frac{E_B}{\omega}\right)^4 \frac{1+\nu^2}{1+(\kappa\nu)^2}\frac{e^{-4\nu\,\mathrm{arccot}(\kappa\nu)}}{1-e^{-2\pi\nu}}\kappa^{-1}\,, \tag{5.15}$$

$$\sigma^0_{dis,r} = \frac{2^9\pi^2}{3}\alpha_s a^2 \left(\frac{E_B}{\omega}\right)^4 \frac{1+\nu^2}{1+(\kappa\nu)^2}\frac{e^{4\nu\,\mathrm{arccot}(\kappa\nu)-2\pi\nu}}{1-e^{-2\pi\nu}}\kappa^{-1}\,. \tag{5.16}$$

In the case that the free pair feels no potential (denoted by the subscript "$free$", and see Section 33 of [154] for the radial function), we find

$$\sigma^0_{dis,free} = \frac{2^9\pi^2}{3}\alpha_s a^2 \left(\frac{E_B}{\omega}\right)^4 \frac{(a\mu v_{rel})^3}{2\pi\left[1+(a\mu v_{rel})^2\right]}\,. \tag{5.17}$$

One can check that in the $\zeta' \to 0$ limit, Eq. (5.15) and Eq. (5.16) both become Eq. (5.17).

The superscript "0" in the above three equations indicates that we have considered the spatial part of the wave function only, while the full wave function is a product of spatial, color and spin wave functions. Also, if the particles are identical, one needs to symmetrize or anti-symmetrize the wave functions. The full dissociation cross section, σ_{dis}, after taking into account color, spin and the symmetry factors, is related to the bound-state formation cross section, σ_{bsf}, via the Milne relation:

$$\sigma_{bsf} = \frac{g_\eta g_g \omega^2}{g_{X_1} g_{X_2} \left(\mu v_{rel}\right)^2}\sigma_{dis}, \tag{5.18}$$

where $g_{g,X_1,X_2,\eta}$ are the degrees of freedom of gluon, X_1, X_2 and η, respectively. Note that if X_1 and X_2 are identical, the left-hand side of Eq. (5.18) has to be multiplied by $1/2$ to avoid double counting the number of bound-state formation reactions.

Bound state can be destroyed not only by the dissociation process, but also by decays. Moreover, the decays can happen in two ways: the constituent particles inside the bound state can annihilate between themselves (annihilation decay) or an individual constituent particle can decay by itself [4]. The effects of these two kinds of decays on the relic density of the metastable colored particles or DM are different. Since we assume that the constituent particles in the bound state have the same discrete symmetry as the DM particle, the annihilation decay to SM particles remove, for example, two R-odd numbers in SUSY, while the individual constitute particle decay does not change the R-odd number. For the colored particle coannihilating in the WIMP scenario and the metastable colored particle in the superWIMP scenario, the individual constituent

[4] It should be noted that the prerequisite of forming a bound state is that the constituent particle decay width has to be smaller than the bound state formation time a^{-1}.

particle decay rate is suppressed either by the small mass difference or by the very small coupling between the massive colored particle and the DM particle [5], while the annihilation decay rate is not suppressed and is proportional to the large mass of the colored particle. Therefore, we will hereafter neglect the individual constitute particle decay rate compared to the annihilation decay rate.

5.3 Results

Here, we present the full bound-state formation and dissociation cross sections for the cases of S3, F3, S8 and F8, as well as the annihilation decay rates.

S3 and F3

Since we consider that the bound state is a color-singlet state, the emission (absorption) of a gluon in the bound-state formation (dissociation) process dictates that for both S3 and F3 the free pair state must be in a color-octet state (see Eq. (5.4)), due to color charge conservation. The normalized color wave function is $\delta_{kj}/\sqrt{3}$ for the bound state, and $\lambda^b_{ij}/\sqrt{2}$ for the free pair, where λ^b_{ij} are the Gell-Mann matrices, and the color indices $i, j, k = 1-3$, $b = 1-8$. The generator $\mathbf{T}_c$ takes the form $\lambda^c_{ki}/2$. Therefore, the color part of the wave functions contributes to σ_{dis} as

$$\left|\frac{\lambda^b_{ij}}{\sqrt{2}}\frac{\lambda^c_{ki}}{2}\frac{\delta_{kj}}{\sqrt{3}}\right|^2 = \left|\frac{\delta^{bc}}{\sqrt{6}}\right|^2 = \frac{4}{3}\,. \tag{5.19}$$

For S3, there is no spin wave function to worry about. While for F3, without considering the bound state, a pair of heavy colored fermion and anti-fermion can have 3/4 chance in a spin-triplet configuration with $S = 1$ and 1/4 chance in a spin-singlet configuration with $S = 0$. Since we only consider a bound state with $S = 0$, then by neglecting the spin-orbit interaction we will only consider a free pair that is also in $S = 0$ state. Therefore, we consider that both the bound state and the free pair have the same spin wave function, given as

$$(\uparrow\downarrow - \downarrow\uparrow)/\sqrt{2}\,, \tag{5.20}$$

so that the spin part of the wave functions does not introduce a factor for σ_{dis}. However, in the next section we will see that when including the bound-state formation and dissociation cross sections in the Boltzmann equation, we need to introduce an additional

[5] This is the case in the MSSM for a Bino-like neutralino LSP coannihilating with a stop, when the two-body decay of the stop into top and neutralino is kinematically forbidden, and indeed coannihilation is responsible for giving the correct DM relic abundance for the small mass difference range [130]. For a neutralino LSP coannihilating with a gluino, the gluino decay rate can be very suppressed by the small mass difference as well as by large squark masses in the propagator [121]. For a gravitino or axino LSP, its coupling with the NLSP is suppressed by the Planck or the Peccei-Quinn scale.

factor of 1/4 for F3 compared to S3 to take into account the fact that we have only considered the $S = 0$ possibility in the former.

Putting the factor of 1/8 from the incoming gluon color averaging, the factor of 4/3 from the color part of the wave functions, and by noticing that the free pair has a repulsive potential with $\zeta' = 1/2 \times (4/3 + 4/3 - 3)\alpha_s = (-1/6)\alpha_s$ (see Eq. (5.3)), we get the full dissociation cross section for S3 and F3,

$$\sigma_{dis}^{S3,F3} = \frac{1}{8} \times \frac{4}{3} \times \sigma_{dis,r}^{0}\,, \tag{5.21}$$

in which the quantities inside $\sigma_{dis,r}^{0}$ are given in Eqs. (5.7), (5.8), (5.13) and (5.14) with $\zeta = (4/3)\alpha_s$. From Eq. (5.18), the bound-state formation cross sections are

$$\sigma_{bsf}^{S3} = \frac{1 \times 16}{3 \times 3} \frac{\omega^2}{(\mu v_{rel})^2} \times \sigma_{dis}^{S3,F3} \tag{5.22}$$

and

$$\sigma_{bsf}^{F3} = \frac{1 \times 16}{6 \times 6} \frac{\omega^2}{(\mu v_{rel})^2} \times \sigma_{dis}^{S3,F3}\,, \tag{5.23}$$

where the degrees of freedom are written explicitly.

For the bound-state annihilation decay, we consider the dominant decay mode only, which is the two-gluon final state (see e.g. [155]), and the results are

$$\Gamma_{\eta}^{S3} = \frac{1}{3}\mu\alpha_s^2\zeta^3 \tag{5.24}$$

and

$$\Gamma_{\eta}^{F3} = \frac{2}{3}\mu\alpha_s^2\zeta^3, \tag{5.25}$$

where $\zeta = (4/3)\alpha_s$. In the above two equations, the α_s factor explicitly written is evaluated at the scale of $2m_X$, while the α_s inside ζ is evaluated at the scale of the inverse Bohr radius, a^{-1}.

S8 and F8

Due to the nature of identical particles, the total wave functions need to be symmetric for S8 whereas anti-symmetric for F8.

The F8 case was studied in detail in [121], and the result for the gluon dissociation of a color-$\mathbf{1}_S$ bound state with $(S = 0, L = 0)$ into a free pair in an $\mathbf{8}_A$ state with $(S = 0, L = 1)$ is

$$\sigma_{dis}^{F8} = 3 \times 4 \times \frac{1}{8} \times \frac{1}{2} \times \sigma_{dis,a}^{0}\,, \tag{5.26}$$

where the factor 3 comes from the color part of the wave functions together with the generator $\mathbf{T}_c = -if_{cde}$ in the coupling between the gluon and the massive colored particle, where f_{cde} are the SU(3) structure constants. The factor 4 comes from symmetrization of the spatial part of the bound-state wave function ($L = 0$) and anti-symmetrization of the spatial part of the free pair wave function ($L = 1$). 1/8 comes from the color averaging of the incoming gluon. The factor 1/2 is introduced to avoid double counting of the two identical massive colored particle in the outgoing free pair phase-space integration. The spin part of the wave functions do not introduce any extra factor. The quantities inside $\sigma^0_{dis,a}$ are given in Eqs. (5.7), (5.8), (5.13) and (5.14) with $\zeta = 3\alpha_s$ and $\zeta' = 1/2 \times (3 + 3 - 3)\alpha_s = (3/2)\alpha_s$.

The S8 case is exactly the same as the F8 case, namely, a transition from a color-$\mathbf{1}_S$ bound state with $(S = 0, L = 0)$ into a color-8_A free pair state with $(S = 0, L = 1)$. The only difference is that while for the F8 case the $S = 0$ state means that the spin wave function is anti-symmetric (i.e., a spin-singlet configuration), for the S8 case there is no spin to worry about, so that for the latter the total wave functions for both bound state and free pair state are symmetric, as they should be. Therefore, we have

$$\sigma^{S8}_{dis} \;=\; \sigma^{F8}_{dis} \;\equiv\; \sigma^{S8,F8}_{dis}\,. \tag{5.27}$$

The corresponding bound-state formation cross sections are

$$\sigma^{S8}_{bsf} \;=\; 2 \times \frac{1 \times 16}{8 \times 8} \frac{\omega^2}{(\mu v_{rel})^2} \times \sigma^{S8,F8}_{dis} \tag{5.28}$$

and

$$\sigma^{F8}_{bsf} \;=\; 2 \times \frac{1 \times 16}{16 \times 16} \frac{\omega^2}{(\mu v_{rel})^2} \times \sigma^{S8,F8}_{dis}\,, \tag{5.29}$$

where the factor of 2 in the front of the right-hand side of the two equations is actually the factor of 1/2 which would have been in the left-hand side of Eq. (5.18) to avoid double counting the number of bound-state formation reactions. In Eqs. (5.28) and (5.29), the degrees of freedom are written explicitly.

Again, we consider the dominant two-gluon annihilation decay channel only, and the annihilation decay rates are (see e.g. [155]),

$$\Gamma^{S8}_{\eta} \;=\; \frac{9}{4}\mu\alpha_s^2\zeta^3, \tag{5.30}$$

and

$$\Gamma^{F8}_{\eta} \;=\; \frac{9}{2}\mu\alpha_s^2\zeta^3, \tag{5.31}$$

where $\zeta = 3\alpha_s$. The scales of evaluating the α_s explicitly written and the one inside ζ in the above two equations are understood similarly as in the S3 and F3 cases.

5.4 Thermal averaging

Let us note that in order to study the bound-state effects on the relic abundance of the massive colored particles or the DM, we need the thermally-averaged bound-state dissociation and annihilation decay rates, as well as the formation cross section times the relative velocity of the free pair, since it is these quantities that appear in the Boltzmann equation which determines the evolution of the density of the massive colored particles or the DM with temperature, T. By defining two dimensionless variables, $z \equiv E_B/T$ and $u \equiv \frac{1}{2}\mu v_{rel}^2/T$, we can rewrite σ_{dis} and σ_{bsf} as functions of z and u, together with factors not changing with T. In particular, the relevant quantities are expressed as

$$\omega = E_B\left(1+\frac{u}{z}\right), \tag{5.32}$$

$$\nu = \left(\frac{z}{u}\right)^{\frac{1}{2}}\kappa^{-1}, \quad \text{for } \zeta' \neq 0, \tag{5.33}$$

$$v_{rel} = \zeta\left(\frac{u}{z}\right)^{\frac{1}{2}}. \tag{5.34}$$

The thermally-averaged bound-state dissociation rate is

$$\langle\Gamma\rangle_{dis} = g_g\frac{4\pi}{(2\pi)^3}\int_{E_B}^{\infty}\sigma_{dis}\frac{\omega^2 d\omega}{e^{\omega/T}-1} = g_g\frac{4\pi}{(2\pi)^3}\int_0^{\infty}\sigma_{dis}\frac{E_B^3\left(1+\frac{u}{z}\right)^2 du}{z\left(e^{z+u}-1\right)}. \tag{5.35}$$

The thermally-averaged bound-state formation cross section times relative velocity is

$$\langle\sigma v\rangle_{bsf} = \int_0^{\infty}\sigma_{bsf}v_{rel}f(v_{rel})\left(1+\frac{1}{e^{\omega/T}-1}\right)dv_{rel}, \tag{5.36}$$

with $f(v_{rel})$ given in Eq. (4.15).

The factor $\frac{1}{e^{\omega/T}-1}$ in Eq. (5.36) accounts for the stimulated emission due to the gluons in the thermal bath. Using Eqs. (5.34) and (5.8), $\langle\sigma v\rangle_{bsf}$ can be rewritten as

$$\langle\sigma v\rangle_{bsf} = \int_0^{\infty}\sigma_{bsf}\zeta\left(\frac{u}{z}\right)^{\frac{1}{2}}\frac{2}{\sqrt{\pi}}u^{1/2}e^{-u}\left(1+\frac{1}{e^{z+u}-1}\right)du. \tag{5.37}$$

The thermally-averaged bound-state annihilation decay rate is

$$\langle\Gamma\rangle_\eta = \Gamma_\eta\langle\frac{m_\eta}{E_\eta}\rangle \approx \Gamma_\eta\frac{\int_{m_\eta}^{\infty}\frac{m_\eta}{E_\eta}e^{-E_\eta/T}d^3\vec{p}_\eta}{\int_{m_\eta}^{\infty}e^{-E_\eta/T}d^3\vec{p}_\eta} = \Gamma_\eta\frac{K_1(m_\eta/T)}{K_2(m_\eta/T)}, \tag{5.38}$$

where m_η is the mass of the bound state, given as $m_\eta = m_{X_1} + m_{X_2} - E_B$. In the above formula, we have assumed the Maxwell-Boltzmann approximation for the bound-state equilibrium distribution, and $K_{1,2}(m_\eta/T)$ are the modified Bessel functions of the second kind. At $m_\eta \gg T$, $\langle\Gamma\rangle_\eta \approx \Gamma_\eta$.

5.5 Boltzmann equations revisited

We now have all the tools to write down and solve the Boltzmann equations of interest governing the evolution of particle number density in the expanding universe. The general formulae for N species of exotic particles are given in [122]. For our purpose, we consider at most two exotic particles in the thermal bath: the colored particle X and DM χ, with degree of freedom g_X and g_χ respectively, [6] and by considering that they share the same discrete symmetry stabilizing DM, we assume the decay of the massive colored particle produced one DM together with some SM particles. In the WIMP scenario, we are interested in the coannihilation between the two exotic species. As highlighted in [121, 156], coannihilation is effective only if the interconversion rate between the two species is sufficiently large compared to the Hubble expansion rate, otherwise the two species would freeze out separately. Without committing to specific particle theory models, in this work we assume the interconversion rate is sufficiently large so that the two species freeze-out together and we can use a single Boltzmann equation to calculate the DM density. We emphasis that this condition needs to be checked when one consider coannihilations in specific DM models.

Also, as we are mainly interested in QCD interactions and further model specifications would have been needed, in our calculation we neglect the (co)annihilation cross sections for DM - DM and DM - massive colored particle, in comparing to the annihilation cross sections between the massive colored particles. In the WIMP DM scenario, indeed this is usually a good approximation. For example, for the right-handed stop-Bino coannihilation in the MSSM, the stop - antistop annihilation to gg channel dominates the effective annihilation cross section in the coannihilation region for an $\mathcal{O}$(TeV) Bino [132], if the ratio of the lighter stop - heavier stop - Higgs coupling to heavier stop mass is not very large [130]; for the gluino-neutralino coannihilation, the gluino pair annihilations to gg and $q\bar{q}$ dominate over the neutralino-gluino and neutralino pair (co)annihilation cross sections.

[6] For the case where χ is a superWIMP, where χ is never in the thermal bath, we simply impose $g_\chi = 0$ in our formulae.

With these specifications, the following set of coupled Boltzmann equations apply:

$$\frac{dY_\chi}{dx} = \frac{xs}{H(m_\chi)}\Big[\langle\Gamma\rangle_X \frac{1}{s}\left(Y_X - Y_X^{eq}\frac{Y_\chi}{Y_\chi^{eq}}\right)\Big], \tag{5.39}$$

$$\frac{dY_X}{dx} = \frac{xs}{H(m_\chi)}\Big[-\langle\sigma v\rangle_{XX}\left(Y_X Y_X - Y_X^{eq}Y_X^{eq}\right) - \langle\Gamma\rangle_X \frac{1}{s}\left(Y_X - Y_X^{eq}\frac{Y_\chi}{Y_\chi^{eq}}\right) - \langle\sigma v\rangle_{bsf}\left(Y_X Y_X - Y_X^{eq}Y_X^{eq}\frac{Y_\eta}{Y_\eta^{eq}}\right)\Big], \tag{5.40}$$

$$\frac{dY_\eta}{dx} = \frac{xs}{H(m_\chi)}\Big[-\langle\Gamma\rangle_\eta \frac{1}{s}\left(Y_\eta - Y_\eta^{eq}\right) - \langle\sigma v\rangle_{X\eta\to Xg} Y_X\left(Y_\eta - Y_\eta^{eq}\right) + \langle\sigma v\rangle_{bsf}\left(Y_X Y_X - Y_X^{eq}Y_X^{eq}\frac{Y_\eta}{Y_\eta^{eq}}\right)\Big], \tag{5.41}$$

where

$$x \equiv \frac{m_\chi}{T},\ s = \frac{2\pi^2}{45}g_{*s}T^3,\ H(m_\chi) \equiv H(T)x^2 = \left(\frac{4\pi^3 G_N g_*}{45}\right)^{\frac{1}{2}} m_\chi^2, \tag{5.42}$$

G_N being the gravitational constant, and g_{*s}, g_* are the numbers of degrees of freedom associated with the entropy density and the energy density respectively.

Rewriting Eq. (5.41) as:

$$\frac{d\ln Y_\eta}{d\ln x} = -\frac{\langle\Gamma\rangle_\eta + \langle\sigma v\rangle_{X\eta\to Xg} n_X}{H(T)}\left(1 - \frac{Y_\eta^{eq}}{Y_\eta}\right) + \frac{\frac{1}{2}\langle\sigma v\rangle_{bsf} n_X\left(\frac{Y_X}{Y_\eta}\right)}{H(T)}\left[1 - \left(\frac{Y_X^{eq}}{Y_X}\right)^2\left(\frac{Y_\eta}{Y_\eta^{eq}}\right)\right], \tag{5.43}$$

we can see that LHS of Eq. (5.43) is of order -10, the terms on the RHS of Eq. (5.43) are of order $\alpha_s^5 M_P/m_\chi \gg 10$. Therefore, under the approximation that the LHS of Eq. (5.43) is zero, we can write $\left(\frac{Y_\eta}{Y_\eta^{eq}}\right)$ as:

$$\frac{Y_\eta}{Y_\eta^{eq}} = \frac{\langle\Gamma\rangle_\eta + \langle\sigma v\rangle_{X\eta\to Xg} n_X + \langle\Gamma\rangle_{dis}\left(\frac{Y_X}{Y_X^{eq}}\right)^2}{\langle\Gamma\rangle_\eta + \langle\sigma v\rangle_{X\eta\to Xg} n_X + \langle\Gamma\rangle_{dis}}, \tag{5.44}$$

where

$$\langle\Gamma\rangle_{dis} = \frac{1}{2}\langle\sigma v\rangle_{bsf}(n_X^{eq})^2/n_\eta^{eq}. \tag{5.45}$$

Hence, the evolution of the total number density of exotic particles over the entropy density, $\tilde{Y} \equiv (n_X + n_\chi)/s$ can be described by a single Boltzmann equation as follows:

$$\frac{d\tilde{Y}}{dx} = \frac{xs}{H(m_\chi)}\Big[-\langle\sigma v\rangle_{XX}\left(Y_X Y_X - Y_X^{eq}Y_X^{eq}\right) - \langle\sigma v\rangle_{bsf}\frac{\langle\Gamma\rangle_\eta + \langle\sigma v\rangle_{X\eta\to Xg} n_X}{\langle\Gamma\rangle_\eta + \langle\sigma v\rangle_{X\eta\to Xg} n_X + \langle\Gamma\rangle_{dis}}\left(Y_X Y_X - Y_X^{eq}Y_X^{eq}\right)\Big]. \tag{5.46}$$

While calculating the relic abundance we are only interested in the temperature of the universe where X is non-relativistic. Hence $\langle\sigma v\rangle_{X\eta\to Xg} n_X$ can be ignored.

The Boltzmann equation can be written more succinctly using an effective cross section $\langle\sigma_{eff} v\rangle$:

$$\frac{d\tilde{Y}}{dx} = -\frac{xs}{H(m_\chi)}\left(1+\frac{T}{3g_{*s}}\frac{dg_{*s}}{dT}\right)\langle\sigma_{eff}v\rangle\left(\tilde{Y}^2-\tilde{Y}_{eq}^2\right), \tag{5.47}$$

We define $\Delta \equiv (m_X - m_\chi)/m_\chi$ and $g_{eff} \equiv g_\chi + g_X(1+\Delta)^{3/2}e^{-\Delta x}$. Then, the effective annihilation cross section without bound-state effects, $\langle\sigma_{eff}v\rangle'$ can be written as

$$\langle\sigma_{eff}v\rangle' = \langle\sigma v\rangle_{XX}\frac{g_X^2(1+\Delta)^3 e^{-2\Delta x}}{g_{eff}^2}, \tag{5.48}$$

where $\langle\sigma v\rangle_{XX}$ is the total annihilation cross section of X into quarks and gluons with Sommerfeld effects included.

Following arguments above, the effects of bound states are incorporated by replacing $\langle\sigma v\rangle_{XX}$ with the following terms:

$$\langle\sigma v\rangle_{XX} \to \langle\sigma v\rangle_{XX} + \langle\sigma v\rangle_{bsf}\frac{\langle\Gamma\rangle_\eta}{\langle\Gamma\rangle_\eta + \langle\Gamma\rangle_{dis}}. \tag{5.49}$$

The formula has the following physical interpretation: the reactions of bound states occur at a timescale much shorter than the Hubble scale such that if one is interested in the change in the number density of X/χ, one does not have to trace the evolution of bound state number density by solving the coupled Boltzmann equations. Once the bound state of X is formed, it either decays to SM particles, reducing the number density of X/χ, or dissociate back to X immediately. These processes feed directly into the annihilation cross section as in Eq. (5.49). As a result, the annihilation cross section of X is effectively enhanced as a new channel involving X annihilating to the bound state is now open.

5.6 Bound-state effects

In order to demonstrate the effects of bound states, we plot for S3 (stop) and F8 (gluino) in Fig. 5.1 and Fig. 5.2 the temperature dependences of the Sommerfeld-corrected annihilation cross section (orange line), i.e.

$$\frac{\langle\sigma v_{rel}(XX\to gg, q\bar{q})\rangle_{\text{Sommerfeld}}}{\langle\sigma v_{rel}(XX\to gg, q\bar{q})\rangle_{\text{w/o Sommerfeld}}}, \tag{5.50}$$

the thermally-averaged bound-state formation cross section with (solid black curve) and without (dotted black curve) considering bound state dissociation and annihilation decay

rates, also normalized to the tree-level $XX \to gg, q\bar{q}$ annihilation cross section, i.e.,

$$\frac{\langle\sigma v\rangle_{bsf}\frac{\langle\Gamma\rangle_\eta}{\langle\Gamma\rangle_\eta+\langle\Gamma\rangle_{dis}}}{\langle\sigma v_{rel}(XX\to gg,q\bar{q})\rangle_{\text{w/o Sommerfeld}}} \quad \text{and} \quad \frac{\langle\sigma v\rangle_{bsf}}{\langle\sigma v_{rel}(XX\to gg,q\bar{q})\rangle_{\text{w/o Sommerfeld}}}\,, \tag{5.51}$$

respectively, and with purple curves for the same ones but multiplied by a factor of 2 in the bound-state formation cross section (solid and dotted) and dissociation rate (solid), that is [7],

$$\frac{2\langle\sigma v\rangle_{bsf}\frac{\langle\Gamma\rangle_\eta}{\langle\Gamma\rangle_\eta+2\langle\Gamma\rangle_{dis}}}{\langle\sigma v_{rel}(XX\to gg,q\bar{q})\rangle_{\text{w/o Sommerfeld}}} \quad \text{and} \quad \frac{2\langle\sigma v\rangle_{bsf}}{\langle\sigma v_{rel}(XX\to gg,q\bar{q})\rangle_{\text{w/o Sommerfeld}}}\,. \tag{5.52}$$

As can be observed from the plots, at early times where the gluons in the thermal bath are energetic, the dissociation rate is so large that once the bound state is formed, it is quickly dissociated away without decaying via annihilation. A factor of 2 increase of the bound state effect has little effect on the effective annihilation cross section, and there is no contribution to reducing the relic abundance at early times. Bound-state effects are important only during the time when the dissociation rate is smaller than the decay rate. This happens at $x \gtrsim m_X/E_B \sim 1/\alpha_s^2 \sim 100$, where the gluon in the thermal plasma is no longer energetic enough to dissociate the bound state. Then, the bound state decays via annihilation and contributes to reducing the relic abundance. Also can be observed from the plots is the fact that the bound-state effects can be comparable or larger than the Sommerfeld effects. [8]

There is a qualitative difference between the S3 and F8 cases at $E_B/T \gg 1$: while in the F8 case the solid black and purple curves keep growing with the decrease of temperature, in the S3 case they are decreasing after achieving maximum values around $E_B/T \sim 2$. This is due to the fact that an S3 incoming pair feels a repulsive potential prior to forming a bound state, while the potential is attractive for an F8 incoming pair.

[7] To account for the errors involving the evaluations of α_s's [157], the corrections from a more accurate QCD potential and the thermal mass of the gluon [145], as well as the possibility that excited bound states may also contribute to the bound-state effect [146], we plot purple curves in this and following figures with an uncertainty of a factor of 2.

[8] We use a common value, $\alpha_s = 0.1$, for all the α_s's appearing in the formulae for the curves in Figs. 5.1,5.2 and the upper left, upper right and lower left panels in Fig. 6.5. In this way, all the ratios do not depend on m_X. However, we note that in other parts of this paper and other plots, α_s's are evaluated differently: the α_s's appearing in the Sommerfeld factors in Eq. (4.16) are evaluated at βm_X which is the typical scale of the momentum transfer of the soft-gluon exchanges which are responsible for the Sommerfeld effect [142], and we take $\beta = 0.3$, which is roughly the average of the thermal velocities of the X's at the freeze-out temperature; the α_s's in the bound-state formation cross sections and dissociation rates, as well as in the ζ part of the annihilation decay rates (given in Eqs. (5.24), (5.25), (5.30) and (5.31)), are evaluated at the bound-state inverse Bohr radius scale; the α_s's in the tree-level $XX \to gg, q\bar{q}$ annihilation cross sections and the ones appearing explicitly in the bound-state annihilation decay rates, are evaluated at the scale of $2m_X$.

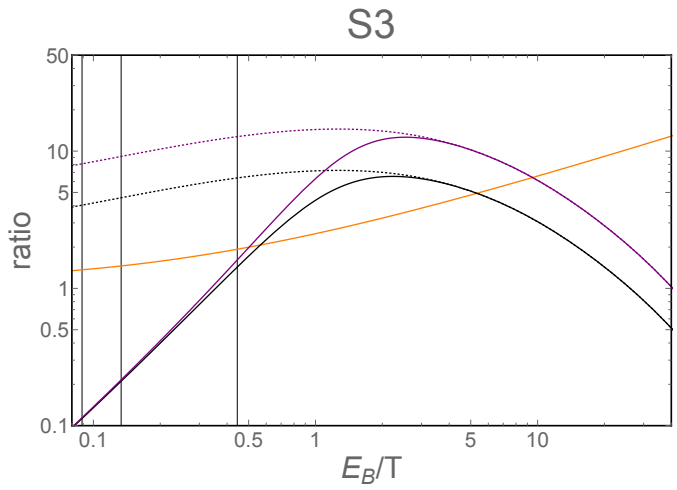

Figure 5.1: The S3 (stop) Sommerfeld-corrected annihilation cross section (orange line), effective annihilation cross section due to bound states (second term in the RHS of Eq. (5.49); black line), and effective bound-state annihilation cross section multiplied by 2 (where $\langle\sigma v\rangle_{bsf}$ and $\langle\Gamma\rangle_{dis}$ are 2 times larger; purple line) as a function of E_B/T. Together we also plot the effective annihilation cross section due to bound states *without* taking into account the dissociation process ($\langle\Gamma\rangle_{dis} = 0$; black and purple dotted lines). All plotted cross sections are normalized with respect to the tree-level annihilation cross section. The vertical black dotted lines correspond to, from left to right, $x = m_X/T = 20, 30, 100$.

At lower temperature, there is a smaller fraction of the incoming S3 pairs which have enough kinetic energy to overcome the repulsive potential to form bound states. While for the F8 case, a low temperature (and hence small velocities) favors the formation of the bound state, similar to that of the Sommerfeld enhancement.

Let us return to solving the Boltzmann equation in Eq. (5.47). In order to obtain the value of $\tilde{Y}$ at late time ($x \to \infty$), one solves the equation from a freeze-out temperature T_f where the number density $\tilde{Y}$ starts to depart from its equilibrium value $\tilde{Y}_{eq}$, such that the last term of the RHS of Eq. (5.47) can be dropped:

$$\frac{d\tilde{Y}}{dx} \simeq -\frac{xs}{H(m_\chi)}\left(1+\frac{T}{3g_{*s}}\frac{dg_{*s}}{dT}\right)\langle\sigma_{eff}v\rangle\left(\tilde{Y}^2\right). \tag{5.53}$$

This typically occurs at $x_f = 20 \sim 30$. Integrating both sides from $x = x_f \equiv m_\chi/T_f$ to $x = \infty$, we get

$$\frac{1}{\tilde{Y}(x=\infty)} \simeq \frac{1}{\tilde{Y}(x_f)} + \int_{x_f}^{\infty} dx \frac{xs}{H(m_\chi)}\left(1+\frac{T}{3g_{*s}}\frac{dg_{*s}}{dT}\right)\langle\sigma_{eff}v\rangle. \tag{5.54}$$

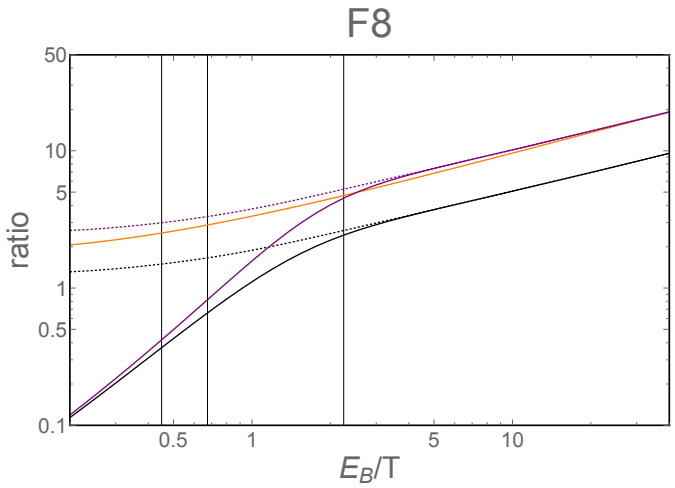

Figure 5.2: The F8 (gluino) Sommerfeld-corrected annihilation cross section (orange line), effective annihilation cross section due to bound states (second term in the RHS of Eq. (5.49); black line), and effective bound-state annihilation cross section multiplied by 2 (where $\langle\sigma v\rangle_{bsf}$ and $\langle\Gamma\rangle_{dis}$ are 2 times larger; purple line) as a function of E_B/T. Together we also plot the effective annihilation cross section due to bound states *without* taking into account the dissociation process ($\langle\Gamma\rangle_{dis} = 0$; black and purple dotted lines). All plotted cross sections are normalized with respect to the tree-level annihilation cross section. The vertical black dotted lines correspond to, from left to right, $x = m_X/T = 20, 30, 100$.

For the typical case where $\langle\sigma_{eff}v\rangle$ is independent of temperature, the last term of the RHS of Eq. (5.54) is negligible, and the present-time relic abundance equals to its value at freeze-out. However, this is not true for Sommerfeld-enhanced processes and bound-state effects, where late-time annihilations are important. Sommerfeld effects become important when the relative velocity of the annihilating particles is low. Moreover, discussed, bound-state effects are important only $x \gtrsim m_X/E_B \sim 1/\alpha_s^2 \sim 100$, where the gluon in the thermal plasma is no longer energetic enough to dissociate the bound state. Therefore, the common wisdom assuming that the number density of relics suddenly freezes out at x_f does not apply.

To demonstrate these effects, we plot for S3 (stop) and F8 (gluino) in Fig. 5.3 and Fig. 5.4 the change of $\tilde{Y}$ with respect to temperature in the coannihilation scenario (assuming DM has a total number of degree of freedom 2). For S3 (F8), we take $m_X = 2$ TeV ($m_X = 8$ TeV), and the mass splitting between DM and the colored particle 5 GeV (15 GeV), which will reproduce the observed relic abundance as will be shown in the next Section. The red, orange, black and purple lines show the calculation without Sommerfeld and bound-state effects, with Sommerfeld but without bound-state effects, with Sommerfeld and bound-state effects, and with Sommerfeld and two times the bound-state effects, respectively. The solid lines correspond to the solution where the full Boltzmann equation (Eq. (5.47)) is solved numerically. The dashed lines correspond to the approximate solution using Eq. (5.54), where the freeze-out temperature is taken to be $x_f = 30$, and the yield during freeze-out is calculated numerically using the full Boltzmann equation. The fact that the solid and dashed lines almost overlap with each other shows that Eq. (5.54) is a good approximation.

It can be noted from the plots that the values of $\tilde{Y}$ at freeze-out ($x_f = 30$, corresponding to the second vertical black dotted line from the left) is different from its value at $x \to \infty$. This is particularly apparent for the case with Sommerfeld and bound-state effects included, where the difference between $\tilde{Y}_{x_f}$ and $\tilde{Y}(x \to \infty)$ can be larger than an order of magnitude. Therefore, in order to take Sommerfeld and bound-state effects into account appropriately, one must integrate the Boltzmann equation at least until $T \lesssim E_B$.

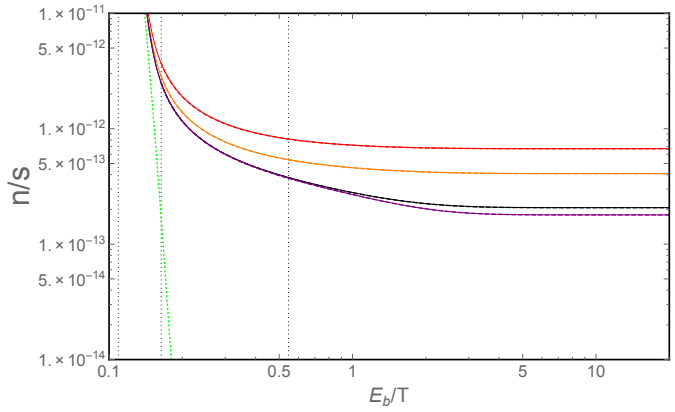

Figure 5.3: The yield $\tilde{Y}$ as a function of E_B/T for the S3 (stop) coannihilation scenario. The red, orange, black and purple lines show the calculation without Sommerfeld and bound-state effects, with Sommerfeld but without bound-state effects, with Sommerfeld and bound-state effects, and with Sommerfeld and two times the bound-state effects, respectively. The solid lines correspond to the solution where the full Boltzmann equation (Eq. (5.47)) is solved numerically. The dashed lines correspond to the approximate solution using Eq. (5.54), where the freeze-out temperature is taken to be $x_f = 30$, and the yield during freeze-out is calculated numerically using the full Boltzmann equation. The green dashed line correspond to the equilibrium value of $\tilde{Y}$. The vertical black dotted lines correspond to, from left to right, $x = m_X/T = 20, 30, 100$.

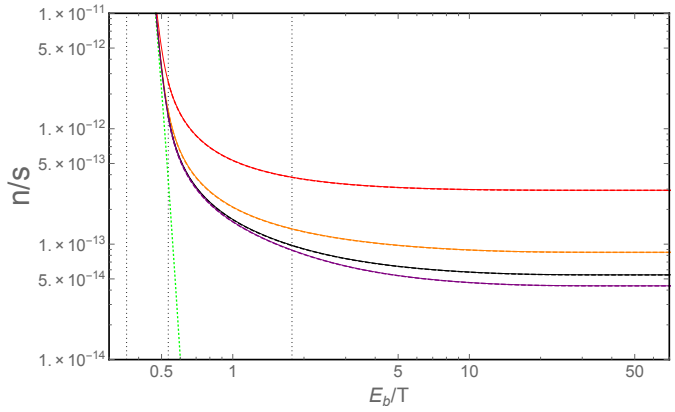

Figure 5.4: The yield $\tilde{Y}$ as a function of E_B/T for the F8 (gluino) coannihilation scenario. The red, orange, black and purple lines show the calculation without Sommerfeld and bound-state effects, with Sommerfeld but without bound-state effects, with Sommerfeld and bound-state effects, and with Sommerfeld and two times the bound-state effects, respectively. The solid lines correspond to the solution where the full Boltzmann equation (Eq. (5.47)) is solved numerically. The dashed lines correspond to the approximate solution using Eq. (5.54), where the freeze-out temperature is taken to be $x_f = 30$, and the yield during freeze-out is calculated numerically using the full Boltzmann equation. The green dashed line correspond to the equilibrium value of $\tilde{Y}$. The vertical black dotted lines correspond to, from left to right, $x = m_X/T = 20, 30, 100$.

Chapter 6

Implications and applications

In this chapter, we study implications of colored bound states and the applications of our techniques to several early-universe scenarios. We first discuss how our calculations change the BBN constraints on long-lived particles. We then study non-thermal contribution of such particles to the relic abundance of superWIMP. Next, we study coannihilating WIMP scenarios. Collider constraints and effects of electric charge will also be discussed.

Before delving deeper into the phenomenology of bound states, let us remind the readers again limitations and assumptions of our calculations. Firstly, we do not include higher order corrections to the QCD Coulomb potential and the thermal mass of the gluon. Secondly, we consider only the ground state, which is expected to be most copiously produced. However, these effects are expected to be small, as explained in Section 5.1. We nevertheless show results with a factor of 2 enhancement of the bound-state effects from the considerations of the excited states contribution as well as other uncertainties in our calculations.

6.1 Bounds on long-lived colored particles

We compare the relic abundance of the long-lived particles with the bounds from the BBN. Injection of energetic particles into the thermal plasma during BBN change predictions on the abundance of light elements. The fact that the observed abundance of light elements agreeing well with standard BBN processes place a stringent constraint on the long-lived relic's abundance [158–167]. Generically, the BBN bounds can constrain particles of lifetime $\tau \gtrsim 0.1$s. Examples of such metastable particles can be found in R-parity conserving SUSY models with a gravitino [168–172] or axino LSP [173–175]. Another motivation is split SUSY [176–178]. Gluino NLSP (neutralino being the LSP) can be long-lived if the squarks are much heavier.

It is well-known that the concordance of the standard BBN predications of the pri-

mordial light-element abundances with the values inferred from observational data, provides strong constraints on the abundance, mass, lifetime, and decay spectra of a massive particle decaying during or after BBN (see e.g. [164]). Since our focus in this work is to study the impacts of the bound-state effect of massive colored particles, we want to see how much the bound-state effect can change the BBN constraints on the abundance and mass comparing to in particular the Sommerfeld effect, for a given lifetime and decay spectra which depend on other details of a specific particle theory model. With this in mind, we simply use the parametrization given in Eq. (56) of [157] for the BBN constraints obtained by [164] for a massive metastable particle with a lifetime of $\sim 0.1 - 10^2$ sec and assuming that its hadronic decay branching ratio is 1 (which can be a good approximation for a massive colored particle), given as

$$Y_X \leqslant 1.0 \times 10^{-13} \left(\frac{m_X}{1\,\text{TeV}}\right)^{-0.3} \quad \text{for} \;\; \tau_X \sim 0.1 - 10^2\,\text{s}\,. \tag{6.1}$$

The above constraint comes from the would be overproduction of He^4, due to the new proton $\leftrightarrow$ neutron interconversion reactions induced by the hadronic shower from X decays. In Eq. (6.1), Y_X is the sum of the yield for particle and anti-particle in our convention.

We show in Fig. 6.1 and Fig. 6.2 Y_X as functions of m_X for the S3 and F8 cases, calculated using Eq. (5.47) with the meanings of the variables understood as mentioned at the end of Sec. 5.5 for massive colored particles. As before, the red, orange, black and purple lines are results without the Sommerfeld and bound-state effects, with the Sommerfeld effect but without bound-state effect, with both the Sommerfeld and bound-state effect, and with Sommerfeld effect and a factor of 2 enlargement of the bound-state effect, respectively. The blue dashed line is given by Eq. (6.1), and the parameter region above this line is excluded for an X with a lifetime of $\sim 0.1 - 10^2$ sec. We can see that the bound-state effect pushes the allowed regions of m_X to larger values compared to the ones with the Sommerfeld effect included only, namely, $\sim 1.1 \to 2.1$ TeV and $\sim 8 \to 11$ TeV for S3 and F8, respectively. As will be discussed more in the next Section, since the LHC is pushing the exclusion limit of long-lived colored particles to TeV scale, it is useful to update the exclusion limit from BBN as well by including the previously omitted bound-state effect, so that we can be more confident to close or to leave open the mass window a long-lived colored particle can have.

We note that in our calculations of the relic abundance of massive colored particles, we have not included the possible further reduction of the abundance due to annihilations of heavy exotic color-neutral hadrons, which are formed by not-yet-decayed massive colored particles together with quarks and gluons after the quark-hadron phase transition in the early Universe [179, 180]. In this sense, the BBN constraints given here are conservative. The contribution to $\Omega_{\text{SW}}^{\text{non-th}} h^2$ from the massive colored particle decays becomes smaller as well if there is further reduction of $\Omega_X h^2$ after the quark-hadron phase

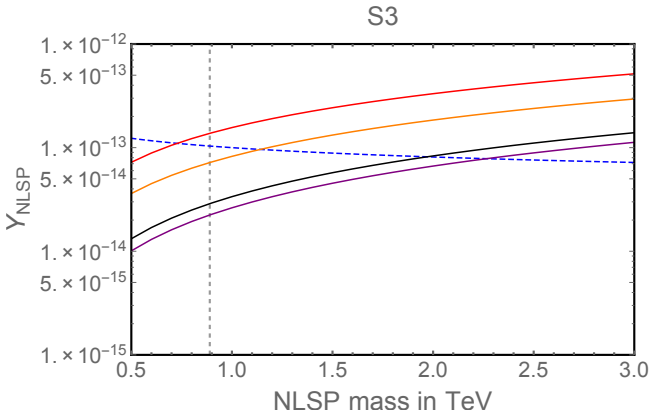

Figure 6.1: The total yield of the massive colored particles as a function of the mass, for the S3 case, calculated without the Sommerfeld and bound-state effects (red line), with the Sommerfeld effect but without bound-state effect (orange line), with both the Sommerfeld and bound-state effect (black line), and with Sommerfeld effect and a factor of 2 enlargement of the bound-state effect (purple line). The blue dashed line is the constraint given in Eq. (6.1). The vertical dashed line is the mass lower limit on the long-lived massive colored particle from collider constraints as demonstrated in Sec. 6.4.

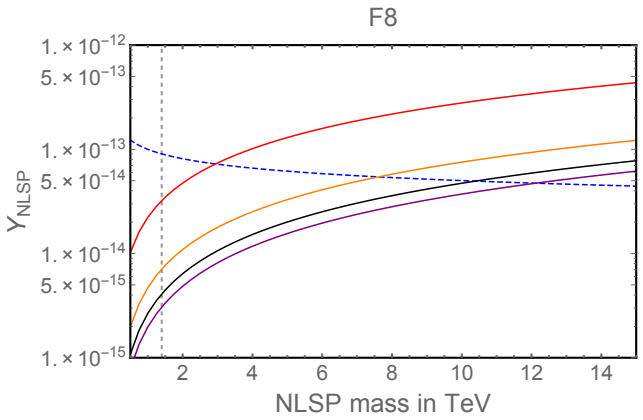

Figure 6.2: The total yield of the massive colored particles as a function of the mass, for the F8 case, calculated without the Sommerfeld and bound-state effects (red line), with the Sommerfeld effect but without bound-state effect (orange line), with both the Sommerfeld and bound-state effect (black line), and with Sommerfeld effect and a factor of 2 enlargement of the bound-state effect (purple line). The blue dashed line is the constraint given in Eq. (6.1). The vertical dashed line is the mass lower limit on the long-lived massive colored particle from collider constraints as demonstrated in Sec. 6.4.

transition.

6.2 SuperWIMP

Let us discuss how the number density of exotic colored particles can change the predictions of the relic abundance of superWIMP. The superWIMP framework in consideration has two sources contributing to the relic abundance of superWIMP: thermal production of superWIMP, where the superWIMP is produced via interactions in the thermal bath, and the decay of frozen out relic colored particles into superWIMPs. Including bound-state effects allows us to study the the latter contribution more precisely. As an example, we consider the case where the right-handed stop is the NLSP and the KSVZ axino is the superWIMP [181, 182].

Axino is thermally produced via QCD interactions in the early universe. The relic abundance depends on the reheating temperature, T_R as follows [183, 184]

$$\Omega_{\tilde{a}}^{(th)}h^2 \simeq 1.5 g_s^6 \ln\left(\frac{3}{g_s}\right)\left(\frac{m_{\tilde{a}}}{600\,\mathrm{GeV}}\right)\left(\frac{T_R}{10^6\,\mathrm{GeV}}\right)\left(\frac{f_a}{10^{14}\,\mathrm{GeV}}\right)^{-2}, \tag{6.2}$$

where f_a is the axion decay constant, and g_s is to be evaluated at the T_R scale.

As the decay rate of the stop NLSP is suppressed by f_a, its decay occurs after freeze-out. The contribution of the stop NLSP to the relic abundance of axino can be related to the would-be relic abundance of stop as follows:

$$\Omega_{\tilde{a}}^{(\tilde{t}_R)}h^2 = \frac{m_{\tilde{a}}}{m_{\tilde{t}_R}}\Omega_{\tilde{t}_R}h^2. \tag{6.3}$$

We parametrize the yield of stop as follows:

$$Y_{\tilde{t}_R} \simeq 3.54\times 10^{-14}\left(\frac{m_{\tilde{t}_R}}{10^3\,\mathrm{GeV}}\right)^{1.25}. \tag{6.4}$$

Using $\Omega_{\tilde{t}_R}h^2 \simeq 2.76\times 10^{11} Y_{\tilde{t}_R}(m_{\tilde{t}_R}/10^3\mathrm{GeV})$, we get

$$\Omega_{\tilde{a}}^{(\tilde{t}_R)}h^2 \simeq 0.1\left(\frac{m_{\tilde{a}}}{600\,\mathrm{GeV}}\right)\left(\frac{m_{\tilde{t}_R}}{10^4\,\mathrm{GeV}}\right)^{1.25}. \tag{6.5}$$

Hence, a multi-TeV stop can reproduce the observed DM relic abundance, assuming that the axino is also of TeV-scale. On the other hand, the reheating temperature must be lower than around $1.4\times 10^5\,\mathrm{GeV}$ for $f_a = 10^{14}\,\mathrm{GeV}$ so that axino is not overproduced. Such a limit on T_R may impose constraints on high-scale models of baryogenesis or leptogenesis.

Note that the decay rate of stop is given as [185]

$$\Gamma(\tilde{t}_R \to t\tilde{a}) = (1.3\times 10^{-3}\,\mathrm{sec})^{-1}\xi_t^2\left(\frac{m_{\tilde{t}_R}}{10^4\,\mathrm{GeV}}\right)\left(\frac{m_{\tilde{g}}}{10^4\,\mathrm{GeV}}\right)^2\left(\frac{10^{14}\,\mathrm{GeV}}{f_a}\right)^2\left(1-\frac{m_{\tilde{a}}^2}{m_{\tilde{t}_R}^2}\right), \tag{6.6}$$

where ξ_t is a factor of order one. Therefore, within the parameter space of interest, the decay of stop does not affect BBN.

6.3 Coannihilation

Let us now study scenarios in which the WIMP DM χ has a mass close to a certain massive colored particle X, such that $\chi - X$ coannihilation is important in determining the DM relic abundance. We assume that the DM has a number of degrees of freedom $g_\chi = 2$, corresponding to a Majorana (e.g., the neutralino in SUSY) or a complex scalar DM. The relic abundance of DM then depends only on the DM mass, m_χ, and the mass splitting between DM and the colored particle, $m_X - m_\chi$. We plot in Fig. 6.3 in the $(m_\chi, m_X - m_\chi)$ planes the contour bands of the dark matter relic abundance falling within the 3-σ range of the Planck determination of the cold DM density, $\Omega_{\rm CDM}h^2 = 0.1193 \pm 0.0014$ [29]. These bands are calculated using Eq. (5.47) without the Sommerfeld and bound-state effects (red), with the Sommerfeld effect but without bound-state effect (orange), with both the Sommerfeld and bound-state effect (black), and with Sommerfeld effect and a factor of 2 enlargement of the bound-state effect (purple). We can see that for the S3, S8 and F8 cases, on top of the Sommerfeld enhancement, bound-state effect further push upwards the largest mass splittings which can result in correct DM relic density. Also, the largest possible DM masses achieved at the endpoints of the coannihilation strips when the mass splittings approach zero, increase by $\sim 50\%, 100\%$ and 30% with respect to the Sommerfeld-enhanced-only values, reaching $\sim 2.5, 11$ and 9 TeV for the S3, S8 and F8 cases, respectively [1]. For the F3 case in the upper right panel, however, the Sommerfeld and bound-state effects are much smaller compared to the other three cases. As can be seen from the positions of the red and orange bands, the Sommerfeld effect gives a slightly suppressed rather than an enhanced $\langle \sigma_{eff} v \rangle$ [2].

Fig. 6.4 shows in the $(m_\chi, \Omega_\chi h^2)$ plans the locations of the endpoints of the coannihilation strips for different values of $\Omega_\chi h^2$, achieved when $m_X - m_\chi = 0$, for S3 (upper left), F3 (upper right), S8 (lower left) and F8 (lower right) coannihilating with a WIMP DM which has $g_\chi = 2$. The color conversions are the same as in Fig. 6.3. The horizontal green band shows the 3-σ range determined by Planck, $0.1151 < \Omega_\chi h^2 < 0.1235$. We can see that for the S3, S8 and F8 cases, for a given value of m_χ the Sommerfeld effect greatly reduces the calculated $\Omega_\chi h^2$ compared to the one without the inclusion of Sommerfeld factors. Also, the calculated $\Omega_\chi h^2$ is further significantly reduced after including the bound-state effect, in particular for a DM mass of TeV scale or larger. On the other hand, for the F3 case, again we see that the Sommerfeld and bound-state effects are

[1] The numerical differences for the F8 case in Figs. 6.3 and 6.4 compared to Figs. 4 and 5 in [121] are due to a different use of α_s in the bound-state formation and dissociation cross sections, as well as the effect from the squark masses in the tree-level cross section of gluino pair annihilation into quark-antiquark pairs.

[2] The red and orange bands and curves in Figs. 6.3 and 6.4 are consistent with the red and light green bands and curves in Figs. 1 and 2 in [145] for the S3, S8 and F8 cases. For the F3 case, the red band and curve presented here are also consistent with the ones in [145], but the orange band and curve are different.

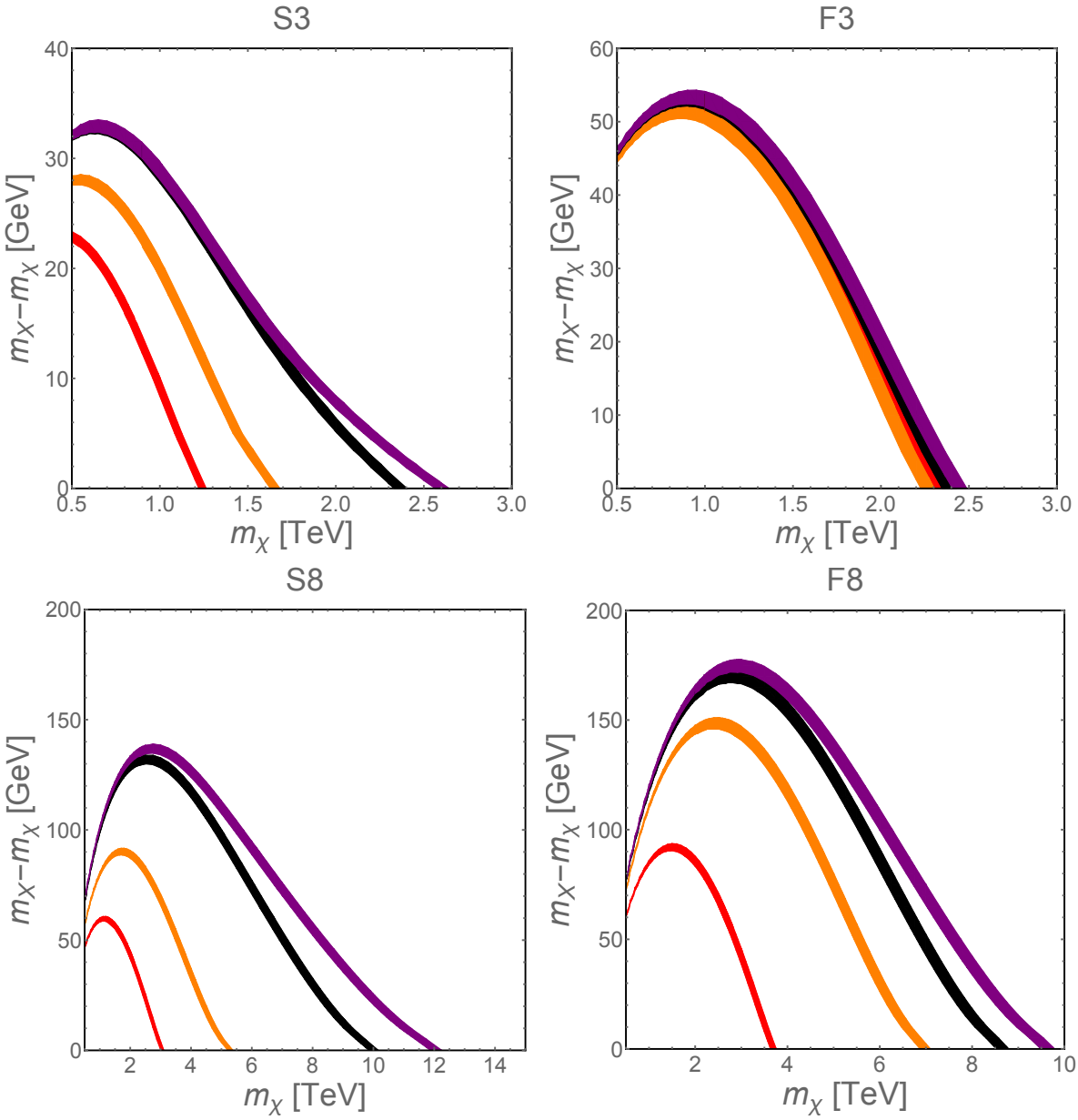

Figure 6.3: The $(m_\chi, m_X - m_\chi)$ planes showing bands where $0.1151 < \Omega_\chi h^2 < 0.1235$ (3-σ range of the Planck determination of the cold DM relic density), for S3 (upper left), F3 (upper right), S8 (lower left) and F8 (lower right) coannihilating with a DM which has the number of degrees of freedom $g_\chi = 2$. These results are calculated without the Sommerfeld and bound-state effects (red), with the Sommerfeld effect but without bound-state effect (orange), with both the Sommerfeld and bound-state effect (black), and with Sommerfeld effect and a factor of 2 enlargement of the bound-state effect (purple).

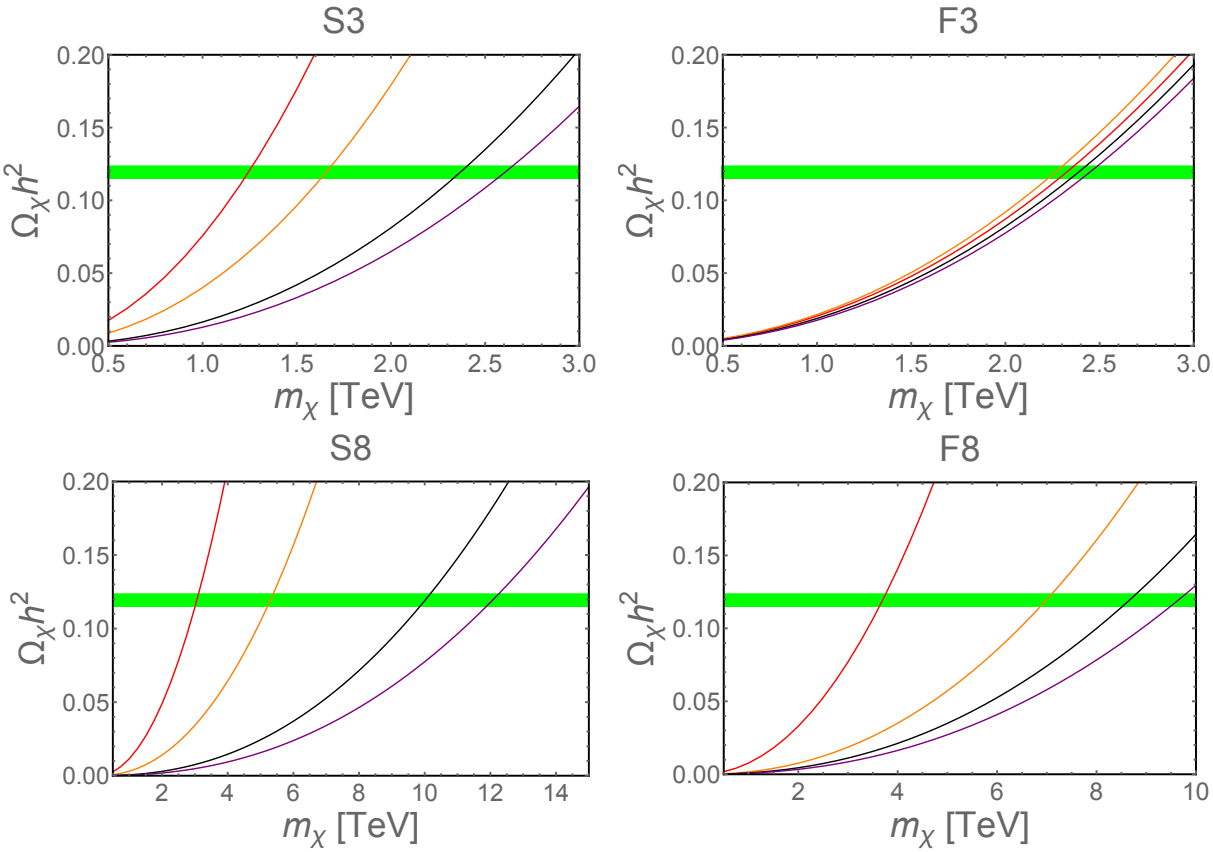

Figure 6.4: The locations of the endpoints (i.e., $m_X - m_\chi = 0$) of the coannihilation strips for different values of $\Omega_\chi h^2$, using the same color conventions as in Fig. 6.3 for S3 (upper left), F3 (upper right), S8 (lower left) and F8 (lower right), respectively. The 3-σ range $0.1151 < \Omega_\chi h^2 < 0.1235$ is shown by the horizontal green band.

small, and the Sommerfeld effect is opposite compared to the other three cases.

6.4 Collider constraints

As shown in the previous Section, the DM relic abundance in the WIMP DM coannihilation scenarios and the BBN constraints on the long-lived massive particle decays impose upper bounds on the masses of exotic massive colored particles. On the other hand, collider experiments are constraining the masses from below. It should be emphasized that it is impossible to probed the WIMP DM coannihilation scenarios using techniques of DM direct/indirect detection experiments as reviewed in Chapter 2. Collider search for the colored particles is the only alternative strategy (which is interesting and important

from the minimalist's point of view).

In the massive colored particle coannihilating with a WIMP DM scenario, the coannihilation region is characterized by a small mass splitting, which typically is difficult to probe at the LHC using the conventional multiple jets plus large missing energy searches. Massive colored particle pair production accompanied by a hard initial-state radiation, i.e., the monojet search, is utilized to constrain scenarios with such a compressed mass spectrum. For simplicity, we focus only on the $m_X - m_\chi \to 0$ region so that the kinematics of decay products of the colored particles can be ignored [3]. The 13 TeV lower mass limits for S3 (stop) and F8 (gluino) are 0.32 TeV [186] and 0.63 TeV [187], respectively. To impose limits on F3 and S8, we simulate the monojet analysis [188, 189] using the `MadGraph-Pythia-Checkmate` [190–197] pipeline: parton events $pp \to \chi\chi j$, where j is a jet, are generated using `MadGraph`; partons are showered and hadronized using `Pythia`; detector responses to the events are simulated with `Delphes`; cuts on the events are applied with the help of `Checkmate`. In particular, we utilize the Run 2 SUSY search for squarks and gluino to place monojet limits on F3 and S8 [188]. The relevant signal region is SR2jm and has kinematic cuts as follows:

- $p_T^{j_1} > 300$ GeV
- $p_T^{j_2} > 50$ GeV
- $\not{E}_T > 200$ GeV
- $\Delta\phi(j, \not{E}_T) > 0.4$ up to three leading jets in the events
- no leptons with $p_T > 10$ GeV
- $\not{E}_T/\sqrt{H_T} > 15$ GeV$^{1/2}$
- $m_{\rm eff} > 1600$ GeV

where p_T is the jet transverse momentum, $\not{E}_T$ is the missing transverse energy, H_T is the scalar sum of jet p_T's, and $m_{\rm eff}$ is defined as the sum of H_T and $\not{E}_T$. The obtained mass limits are 0.41 TeV and 0.43 TeV for F3 and S8, respectively. The results are summarized in Table 6.1, together with the endpoint values for the coannihilation strips including the Sommerfeld and bound-state effects read from Fig. 6.3.

Let us briefly comment on the discovery reach of a prospective 100 TeV proton-proton collider at an integrated luminosity of 3000 fb^{-1}, in particular for the S3 case.

[3] Opening the mass splitting $m_X - m_\chi$ will lower the monojet sensitivity as the missing energy is reduced by additional jets or objects from the decays of the massive colored particles. On the other hand, the signal efficiency of multi-jet plus missing energy searches is increased as the mass splitting opens, albeit the efficiency depends on how the colored particle decays. It is interesting to study how these complementary approaches can probe the coannihilation region. The detailed study is left for future work.

Bounds (TeV)	S3	F3	S8	F8
DM	2.5	2.4	11	9
LHC	0.32	0.41	0.63	0.43

Table 6.1: The DM masses at the endpoints of the coannihilation scripts including the Sommerfeld and bound-state effects and giving the observed DM relic abundance, and the LHC monojet bounds for these coannihilation scenarios.

The bound-state effect increases the mass range of DM significantly, making the coannihilation scenario more difficult to probe. With the inclusion of the bound-state effect so that the right-handed stop-Bino coannihilation strip ends at ~ 2.5 TeV when the Bino accounts for the total DM density (the inclusion of additional electroweak coannihilation channels [132] and a large lighter stop - heavier stop - Higgs coupling to heavier stop mass ratio [130] can shift the endpoint to even larger values), the ending part of the strip may be not within the discovery reach any more, though may be still within the exclusion reach given sufficiently low systematics [198].

In the long-lived massive colored particle scenario, the produced massive colored particles at a collider form R-hadrons and travel through the detector with velocities significantly less than the speed of light, leaving ionization energy dE/dx characteristically higher than that of charged SM particles. Searches for such events have been performed by both ATLAS and CMS collaborations at the LHC [199, 200]. The current 13 TeV limits on long-lived (stable at collider scales) S3 (stop) and F8 (gluino) are 890 GeV and 1580 GeV, respectively [201]. While a dedicated simulation of R-hadron events at the LHC is beyond the scope of this work, in order to make a simple estimate of the bounds on long-lived F3 and S8, we assume that the signal efficiency and hadron formation probability of F3 (S8) equal to that of S3 (F8). The pair production cross section of F3 is estimated up to NNLO using `Hathor` [202], while an NLO K-factor of 2 is used for the S8 scenario [203]. The obtained mass limits are 1170 GeV and 1420 GeV for F3 and S8, respectively. The results are summarized in Table 6.2, together with the upper bounds from BBN for the masses of long-lived massive colored particles assuming lifetimes between 0.1 and 100 sec, including the Sommerfeld and bound-state effects, as discussed previously.

6.5 Electric charge corrections

So far we have focused on bound-state effects with a gluon being emitted/absorbed in the bound-state formation/dissociation process. If a massive colored particle also carries some electric charge, for example, the squark in SUSY, a bound state can form (or be dissociated) by emitting (or absorbing) a photon, i.e., $X_1 X_2 \leftrightarrow \eta\gamma$. In addition, the

Bounds (TeV)	S3	F3	S8	F8
BBN	2.1	1.7	17	11
LHC	0.89	1.2	1.6	1.4

Table 6.2: BBN upper bounds on the masses of long-lived massive colored particles assuming lifetimes between 0.1 and 100 sec, including the Sommerfeld and bound-state effects. Also shown are the LHC lower bounds on the masses of long-lived colored particles.

previously calculated bound-state formation/dissociation cross sections associated with gluon emission/absorption are modified due to the change of the potentials between the massive colored particles. To see the impacts of the electric charge on the bound-state effect, we use the S3 case as an example by assigning a charge Q ($-Q$) to $S3$ ($\overline{S3}$), and consider the processes $S3\overline{S3} \leftrightarrow \eta g$ and $S3\overline{S3} \leftrightarrow \eta\gamma$.

For $S3\overline{S3} \leftrightarrow \eta g$, we still consider the transition between the (color-octet, $L = 1, S = 0$) free pair state and the (color-singlet, $L = 0, S = 0$) bound state. By modifying the coefficients of the Coulomb potentials, $\zeta \to \zeta + \alpha_{\rm EM} Q^2$ and $\zeta' \to \zeta' + \alpha_{\rm EM} Q^2$, where $\alpha_{\rm EM}$ is the electromagnetic fine structure constant, the formulae given in the previous sections still apply. Quantities depending on ζ and/or ζ', e.g., a, E_B, κ, and the cross sections and rates into which they enter, therefore all change. With an electric charge, for the bound state the previous attractive potential becomes more attractive. On the other hand, for the free pair state the previous repulsive potential becomes less repulsive, and even it can become attractive when $|Q|$ is large enough, i.e., $(-1/6)\alpha_s + \alpha_{\rm EM} Q^2$ is positive when $|Q| \gtrsim 3/2$. The bound-state annihilation decay rate changes as well due to the change of ζ.

For $S3\overline{S3} \leftrightarrow \eta\gamma$, the bound state and the free pair state are in the same color state, so that $\zeta = \zeta'$. Using dipole approximation [4], we consider the transition between the (color-singlet, $L = 1, S = 0$) free pair state and the (color-singlet, $L = 0, S = 0$) bound state. The calculation is the same as for $S3\overline{S3} \leftrightarrow \eta g$, except that there is no color factors to worry about and the explicit coupling factor α_s in Eq. (5.11) is changed to $\alpha_{\rm EM} Q^2$. The bound-state dissociation and formation cross sections are

$$\sigma^{\gamma}_{dis} = \frac{2^9 \pi^2}{3} \alpha_{\rm EM} Q^2 a^2 \left(\frac{E_B}{\omega}\right)^4 \frac{e^{-4\nu \,\mathrm{arccot}\, \nu}}{1 - e^{-2\pi\nu}} , \tag{6.7}$$

$$\sigma^{\gamma}_{bsf} = \frac{1 \times 2}{3 \times 3} \frac{\omega^2}{(\mu v_{rel})^2} \times \sigma^{\gamma}_{dis} , \tag{6.8}$$

where the superscript "γ" indicates photon emission/absorption. The quantities a, E_B etc. are evaluated taking into account the change of potential due to the electric charge

[4] We have checked that the dipole approximation is still justified with the inclusion of the electric charges we consider.

as mentioned above. In the thermally-averaged dissociation rate given in Eq. (5.35), g_g is changed to $g_\gamma = 2$. The formula for the thermally-averaged formation cross section times relative velocity given in Eq. (5.36) stays the same.

We show in Fig. 6.5 the impacts of electric charge on the bound-state effect for the S3 case. The red dashed, red dotted, blue dashed, blue dotted and brown dashed lines correspond to cases of $|Q| = 1/3, 2/3, 1, 2$ and 3, respectively. The grey dashed lines in the upper left, upper right and lower left panels are for the case with the electric charge chosen such that $\zeta' = 0$. The black lines in the upper left and lower left panels are the same as the one in the left panel of Fig. 5.1, and the black line in the lower right panel is the same as the one in the upper left panel of Fig. 6.4, all for $Q = 0$. We use $\alpha_{\rm EM} = 1/128$ in these plots, and take values of α_s's as noted before in Sec. 5.6. The upper left panel shows the the ratio

$$\frac{\langle\sigma v\rangle^g_{bsf}\,\frac{\langle\Gamma\rangle_\eta}{\langle\Gamma\rangle_\eta+\langle\Gamma\rangle^g_{dis}}}{\langle\sigma v_{rel}(XX\to gg,q\bar{q})\rangle_{\text{w/o Sommerfeld}}}\,, \tag{6.9}$$

where the superscript "g" indicates that only $S3\overline{S3} \leftrightarrow \eta g$ is considered. We can see that larger $|Q|$ makes the bound-state effect stronger. Also, for a large enough $|Q|$ such that the free pair potential becomes attractive (the blue dotted line and especially the brown dashed line), the behavior of the ratio at large E_B/T becomes more like the black line of Fig. 5.2 where the free pair potential is attractive. The upper right panel shows the ratio

$$\frac{\langle\sigma v\rangle^\gamma_{bsf}\,\frac{\langle\Gamma\rangle_\eta}{\langle\Gamma\rangle_\eta+\langle\Gamma\rangle^\gamma_{dis}}}{\langle\sigma v_{rel}(XX\to gg,q\bar{q})\rangle_{\text{w/o Sommerfeld}}}\,. \tag{6.10}$$

Again, larger $|Q|$ leads to larger bound-state effect with photon emission/absorption. By comparing with the corresponding lines in the upper right panel, we see that for $|Q| > 2$, at $E_B/T \lesssim 10$ the bound-state effect due to gluon emission/absorption is much larger than the one due to photon emission/absorption, while they become comparable for larger $|Q|$. The lower left panel shows the ratio

$$\frac{\left(\langle\sigma v\rangle^g_{bsf}+\langle\sigma v\rangle^\gamma_{bsf}\right)\frac{\langle\Gamma\rangle_\eta}{\langle\Gamma\rangle_\eta+\langle\Gamma\rangle^g_{dis}+\langle\Gamma\rangle^\gamma_{dis}}}{\langle\sigma v_{rel}(XX\to gg,q\bar{q})\rangle_{\text{w/o Sommerfeld}}}\,, \tag{6.11}$$

in which the numerator is the one entering into the Boltzmann equation as the second term in Eq. (5.49). The shape of curves at smaller E_B/T is controlled by the gluon emission/absorption bound-state effect, while the one from photon emission/absorption becomes important at larger E_B/T.

We plot in the lower right panel the locations of the endpoints of the coannihilation strips for different values of $\Omega_\chi h^2$, after taking into account the total impacts of electric charge on the bound-state effects. As before, the horizontal green band shows the 3-σ range of the Planck determination of the cold DM relic density, $0.1151 < \Omega_\chi h^2 < 0.1235$,

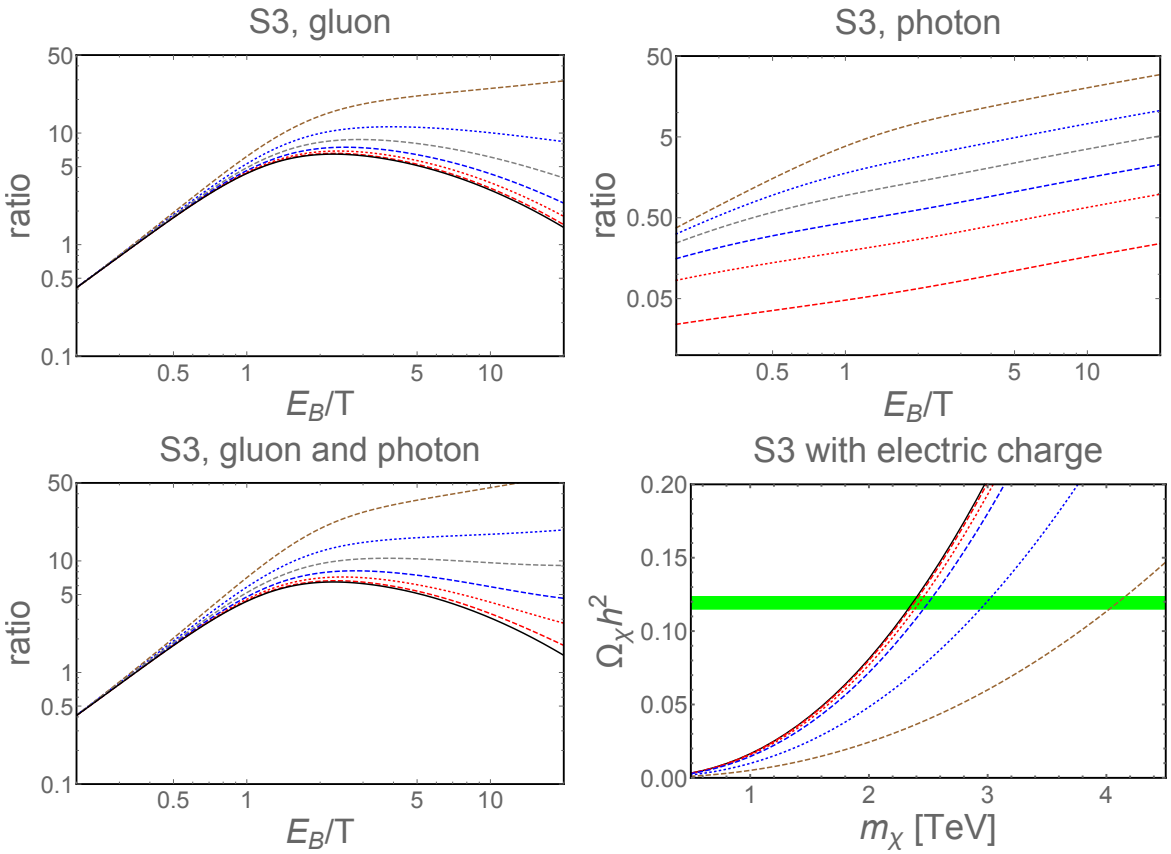

Figure 6.5: Impacts of the electric charge on the bound-state effect for the S3 case. The upper left panel is for the gluon emission/absorption bound-state effect, corresponding to Eq. (6.9). The upper right panel is for the photon emission/absorption bound-state effect, corresponding to Eq. (6.10). The lower left panel takes both of the above two into account, corresponding to Eq. (6.11). The lower right panel shows the locations of the endpoints (i.e., $m_X - m_\chi = 0$) of the coannihilation strips for different values of $\Omega_\chi h^2$, for a WIMP DM with the number of degrees of freedom $g_\chi = 2$. The 3-σ range $0.1151 < \Omega_\chi h^2 < 0.1235$ of the Planck determination of the cold DM relic density is shown by a horizontal green band. In all panels, the red dashed, red dotted, blue dashed, blue dotted and brown dashed lines correspond to cases of $|Q| = 1/3, 2/3, 1, 2$ and 3, respectively. The grey dashed lines in the upper left, upper right and lower left panels are for the case with the Q chosen such that the potential for the free pair is zero. The black lines in the upper left, lower left and lower right panels are for the case of $Q = 0$.

and we assume a WIMP DM with the number of degrees of freedom $g_\chi = 2$. Comparing to the black line which corresponds to $Q = 0$, the $|Q| = 1/3$ and $2/3$ cases (corresponding to the charges of squarks) only slightly increase the endpoint values of m_χ for a given $\Omega_\chi h^2$, and by $\sim \mathcal{O}(10)$ GeV on the Planck band. For larger $|Q|$, the increase becomes significant, and the endpoint on the Planck band reaches ~ 3 (4) TeV for $|Q| = 2$ (3).

Chapter 7

Discussions and Conclusions

After giving an review on DM, we have in this thesis studied the bound-state effects of exotic massive colored particles on DM relic abundance calculations in scenarios where the massive colored particles coannihilating with a WIMP DM. In general the bound-state effect increases the effective annihilation cross section through the formation and then annihilation decays of bound states, draining the number of DM particles in the thermal bath, when the massive colored particles and DM share the same discrete symmetry which stabilizes the latter, and provided the interconversion rate between the two particle species is fast enough compared to the Hubble expansion rate. For a given DM relic abundance, this effect allows a larger DM mass and a larger mass splitting between the massive colored particle and the DM. As examples, we consider the massive colored particles being complex scalars (S3) or Dirac fermions (F3) in the color SU(3) fundamental representation, and real scalars (S8) or Majorana fermions (F8) in the adjoint representation. We find that the bound-state effect significantly increases the largest possible DM masses which can give the observed DM relic abundance, reaching $\sim 2.5, 11$ and 9 TeV for the S3, S8 and F8 cases, resepectively. Comparing to the corresponding ones when considering only the Sommerfeld effect but without the bound-state effect, these values increase by $\sim 50\%, 100\%$ and 30%, respectively. The increase for the F3 case is smaller, but still the bound-state effect can more than counterbalance the Sommerfeld effect which is a suppression rather than an enhancement in this case.

We note that while the potentials for the bound states are attractive, due to color charge conservation the potential for an incoming massive colored particle pair can be attractive, zero or repulsive. In the early Universe bound states can form when incoming pairs have sufficiently large relative velocities to overcome the repulsive potential. In particular, for the S3 case, we find that although fading at low temperatures, the large bound-state formation cross section achieved when temperatures are comparable to the bound-state binding energy makes the bound-state effect significant enough, such that to probe the entire stop-Bino coannihilation strip can be quite challenging, if possible,

even in a prospective 100 TeV proton-proton collider at an integrated luminosity of 3000 fb^{-1}.

We have also calculated the corrections for the bound-state effect when the massive colored particles carry electric charges. Using the S3 case as an example, we find that larger electric charge makes the bound-state effect stronger, and the enhancement can make the above mentioned ~ 2.5 TeV coannihilation endpoint to ~ 3 (4) TeV for $|Q| = 2$ (3), for which the incoming pair potential changes from being repulsive to attractive. However, for $|Q| < 1$, the enhancement is quite small.

As we have briefly discussed, bound-state effects should also be included in calculations of superWIMP DM relic density from the decays of metastable massive colored particles, as well as when applying BBN constraints on long-lived massive colored particles. Furthermore, considering that BBN constraints and the DM relic abundance in coannihilation scenarios impose upper bounds on the masses of massive colored particles, we have studied the collider limits on the exotic massive colored particles we consider in this thesis.

Let us note that many other QCD bound states are possible. For example, in SUSY there can be di-squark and squark-gluino bound states [204]. Also, a squark and an antisquark with different flavors can also form a bound state. Studying the effects of these bound states in specific SUSY models are left for future works.

Bibliography

[1] G. Aad *et al.* (ATLAS), Phys. Lett. **B716**, 1 (2012), arXiv:1207.7214 [hep-ex].

[2] S. Chatrchyan *et al.* (CMS), Phys. Lett. **B716**, 30 (2012), arXiv:1207.7235 [hep-ex].

[3] S. P. Liew and F. Luo, (2016), arXiv:1611.08133 [hep-ph].

[4] J. C. Kapteyn, Astrophysical Journal **55**, 302 (1922).

[5] J. H. Oort, Bulletin of the Astronomical Institutes of the Netherlands **6**, 249 (1932).

[6] F. Zwicky, Helv. Phys. Acta **6**, 110 (1933).

[7] S. Smith, Astrophysical Journal **83**, 23 (1936).

[8] F. D. Kahn and L. Woltjer, Astrophysical Journal **130**, 705 (1959).

[9] D. B. Cline, ed., *Sources of Dark Matter in the Universe: Proceedings, 1st International Symposium, February 16-18, 1994, Bel Air, CA*, World Scientific (World Scientific, Singapore, 1995).

[10] V. C. Rubin and W. K. Ford, Jr., Astrophys. J. **159**, 379 (1970).

[11] M. Roberts and R. Whitehurst, Astrophysical Journal **201**, 327 (1975).

[12] J. Ostriker and P. Peebles, Astrophysical Journal **186**, 467 (1973).

[13] K. A. Einasto, J. and E. Saar, Nature **250**, 309 (1974).

[14] J. P. Ostriker, P. J. E. Peebles, and A. Yahil, Astrophys. J. **193**, L1 (1974).

[15] R. Cowsik and J. McClelland, Astrophys. J. **180**, 7 (1973).

[16] Ya. B. Zeldovich, J. Einasto, and S. F. Shandarin, Nature **300**, 407 (1982).

[17] H. Pagels and J. R. Primack, Phys. Rev. Lett. **48**, 223 (1982).

[18] G. R. Blumenthal, H. Pagels, and J. R. Primack, Nature **299**, 37 (1982).

[19] J. R. Ellis, J. S. Hagelin, D. V. Nanopoulos, K. A. Olive, and M. Srednicki, *IN *BATAVIA 1984, PROCEEDINGS, INNER SPACE/OUTER SPACE*, 458-459., In *Srednicki, M.A. (ed.): Particle physics and cosmology* 223-246*, Nucl. Phys. **B238**, 453 (1984).

[20] E. W. Kolb and M. S. Turner, Front. Phys. **69**, 1 (1990).

[21] S. Weinberg, *Cosmology* (2008).

[22] A. G. Riess *et al.* (Supernova Search Team), Astron. J. **116**, 1009 (1998), arXiv:astro-ph/9805201 [astro-ph].

[23] S. Perlmutter *et al.* (Supernova Cosmology Project), Astrophys. J. **517**, 565 (1999), arXiv:astro-ph/9812133 [astro-ph].

[24] K. G. Begeman, A. H. Broeils, and R. H. Sanders, Mon. Not. Roy. Astron. Soc. **249**, 523 (1991).

[25] G. Bertone, D. Hooper, and J. Silk, Phys. Rept. **405**, 279 (2005), arXiv:hep-ph/0404175 [hep-ph].

[26] D. Clowe, M. Bradac, A. H. Gonzalez, M. Markevitch, S. W. Randall, C. Jones, and D. Zaritsky, Astrophys. J. **648**, L109 (2006), arXiv:astro-ph/0608407 [astro-ph].

[27] W. T. Hu, *Wandering in the Background: A CMB Explorer*, Ph.D. thesis, UC, Berkeley (1995), arXiv:astro-ph/9508126 [astro-ph].

[28] P. A. R. Ade *et al.* (Planck), Astron. Astrophys. **571**, A16 (2014), arXiv:1303.5076 [astro-ph.CO].

[29] P. A. R. Ade *et al.* (Planck), Astron. Astrophys. **594**, A13 (2016), arXiv:1502.01589 [astro-ph.CO].

[30] B. Fields and S. Sarkar, (2006), arXiv:astro-ph/0601514 [astro-ph].

[31] M. Betoule *et al.* (SDSS), Astron. Astrophys. **568**, A22 (2014), arXiv:1401.4064 [astro-ph.CO].

[32] K. Freese, B. Fields, and D. Graff, Nucl. Phys. Proc. Suppl. **80**, 0305 (2000), arXiv:astro-ph/9904401 [astro-ph].

[33] P. Kroupa, B. Famaey, K. S. de Boer, J. Dabringhausen, M. S. Pawlowski, C. M. Boily, H. Jerjen, D. Forbes, G. Hensler, and M. Metz, Astron. Astrophys. **523**, A32 (2010), arXiv:1006.1647 [astro-ph.CO].

[34] S. W. Randall, M. Markevitch, D. Clowe, A. H. Gonzalez, and M. Bradac, Astrophys. J. **679**, 1173 (2008), arXiv:0704.0261 [astro-ph].

[35] H.-W. Rix and G. Lake, Astrophys. J. **417**, L1 (1993), arXiv:astro-ph/9308022 [astro-ph].

[36] G. Jungman, M. Kamionkowski, and K. Griest, Phys. Rept. **267**, 195 (1996), arXiv:hep-ph/9506380 [hep-ph].

[37] D. G. Cerdeno and A. M. Green, (2010), arXiv:1002.1912 [astro-ph.CO].

[38] R. W. Schnee, in *In Physics of the Large and Small: Proceedings of the 2009 Theoretical Advanced Study Institute in Elementary Particle Physics, 629-681 (World Scientific, Singapore) Ed. Csaba Csaki and Scott Dodelson (2010)* (2011) arXiv:1101.5205 [astro-ph.CO].

[39] E. Aprile *et al.* (XENON100), Phys. Rev. Lett. **109**, 181301 (2012), arXiv:1207.5988 [astro-ph.CO].

[40] D. S. Akerib *et al.*, (2016), arXiv:1608.07648 [astro-ph.CO].

[41] R. Agnese *et al.* (SuperCDMS), Phys. Rev. Lett. **116**, 071301 (2016), arXiv:1509.02448 [astro-ph.CO].

[42] R. H. Helm, Phys. Rev. **104**, 1466 (1956).

[43] J. R. Ellis, K. A. Olive, and C. Savage, Phys. Rev. **D77**, 065026 (2008), arXiv:0801.3656 [hep-ph].

[44] X. L. Ren, L. S. Geng, J. Martin Camalich, J. Meng, and H. Toki, JHEP **12**, 073 (2012), arXiv:1209.3641 [nucl-th].

[45] P. Schweitzer, Eur. Phys. J. **A22**, 89 (2004), arXiv:hep-ph/0312376 [hep-ph].

[46] P. Junnarkar and A. Walker-Loud, Phys. Rev. **D87**, 114510 (2013), arXiv:1301.1114 [hep-lat].

[47] R. Ruiz de Austri and C. Prez de los Heros, JCAP **1311**, 049 (2013), arXiv:1307.6668 [hep-ph].

[48] M. I. Gresham and K. M. Zurek, Phys. Rev. **D89**, 016017 (2014), arXiv:1311.2082 [hep-ph].

[49] R. Bernabei *et al.* (DAMA, LIBRA), Eur. Phys. J. **C67**, 39 (2010), arXiv:1002.1028 [astro-ph.GA].

[50] C. E. Aalseth *et al.* (CoGeNT), Phys. Rev. Lett. **106**, 131301 (2011), arXiv:1002.4703 [astro-ph.CO].

[51] C. E. Aalseth *et al.*, Phys. Rev. Lett. **107**, 141301 (2011), arXiv:1106.0650 [astro-ph.CO].

[52] G. Angloher *et al.*, Eur. Phys. J. **C72**, 1971 (2012), arXiv:1109.0702 [astro-ph.CO].

[53] R. Agnese *et al.* (CDMS), Phys. Rev. Lett. **111**, 251301 (2013), arXiv:1304.4279 [hep-ex].

[54] D. S. Akerib *et al.* (LUX), Phys. Rev. Lett. **112**, 091303 (2014), arXiv:1310.8214 [astro-ph.CO].

[55] M. Ackermann *et al.* (Fermi-LAT), Phys. Rev. Lett. **115**, 231301 (2015), arXiv:1503.02641 [astro-ph.HE].

[56] D. Hooper and L. Goodenough, Phys. Lett. **B697**, 412 (2011), arXiv:1010.2752 [hep-ph].

[57] D. Hooper and T. Linden, Phys. Rev. **D84**, 123005 (2011), arXiv:1110.0006 [astro-ph.HE].

[58] D. P. Finkbeiner, (2004), arXiv:astro-ph/0409027 [astro-ph].

[59] T. Linden, D. Hooper, and F. Yusef-Zadeh, Astrophys. J. **741**, 95 (2011), arXiv:1106.5493 [astro-ph.HE].

[60] D. Hooper, Phys. Dark Univ. **1**, 1 (2012), arXiv:1201.1303 [astro-ph.CO].

[61] T. Bringmann, X. Huang, A. Ibarra, S. Vogl, and C. Weniger, JCAP **1207**, 054 (2012), arXiv:1203.1312 [hep-ph].

[62] C. Weniger, JCAP **1208**, 007 (2012), arXiv:1204.2797 [hep-ph].

[63] M. Endo, K. Hamaguchi, S. P. Liew, K. Mukaida, and K. Nakayama, Phys. Lett. **B721**, 111 (2013), arXiv:1301.7536 [hep-ph].

[64] S. P. Liew, Phys. Lett. **B724**, 88 (2013), arXiv:1304.1992 [hep-ph].

[65] J. Knodlseder *et al.*, Astron. Astrophys. **411**, L457 (2003), arXiv:astro-ph/0309442 [astro-ph].

[66] P. Jean *et al.*, Astron. Astrophys. **407**, L55 (2003), arXiv:astro-ph/0309484 [astro-ph].

[67] C. Boehm, D. Hooper, J. Silk, M. Casse, and J. Paul, Phys. Rev. Lett. **92**, 101301 (2004), arXiv:astro-ph/0309686 [astro-ph].

[68] D. P. Finkbeiner and N. Weiner, Phys. Rev. **D76**, 083519 (2007), arXiv:astro-ph/0702587 [astro-ph].

[69] E. Bulbul, M. Markevitch, A. Foster, R. K. Smith, M. Loewenstein, and S. W. Randall, Astrophys. J. **789**, 13 (2014), arXiv:1402.2301 [astro-ph.CO].

[70] A. Boyarsky, O. Ruchayskiy, D. Iakubovskyi, and J. Franse, Phys. Rev. Lett. **113**, 251301 (2014), arXiv:1402.4119 [astro-ph.CO].

[71] S. P. Liew, JCAP **1405**, 044 (2014), arXiv:1403.6621 [hep-ph].

[72] E. Resconi (IceCube), *Very large volume neutrino telescope for the Mediterranean Sea. Proceedings, 3rd International VLVnuT Workshop, Toulon, France, April 22-24, 2008*, Nucl. Instrum. Meth. **A602**, 7 (2009), arXiv:0807.3891 [astro-ph].

[73] S. Profumo, in *Proceedings, Theoretical Advanced Study Institute in Elementary Particle Physics: Searching for New Physics at Small and Large Scales (TASI 2012): Boulder, Colorado, June 4-29, 2012* (2013) pp. 143–189, arXiv:1301.0952 [hep-ph].

[74] M. G. Aartsen *et al.* (IceCube), Phys. Rev. Lett. **113**, 101101 (2014), arXiv:1405.5303 [astro-ph.HE].

[75] B. Feldstein, A. Kusenko, S. Matsumoto, and T. T. Yanagida, Phys. Rev. **D88**, 015004 (2013), arXiv:1303.7320 [hep-ph].

[76] A. Esmaili and P. D. Serpico, JCAP **1311**, 054 (2013), arXiv:1308.1105 [hep-ph].

[77] O. Adriani *et al.* (PAMELA), Phys. Rev. Lett. **105**, 121101 (2010), arXiv:1007.0821 [astro-ph.HE].

[78] M. Aguilar *et al.* (AMS), Phys. Rev. Lett. **117**, 091103 (2016).

[79] O. Adriani *et al.* (PAMELA), Nature **458**, 607 (2009), arXiv:0810.4995 [astro-ph].

[80] M. Aguilar *et al.* (AMS), Phys. Rev. Lett. **110**, 141102 (2013).

[81] L. Bergstrom, T. Bringmann, I. Cholis, D. Hooper, and C. Weniger, Phys. Rev. Lett. **111**, 171101 (2013), arXiv:1306.3983 [astro-ph.HE].

[82] M. Brhlik, in *Proceedings, 2nd International Heidelberg Conference on Dark matter in astrophysics and particle physics (DARK 1998): Heidelberg, Germany, July 20-25, 1998* (1998) pp. 499–515, arXiv:hep-ph/9810279 [hep-ph].

[83] A. Birkedal, K. Matchev, and M. Perelstein, Phys. Rev. **D70**, 077701 (2004), arXiv:hep-ph/0403004 [hep-ph].

[84] F. J. Petriello, S. Quackenbush, and K. M. Zurek, Phys. Rev. **D77**, 115020 (2008), arXiv:0803.4005 [hep-ph].

[85] Y. Gershtein, F. Petriello, S. Quackenbush, and K. M. Zurek, Phys. Rev. **D78**, 095002 (2008), arXiv:0809.2849 [hep-ph].

[86] M. Beltran, D. Hooper, E. W. Kolb, Z. A. C. Krusberg, and T. M. P. Tait, JHEP **09**, 037 (2010), arXiv:1002.4137 [hep-ph].

[87] J. Goodman, M. Ibe, A. Rajaraman, W. Shepherd, T. M. P. Tait, and H.-B. Yu, Phys. Lett. **B695**, 185 (2011), arXiv:1005.1286 [hep-ph].

[88] J. Goodman, M. Ibe, A. Rajaraman, W. Shepherd, T. M. P. Tait, and H.-B. Yu, Phys. Rev. **D82**, 116010 (2010), arXiv:1008.1783 [hep-ph].

[89] Y. Bai, P. J. Fox, and R. Harnik, JHEP **12**, 048 (2010), arXiv:1005.3797 [hep-ph].

[90] P. J. Fox, R. Harnik, J. Kopp, and Y. Tsai, Phys. Rev. **D84**, 014028 (2011), arXiv:1103.0240 [hep-ph].

[91] P. J. Fox, R. Harnik, J. Kopp, and Y. Tsai, Phys. Rev. **D85**, 056011 (2012), arXiv:1109.4398 [hep-ph].

[92] Y. Bai and T. M. P. Tait, Phys. Lett. **B723**, 384 (2013), arXiv:1208.4361 [hep-ph].

[93] A. Friedland, M. L. Graesser, I. M. Shoemaker, and L. Vecchi, Phys. Lett. **B714**, 267 (2012), arXiv:1111.5331 [hep-ph].

[94] I. M. Shoemaker and L. Vecchi, Phys. Rev. **D86**, 015023 (2012), arXiv:1112.5457 [hep-ph].

[95] G. Busoni, A. De Simone, E. Morgante, and A. Riotto, Phys. Lett. **B728**, 412 (2014), arXiv:1307.2253 [hep-ph].

[96] S. Chang, R. Edezhath, J. Hutchinson, and M. Luty, Phys. Rev. **D89**, 015011 (2014), arXiv:1307.8120 [hep-ph].

[97] H. An, L.-T. Wang, and H. Zhang, Phys. Rev. **D89**, 115014 (2014), arXiv:1308.0592 [hep-ph].

[98] Y. Bai and J. Berger, JHEP **11**, 171 (2013), arXiv:1308.0612 [hep-ph].

[99] H. Dreiner, D. Schmeier, and J. Tattersall, Europhys. Lett. **102**, 51001 (2013), arXiv:1303.3348 [hep-ph].

[100] A. DiFranzo, K. I. Nagao, A. Rajaraman, and T. M. P. Tait, JHEP **11**, 014 (2013), [Erratum: JHEP01,162(2014)], arXiv:1308.2679 [hep-ph].

[101] O. Buchmueller, M. J. Dolan, S. A. Malik, and C. McCabe, JHEP **01**, 037 (2015), arXiv:1407.8257 [hep-ph].

[102] M. Papucci, A. Vichi, and K. M. Zurek, JHEP **11**, 024 (2014), arXiv:1402.2285 [hep-ph].

[103] K. Hamaguchi, S. P. Liew, T. Moroi, and Y. Yamamoto, JHEP **05**, 086 (2014), arXiv:1403.0324 [hep-ph].

[104] M. Garny, A. Ibarra, S. Rydbeck, and S. Vogl, JHEP **06**, 169 (2014), arXiv:1403.4634 [hep-ph].

[105] J. Abdallah *et al.*, (2014), arXiv:1409.2893 [hep-ph].

[106] S. A. Malik *et al.*, Phys. Dark Univ. **9-10**, 51 (2015), arXiv:1409.4075 [hep-ex].

[107] D. Abercrombie *et al.*, (2015), arXiv:1507.00966 [hep-ex].

[108] M. Srednicki, R. Watkins, and K. A. Olive, Nucl. Phys. **B310**, 693 (1988).

[109] K. Griest and D. Seckel, Phys. Rev. **D43**, 3191 (1991).

[110] K. A. Olive *et al.* (Particle Data Group), Chin. Phys. **C38**, 090001 (2014).

[111] T. K. Hemmick *et al.*, Phys. Rev. **D41**, 2074 (1990).

[112] S. Profumo and C. E. Yaguna, Phys. Rev. **D69**, 115009 (2004), arXiv:hep-ph/0402208 [hep-ph].

[113] I. Gogoladze, R. Khalid, and Q. Shafi, Phys. Rev. **D79**, 115004 (2009), arXiv:0903.5204 [hep-ph].

[114] D. Feldman, Z. Liu, and P. Nath, Phys. Rev. **D80**, 015007 (2009), arXiv:0905.1148 [hep-ph].

[115] I. Gogoladze, R. Khalid, and Q. Shafi, Phys. Rev. **D80**, 095016 (2009), arXiv:0908.0731 [hep-ph].

[116] N. Chen, D. Feldman, Z. Liu, P. Nath, and G. Peim, Phys. Rev. **D83**, 035005 (2011), arXiv:1011.1246 [hep-ph].

[117] M. Adeel Ajaib, T. Li, Q. Shafi, and K. Wang, JHEP **01**, 028 (2011), arXiv:1011.5518 [hep-ph].

[118] K. Harigaya, M. Ibe, and T. T. Yanagida, JHEP **12**, 016 (2013), arXiv:1310.0643 [hep-ph].

[119] K. Harigaya, K. Kaneta, and S. Matsumoto, Phys. Rev. **D89**, 115021 (2014), arXiv:1403.0715 [hep-ph].

[120] J. L. Evans and K. A. Olive, Phys. Rev. **D90**, 115020 (2014), arXiv:1408.5102 [hep-ph].

[121] J. Ellis, F. Luo, and K. A. Olive, JHEP **09**, 127 (2015), arXiv:1503.07142 [hep-ph].

[122] J. Ellis, J. L. Evans, F. Luo, and K. A. Olive, JHEP **02**, 071 (2016), arXiv:1510.03498 [hep-ph].

[123] C. Boehm, A. Djouadi, and M. Drees, Phys. Rev. **D62**, 035012 (2000), arXiv:hep-ph/9911496 [hep-ph].

[124] J. R. Ellis, K. A. Olive, and Y. Santoso, Astropart. Phys. **18**, 395 (2003), arXiv:hep-ph/0112113 [hep-ph].

[125] J. Edsjo, M. Schelke, P. Ullio, and P. Gondolo, JCAP **0304**, 001 (2003), arXiv:hep-ph/0301106 [hep-ph].

[126] I. Gogoladze, S. Raza, and Q. Shafi, Phys. Lett. **B706**, 345 (2012), arXiv:1104.3566 [hep-ph].

[127] M. A. Ajaib, T. Li, and Q. Shafi, Phys. Rev. **D85**, 055021 (2012), arXiv:1111.4467 [hep-ph].

[128] J. Harz, B. Herrmann, M. Klasen, K. Kovarik, and Q. L. Boulc'h, Phys. Rev. **D87**, 054031 (2013), arXiv:1212.5241 [hep-ph].

[129] J. Harz, B. Herrmann, M. Klasen, and K. Kovarik, Phys. Rev. **D91**, 034028 (2015), arXiv:1409.2898 [hep-ph].

[130] J. Ellis, K. A. Olive, and J. Zheng, Eur. Phys. J. **C74**, 2947 (2014), arXiv:1404.5571 [hep-ph].

[131] S. Raza, Q. Shafi, and C. S. n, Phys. Rev. **D92**, 055010 (2015), arXiv:1412.7672 [hep-ph].

[132] A. Ibarra, A. Pierce, N. R. Shah, and S. Vogl, *Proceedings, Meeting of the APS Division of Particles and Fields (DPF 2015): Ann Arbor, Michigan, USA, 4-8 Aug 2015*, Phys. Rev. **D91**, 095018 (2015), arXiv:1501.03164 [hep-ph].

[133] G. Servant and T. M. P. Tait, Nucl. Phys. **B650**, 391 (2003), arXiv:hep-ph/0206071 [hep-ph].

[134] F. Burnell and G. D. Kribs, Phys. Rev. **D73**, 015001 (2006), arXiv:hep-ph/0509118 [hep-ph].

[135] K. Kong and K. T. Matchev, JHEP **01**, 038 (2006), arXiv:hep-ph/0509119 [hep-ph].

[136] M. Kakizaki, S. Matsumoto, and M. Senami, Phys. Rev. **D74**, 023504 (2006), arXiv:hep-ph/0605280 [hep-ph].

[137] G. Belanger, M. Kakizaki, and A. Pukhov, JCAP **1102**, 009 (2011), arXiv:1012.2577 [hep-ph].

[138] Y. Ishigure, M. Kakizaki, and A. Santa, (2016), arXiv:1611.06760 [hep-ph].

[139] J. Hisano, S. Matsumoto, and M. M. Nojiri, Phys. Rev. Lett. **92**, 031303 (2004), arXiv:hep-ph/0307216 [hep-ph].

[140] J. Hisano, S. Matsumoto, M. M. Nojiri, and O. Saito, Phys. Rev. **D71**, 063528 (2005), arXiv:hep-ph/0412403 [hep-ph].

[141] J. L. Feng, M. Kaplinghat, and H.-B. Yu, Phys. Rev. **D82**, 083525 (2010), arXiv:1005.4678 [hep-ph].

[142] H. Baer, K.-m. Cheung, and J. F. Gunion, Phys. Rev. **D59**, 075002 (1999), arXiv:hep-ph/9806361 [hep-ph].

[143] A. Freitas, Phys. Lett. **B652**, 280 (2007), arXiv:0705.4027 [hep-ph].

[144] A. Hryczuk, Phys. Lett. **B699**, 271 (2011), arXiv:1102.4295 [hep-ph].

[145] A. De Simone, G. F. Giudice, and A. Strumia, JHEP **06**, 081 (2014), arXiv:1402.6287 [hep-ph].

[146] J. L. Feng, M. Kaplinghat, H. Tu, and H.-B. Yu, JCAP **0907**, 004 (2009), arXiv:0905.3039 [hep-ph].

[147] W. Detmold, M. McCullough, and A. Pochinsky, Phys. Rev. **D90**, 115013 (2014), arXiv:1406.2276 [hep-ph].

[148] B. von Harling and K. Petraki, JCAP **1412**, 033 (2014), arXiv:1407.7874 [hep-ph].

[149] H. An, M. B. Wise, and Y. Zhang, Phys. Rev. **D93**, 115020 (2016), arXiv:1604.01776 [hep-ph].

[150] Y. Bai and J. Osborne, JHEP **11**, 036 (2015), arXiv:1506.07110 [hep-ph].

[151] M. J. Baker *et al.*, JHEP **12**, 120 (2015), arXiv:1510.03434 [hep-ph].

[152] K. Petraki, M. Postma, and J. de Vries, (2016), arXiv:1611.01394 [hep-ph].

[153] V. B. Berestetskii, E. M. Lifshitz, and L. P. Pitaevskii, *Quantum Electrodynamics* (Pergamon Press, 1971).

[154] L. D. Landau and E. M. Lifshitz, *Quantum Mechanics*, Course of Theoretical Physics, Vol. v.3 (Butterworth-Heinemann, Oxford, 1991).

[155] D. Kahawala and Y. Kats, JHEP **09**, 099 (2011), arXiv:1103.3503 [hep-ph].

[156] N. Nagata, H. Otono, and S. Shirai, Phys. Lett. **B748**, 24 (2015), arXiv:1504.00504 [hep-ph].

[157] C. F. Berger, L. Covi, S. Kraml, and F. Palorini, JCAP **0810**, 005 (2008), arXiv:0807.0211 [hep-ph].

[158] D. Lindley, Astrophys. J. **294**, 1 (1985).

[159] M. H. Reno and D. Seckel, Phys. Rev. **D37**, 3441 (1988).

[160] S. Dimopoulos, R. Esmailzadeh, L. J. Hall, and G. D. Starkman, Astrophys. J. **330**, 545 (1988).

[161] R. J. Scherrer and M. S. Turner, Astrophys. J. **331**, 19 (1988), [Astrophys. J.331,33(1988)].

[162] S. Dimopoulos, R. Esmailzadeh, L. J. Hall, and G. D. Starkman, Nucl. Phys. **B311**, 699 (1989).

[163] J. R. Ellis, G. B. Gelmini, J. L. Lopez, D. V. Nanopoulos, and S. Sarkar, Nucl. Phys. **B373**, 399 (1992).

[164] M. Kawasaki, K. Kohri, and T. Moroi, Phys. Rev. **D71**, 083502 (2005), arXiv:astro-ph/0408426 [astro-ph].

[165] K. Jedamzik, Phys. Rev. **D74**, 103509 (2006), arXiv:hep-ph/0604251 [hep-ph].

[166] M. Kawasaki, K. Kohri, and T. Moroi, Phys. Lett. **B649**, 436 (2007), arXiv:hep-ph/0703122 [hep-ph].

[167] M. Kawasaki, K. Kohri, T. Moroi, and A. Yotsuyanagi, Phys. Rev. **D78**, 065011 (2008), arXiv:0804.3745 [hep-ph].

[168] J. L. Feng, A. Rajaraman, and F. Takayama, Phys. Rev. Lett. **91**, 011302 (2003), arXiv:hep-ph/0302215 [hep-ph].

[169] J. R. Ellis, K. A. Olive, Y. Santoso, and V. C. Spanos, Phys. Lett. **B588**, 7 (2004), arXiv:hep-ph/0312262 [hep-ph].

[170] J. L. Feng, S.-f. Su, and F. Takayama, Phys. Rev. **D70**, 063514 (2004), arXiv:hep-ph/0404198 [hep-ph].

[171] D. G. Cerdeno, K.-Y. Choi, K. Jedamzik, L. Roszkowski, and R. Ruiz de Austri, JCAP **0606**, 005 (2006), arXiv:hep-ph/0509275 [hep-ph].

[172] J. L. Feng, B. T. Smith, and F. Takayama, Phys. Rev. Lett. **100**, 021302 (2008), arXiv:0709.0297 [hep-ph].

[173] L. Covi, J. E. Kim, and L. Roszkowski, Phys. Rev. Lett. **82**, 4180 (1999), arXiv:hep-ph/9905212 [hep-ph].

[174] L. Covi, H.-B. Kim, J. E. Kim, and L. Roszkowski, JHEP **05**, 033 (2001), arXiv:hep-ph/0101009 [hep-ph].

[175] L. Covi, L. Roszkowski, R. Ruiz de Austri, and M. Small, JHEP **06**, 003 (2004), arXiv:hep-ph/0402240 [hep-ph].

[176] N. Arkani-Hamed and S. Dimopoulos, JHEP **06**, 073 (2005), arXiv:hep-th/0405159 [hep-th].

[177] G. F. Giudice and A. Romanino, Nucl. Phys. **B699**, 65 (2004), [Erratum: Nucl. Phys.B706,487(2005)], arXiv:hep-ph/0406088 [hep-ph].

[178] A. Arvanitaki, C. Davis, P. W. Graham, A. Pierce, and J. G. Wacker, Phys. Rev. **D72**, 075011 (2005), arXiv:hep-ph/0504210 [hep-ph].

[179] J. Kang, M. A. Luty, and S. Nasri, JHEP **09**, 086 (2008), arXiv:hep-ph/0611322 [hep-ph].

[180] K. Kohri and Y. Santoso, Phys. Rev. **D79**, 043514 (2009), arXiv:0811.1119 [hep-ph].

[181] J. E. Kim, Phys. Rev. Lett. **43**, 103 (1979).

[182] M. A. Shifman, A. I. Vainshtein, and V. I. Zakharov, Nucl. Phys. **B166**, 493 (1980).

[183] A. Brandenburg and F. D. Steffen, JCAP **0408**, 008 (2004), arXiv:hep-ph/0405158 [hep-ph].

[184] A. Strumia, JHEP **06**, 036 (2010), arXiv:1003.5847 [hep-ph].

[185] L. Covi, L. Roszkowski, and M. Small, JHEP **07**, 023 (2002), arXiv:hep-ph/0206119 [hep-ph].

[186] M. Aaboud *et al.* (ATLAS), Phys. Rev. **D94**, 032005 (2016), arXiv:1604.07773 [hep-ex].

[187] M. Aaboud *et al.* (ATLAS), Eur. Phys. J. **C76**, 392 (2016), arXiv:1605.03814 [hep-ex].

[188] T. A. collaboration, (2015).

[189] K. Hamaguchi and S. P. Liew, Phys. Rev. **D94**, 035012 (2016), arXiv:1604.07828 [hep-ph].

[190] J. Alwall, R. Frederix, S. Frixione, V. Hirschi, F. Maltoni, O. Mattelaer, H. S. Shao, T. Stelzer, P. Torrielli, and M. Zaro, JHEP **07**, 079 (2014), arXiv:1405.0301 [hep-ph].

[191] J. Alwall, M. Herquet, F. Maltoni, O. Mattelaer, and T. Stelzer, JHEP **06**, 128 (2011), arXiv:1106.0522 [hep-ph].

[192] T. Sjostrand, S. Mrenna, and P. Z. Skands, JHEP **05**, 026 (2006), arXiv:hep-ph/0603175 [hep-ph].

[193] M. Drees, H. Dreiner, D. Schmeier, J. Tattersall, and J. S. Kim, Comput. Phys. Commun. **187**, 227 (2015), arXiv:1312.2591 [hep-ph].

[194] J. S. Kim, D. Schmeier, J. Tattersall, and K. Rolbiecki, Comput. Phys. Commun. **196**, 535 (2015), arXiv:1503.01123 [hep-ph].

[195] J. de Favereau, C. Delaere, P. Demin, A. Giammanco, V. Lematre, A. Mertens, and M. Selvaggi (DELPHES 3), JHEP **02**, 057 (2014), arXiv:1307.6346 [hep-ex].

[196] M. Cacciari, G. P. Salam, and G. Soyez, Eur. Phys. J. **C72**, 1896 (2012), arXiv:1111.6097 [hep-ph].

[197] M. Cacciari and G. P. Salam, Phys. Lett. **B641**, 57 (2006), arXiv:hep-ph/0512210 [hep-ph].

[198] M. Low and L.-T. Wang, JHEP **08**, 161 (2014), arXiv:1404.0682 [hep-ph].

[199] G. Aad *et al.* (ATLAS), JHEP **01**, 068 (2015), arXiv:1411.6795 [hep-ex].

[200] S. Chatrchyan *et al.* (CMS), JHEP **07**, 122 (2013), arXiv:1305.0491 [hep-ex].

[201] M. Aaboud *et al.* (ATLAS), Phys. Lett. **B760**, 647 (2016), arXiv:1606.05129 [hep-ex].

[202] M. Aliev, H. Lacker, U. Langenfeld, S. Moch, P. Uwer, and M. Wiedermann, Comput. Phys. Commun. **182**, 1034 (2011), arXiv:1007.1327 [hep-ph].

[203] D. Goncalves-Netto, D. Lopez-Val, K. Mawatari, T. Plehn, and I. Wigmore, Phys. Rev. **D85**, 114024 (2012), arXiv:1203.6358 [hep-ph].

[204] Y. Kats and M. D. Schwartz, JHEP **04**, 016 (2010), arXiv:0912.0526 [hep-ph].